SCUOLA NORMALE SUPERIORE

PH.D. THESIS

IN BIOPHYSICAL SCIENCES

INTERFACING GRAPHENE WITH PERIPHERAL NEURONS:
INFLUENCE ON NEURITE OUTGROWTH
AND NGF AXONAL TRANSPORT

CANDIDATE

Domenica Convertino

ADVISORS

Camilla Coletti

Laura Marchetti

SUPERVISOR

Stefano Luin

Foreword

This thesis is the result of my research activity at NEST Laboratory of Scuola Normale Superiore in Pisa. I started to work on graphene in 2013. I continued during my PhD at NEST since 2014, focusing mainly on graphene interaction with peripheral neurons. This research was performed within a joint PhD program sponsored by Scuola Normale Superiore and Istituto Italiano di Tecnologia.

Table of Contents

List of abbreviations

DRG	Dorsal root ganglion
NGF	Nerve growth factor
GO	Graphene oxide
rGO	Reduced graphene oxide
LPE	Liquid phase exfoliation
GB	Graphene-based
FBS	Fetal bovine serum
CNF	Carbon nanofiber
CNT	Carbon nanotube
GAP-43	Growth-associated protein-43
NFL	Neurofilament light chain
FAK	Focal adhesion kinase
MAPK	P38 mitogen-activated protein kinase
SiC	Silicon carbide
CVD	Chemical vapor deposition
P	Post-natal day
PLL	Poly-L-Lysine
PDL	Poly-D-Lysine
DIV	Days in vitro
FluoNGF	Fluorolabeled NGF
AFM	Atomic force microscopy
STORM	Stochastic optical reconstruction microscopy
TEM	Transmission electron microscopy
WS_2	Tungsten disulfide
RT	Room temperature
μ	Mobilities

MG	Multi-layered graphene
SNR	Signal-to-noise ratio
NSC	Neural stem cell
SEM	Scanning electron microscopy
FWHM	Full width at half maximum
QFSMG	Quasi-free standing monolayer graphene
PMMA	Poly-methyl-methacrylate
SLG	Single layer graphene
APS	Ammonium persulfate
DI	Deionized
RMS	Root-mean-square
BDNF	Brain-derived neurotrophic factor
^{125}I-NGF	Iodine-125-labeled NGF
QD-NGF	Quantum dot-labeled NGF
CoA	Coenzyme A
HPLC	High-performance liquid chromatography
PDMS	Polydimethylsiloxane
SC	Soma compartment
AC	Axon compartment
PFA	Paraformaldehyde
BSA	Bovine serum albumin
DAPI	4′,6-diamidino-2-phenylindole
SDS-PAGE	Sodium Dodecyl Sulphate - PolyAcrylamide Gel Electrophoresis
ROI	Region of interest
MT	Microtubule
NHF	Neurofilament heavy
MPS	Membrane-associated periodic skeleton

TMD	Transition metal dichalcogenide
RA	Retinoic acid
FL	Few layers

Abstract

Graphene displays properties that make it appealing for neuroregenerative medicine, yet the potential of large-scale highly-crystalline graphene as a conductive peripheral neural interface has been scarcely investigated. In particular, pristine graphene offers enhanced electrical properties that can be advantageous for nervous system regeneration applications.

In this work, we investigate graphene potential as peripheral nerve interface. First, we perform an unprecedented analysis aimed at revealing how the typical polymeric coatings for neural cultures distribute on graphene at the nanometric scale. Second, we examine the impact of graphene on the culture of two established cellular models for peripheral nervous system: PC12 cell line and primary embryonic rat dorsal root ganglion (DRG) neurons, showing a better and faster axonal elongation using graphene.

We then observe that the axon elongation in the first days of culture correlates to an altered nerve growth factor (NGF) axonal transport, with a reduced number of retrogradely moving NGF vesicles in favor of stalled vesicles. We thus hypothesize that the axon elongation observed in the first days of culture could be mediated by this pool of NGF vesicles locally retained in the medial/distal parts of axons.

Furthermore, we investigate electrophysiological properties and cytoskeletal structure of peripheral neurons. We observe a reduced neural excitability and altered membrane potential together with a reduced inter-microtubular distance on graphene and correlate these electrophysiological and structural reorganizations of axon physiology to the observed vesicle stalling.

Finally, the potential of another 2D material as neural interface, tungsten disulfide, is explored.

Introduction

A specific feature of peripheral nerves is the ability to spontaneously regenerate after traumatic injuries. In the presence of important gaps where an end-to-end suture is not possible, a surgical approach is preferred, where nerve conduits (generally, autografts or allografts) are used as bridges between the nerve stumps and provide physical guidance for the axons [1]. However, these present limitations in functional recovery and other disadvantages, e.g. size mismatch and increasing healing time for autografts, and rejection and disease transmission for allografts [2]. A promising alternative is represented by tissue engineered nerve grafts, which have shown to improve regeneration, reduce scar formation and increase the concentration of neurotrophic factors [1,3]. Among materials that can be used for the guide production, silicon stimulates excessive scar tissue formation thus lacking long-term stability, while some other natural polymers, such as collagen and chitosan, lack adequate mechanical and electrical properties [4–6].

In recent years, new materials have been suggested as alternative candidates for tissue engineering applications. In particular, due to their unique features, graphene and its derivatives have attracted great attention in a broad range of fields, including biomedical applications.

Graphene is a single layer of carbon atoms arranged in a honeycomb lattice, firstly isolated in 2004 from graphite [7]. The increasing research interest in graphene is due to its peculiar features: superior mechanical properties both in strength and flexibility, high electron mobility and thermal conductivity and high area/volume ratio [8,9]. Furthermore, its transparency, flexibility, biocompatibility and chemical stability make it ideally suited for biomedical applications [10].

In the past years, a number of studies have investigated graphene potential as a conductive neural interface, which can enhance adhesion, proliferation, differentiation and outgrowth of different cell types, including neural cells [11–15]. Graphene turned out to be a promising material in regenerative medicine to realize a scaffold that provides support in nervous system regeneration [5,16–18].

Most of the biomedical studies published to date have explored graphene covalently-functionalized forms, such as graphene oxide (GO) and its chemical reduction known as reduced graphene oxide (rGO), or liquid phase exfoliated (LPE) graphene [10,17,19–24]. These graphene-like structures have altered electronic structure and physical properties due to the variable fraction of sp^2 and sp^3 hybridized carbon atoms. With respect to those graphene-based (GB) materials, pristine graphene assures its unique electrical and tribological properties and most notably an excellent electrical conductivity, thus prospecting advantages for nervous system regeneration applications for the positive effect of conductive materials on axon regeneration [5,13,25]. For these reasons, graphene and carbon nanotubes have been tested to realize composite materials as an alternative to the conductive polymers usually preferred as bioactive scaffold [6,25,26].

The studies that use pristine graphene usually interface it with central neurons [11,27]. In this direction much progress has been made; *e.g.* graphene has been successfully used for high-resolution neurophysiological recording and stimulation [28–30]. On the other hand, despite graphene potential in nerve tissue regeneration, only few studies have investigated pristine graphene interaction with peripheral neurons [12,31]; these suggested a positive effect on neurite outgrowth and proliferation when using graphene coated with fetal bovine serum (FBS). However, in both studies bare glass was used as control, thus the effect on the results of FBS coating, which per se is not a traditional coating for neural cells [32], was not investigated. Moreover, no detailed study has yet examined the homogeneity and quality of the coatings typically adopted in neuronal culture. Predicting how polymeric surface coatings distribute onto graphene, due to its hydrophobicity and extreme flatness, is by no means trivial; furthermore, understanding how nerve cells can sense graphene under extracellular-matrix-like coatings is crucially important for possible in vivo applications. Overall, this lack of studies on pristine graphene leaves other carbon-based materials such as carbon nanofibers (CNF), carbon nanotubes (CNT), GO and rGO to star in its play [5,17,33,34].

Furthermore, little is known about the nanoscale mechanisms by which graphene would promote axon regeneration. Li *et al.* showed that especially during the developmental phase graphene accelerated neurite sprouting and outgrowth in hippocampal neurons. A recognized marker of developing and regenerating axons, growth-associated protein-43 (GAP-43), was investigated to understand the molecular mechanism promoting outgrowth on graphene. Interestingly, increased GAP-43 protein levels was reported [11]. Similarly, increased GAP-43 and synaptophysin levels were also reported in PC12 cells grown on aligned silk-graphene hybrid hydrogels [35], suggesting that the mechanisms driving neurogenesis may be shared for central and peripheral neurons grown on graphene. Graphene was also demonstrated to stimulate human neuroblastoma (SH-SY5Y) cell neurogenesis, upregulating the expression of the neurofilament light chain (NFL), through focal adhesion kinase (FAK) and p38 mitogen-activated protein kinase (MAPK) cascades.

A recent study has reported for hippocampal neurons grown on graphene an increased cell firing probably due to altered membrane ion currents at the material interface [27]. Indeed, several reports described a positive effect of electrical stimulation on axonal outgrowth and branching [13,36,37]. However, such effect may not necessarily apply to peripheral neurons on graphene, as it was already reported that DRG neurons respond differently from hippocampal neurons on nanofabricated biomaterial scaffolds [38,39]. Importantly, all the above-cited studies were carried out on cultures grown from one to three weeks onto the substrate. While this strategy is useful to understand the long-term effects of the material on neuron physiology, it fails to investigate how the early developmental stage is influenced by the neuron-material interface. Indeed, this appears to be an important issue to unravel, because the positive effect of graphene on axonal sprouting and outgrowth was found to be maximal during the first two days of culture, and then to decrease up to a steady-state level in which axons are slightly longer with respect to control cultures [11].

Objective and results of the thesis

The overall motivation of the thesis is to investigate the potential of graphene as a conductive peripheral neural interface.

Three aims in particular are targeted:

(i) to examine how the polymeric coating typically adopted in neuronal culture distribute onto the highly hydrophobic graphene;
(ii) to assess graphene effect on axonal sprouting and viability of two cellular models used to study peripheral nerve regeneration;
(iii) to investigate graphene effect on primary neurons during the early developmental phase, i.e., when we could detect a maximal axonal elongation with respect to a control substrate.

To this purpose, we synthesized graphene on different substrates and with different techniques: via thermal decomposition of silicon carbide (SiC) dice [40] and via chemical vapor deposition (CVD) on copper (Cu) foils [41]. This allowed us to study both an ideal model – i.e., graphene on SiC is extremely clean as it does not need transfer and cells can be cultured directly on it – and the realistic model of CVD graphene grown on Cu and transferred on substrates of choices which can be, at need, of different chemical composition, planar or flexible. These different graphene substrates were used for systematically investigating vitality, axonal outgrowth and NGF transport of two different cellular models of peripheral neurons, namely PC12 immortalized cell line [42] and primary rat embryonic DRG neurons [43]. However, as a more reliable model to study axonal regeneration requires the use of adult neurons, we also set up a method for dissection of DRGs from post-natal day 3-4 (P3-4) mice and for their further dissociation and culture, and these were alternatively used throughout the experiments as detailed below.

In the first part of this thesis, we used epitaxial graphene obtained via thermal decomposition on SiC. Graphene was synthesized with single layer thickness and high crystallinity as confirmed by atomic and spectroscopic characterization [44]. A careful nano-resolved analysis of typical polymeric coatings for neural cultures on such substrate was performed, in order to examine their distribution on the highly hydrophobic graphene surface. Differently from the control substrates, where the polymeric coatings distributed homogeneously, on graphene aggregates were observed. Only the Poly-L-Lysine (PLL) coating tended to form a uniform carpet of 1 nm spots, while Collagene Type I, Poly-D-Lysine (PDL) and laminin formed network-like structures [45]. Then, we cultured PC12 cells and embryonic DRG neurons on graphene, in order to evaluate the material cytocompatibility and its effect on the neuron differentiation process. Graphene significantly improved neurite outgrowth of PC12 cells, with an increased neurite length on graphene up to 35% more than controls. DRG primary neurons survived both on uncoated and coated graphene and showed dense axonal networks comparable to the controls [45]. These results suggested that novel concepts of active nerve conduits promoting better and faster axonal elongation can be devised by using graphene. However, it should be noted that flexibility and scalability are requirements in neural regeneration that cannot be easily met by using graphene on SiC.

For these reasons, in the following part of the thesis CVD graphene was synthesized on Cu and transferred on glass coverslips. Also in this case graphene synthesis was carefully carried on by controlling the single layer thickness and by maximizing the crystallinity of the material. An optimized transfer process was developed to increase graphene adhesion on glass, and the effect of graphene on post-natal DRG neurons was investigated. It was observed that, differently from glass where the cell monolayer was homogeneously distributed, cell bodies formed aggregates connected by fasciculated axonal bundles on graphene, which however did not affect culture vitality.

To better explore CVD graphene influence on axonal outgrowth, P3-4 DRG neurons were grown within compartmentalized chambers placed on top of the graphene substrate or on graphene-coated glass coverslip, using glass coverslip as control. We monitored axonal elongation during the first 4 days in vitro (DIV) of neuron development and found a statistically significant neuron outgrowth on graphene during the first 3 days of culture, with an axonal sprouting up to 79% greater than in the control. To shine light on this result, the role of the NGF neurotrophin, a key molecule involved in neurite elongation and survival during DRG development [46,47] was investigated by single-molecule fluorescence microscopy of a fluorolabeled NGF (fluoNGF). A remarkably altered vesicle trafficking was observed on graphene with respect to a glass control, consisting in a reduced number of retrogradely or anterogradely moving, as well as oscillating, NGF vesicles in favor of stalled vesicles. Interestingly, we found that axonal sprouting on graphene correlates with this significant reduction of NGF vesicles retrogradely transported to the soma, in favor of a stalled pool retained locally in the developing axons.

Combined electrophysiology and ultrastructural analyses showed that profound rearrangements occur in axons developing on graphene. Axon elongation correlates with a mutual charge redistribution observed both for the material via Raman spectroscopy and for the cell membrane via electrophysiological recording. Furthermore, ultrastructural analysis indicates a reduced inter-microtubule distance and a stretched axonal topology. We believe that these rearrangements could be causally involved in the local accumulation of NGF, which acts in the medial and distal parts of axons boosting axon elongation.

Thus, both electrophysiological and structural effects account for graphene action on neuron development. Unraveling the molecular players underneath this interplay may open new avenues for axon regeneration applications.

This work paves the way to test in vivo graphene in peripheral nerve regeneration. The direct transfer of the transparent graphene onto flexible and biocompatible substrates allows the realization of a nerve conduit that not only improves regeneration of injured nerves, but can also be used to electrically stimulate nerves and monitor axonal transport in vivo.

Thesis outline

Chapter 1 addresses the basic properties of graphene and gives an overview of its applications, focusing in particular on graphene biomedical applications. Existing works on graphene neural interfaces are reported and the key issues that motivated this study are explained.

Chapter 2 gives an overview of the main synthesis methods, focusing on the ones used in this work: epitaxial growth on SiC via thermal decomposition and chemical vapor deposition on copper (section 0). Section **Error! Reference source not found.** presents the standard surface characterization instruments for structural, chemical and electronic analysis of the graphene substrate: atomic force microscopy (AFM) and Raman spectroscopy. In particular, it is clarified how AFM allows probing graphene quality, in terms of morphology, roughness and uniformity. It is also described how Raman spectroscopy can be used to assess graphene electronic and structural properties, focusing on the possibility to extract information on doping and strain.

The different growth modes for graphene on Si- and C-face of SiC are then illustrated, together with the experimental approaches developed within this thesis to improve C-face graphene topography and homogeneity and Si-face graphene quality (section 2.3). The choice of the best samples for cell culture experiments is also explained. The optimization of the transfer process of CVD graphene for cell culture applications is finally discussed in section 2.4.

After a brief introduction to the sample characterization (section 3.2), **Chapter 3** reports the distribution of the typical polymeric coatings for neural cultures on graphene at the nanometric scale (section 3.3). Furthermore, it is presented the impact of graphene on the culture of two established cellular models for peripheral nervous system: PC12 cell line (section 3.4) and primary embryonic rat DRG neurons (section 3.5). Notably, the morphometric analysis of cell differentiation shows that graphene significantly improves neurite outgrowth. Remarkably, graphene performs better than gold, an appealing conductive alternative for biomedical applications. These results suggest that graphene holds great promises as an active substrate in nerve guidance conduit devices.

Chapter 4 focuses on graphene effect on axonal elongation of developing DRG neurons on graphene. In section 4.1, the NGF neurotrophin, which is involved in neuron survival and elongation and is an object of study in this work, is introduced. Subsequently, the approaches that have been adopted to study NGF binding, internalization and axonal transport (section 4.1) are discussed. The experimental procedures used to label the neurotrophin and check its quality are also reported. Section 4.2 describes the approach specifically developed in this thesis to combine graphene with compartmentalized chambers in order to study the trafficking of labeled NGF in living cells on graphene. It also reports the custom made Matlab script for Single particle tracking of the fluorescent vesicles (section 4.2.10) as well as the techniques adopted to characterize neurons electrophysiological (Patch-clamp, section 4.2.11) and morphological properties (Stochastic optical reconstruction microscopy (STORM), transmission electron microscopy (TEM), section 4.2.12 and 4.2.13). Section 4.3 describes the use of two different green excitable fluorophores to produce the labelled neurotrophin (fluoNGF). In this section it is also investigated whether the choice of the fluorophore influences the labelling reaction on purified NGF, the fluoNGF internalization in neurons and the axonal transport properties. The effect of graphene on axonal sprouting is thoroughly reported in section 4.4, while the correlation between axonal sprouting and altered NGF axonal transport is discussed in section 4.5. Finally, the possible cause-effect links between NGF vesicle stall and axon elongation are investigated in sections 4.6 and 4.7, by examining the possible electrophysiological and structural changes prompted by graphene.

Chapter 5 presents a preliminary study of cell viability on centimeter-scale tungsten disulfide (WS_2) grown on sapphire and compares it to that obtained on graphene on sapphire. The quality, thickness and homogeneity of the materials is analyzed by using AFM and Raman spectroscopy (sections 5.3 and 5.4). The cytotoxicity of WS_2 is investigated by cell viability and differentiation assessment on SH-SY5Y cells (section 5.5).

1 Graphene in neural interfaces

In this chapter a brief introduction on graphene structure and properties is reported. Graphene bioapplications are then discussed, with particular attention to graphene as a neural interface in nerve tissue regeneration.

1.1 Graphene structure

Graphene is a monolayer of sp^2-hybridized carbon atoms arranged in a two-dimensional honeycomb lattice, firstly isolated from graphite in 2004 by Andre Geim and Konstantin Novoselov [7]. It is the mother of all the other graphitic forms of different dimensions: fullerenes (0D), carbon nanotubes (1D) and graphite (3D) (**Error! Reference source not found.**).

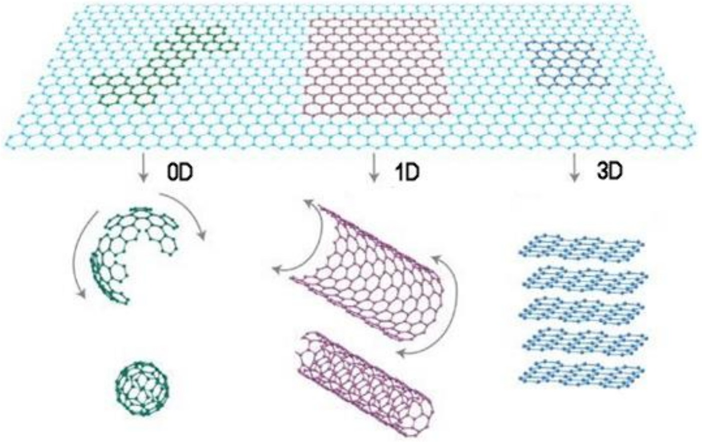

Fig. 1.1. **Graphene as building block for carbon materials of all other dimensionalities**: 0D fullerenes, 1D carbon nanotube and 3D graphite. Adapted from [48].

The 2s and two 2p orbitals hybridize to form three sp^2 planar orbitals that participate in covalent σ bonds. The fourth electron occupies the perpendicular

p_z orbital and forms a delocalized π bond. The strong σ bonds are responsible of graphene mechanical properties, while the delocalization of π electrons gives rise to a high graphene electrical conductivity [49].

The first graphene flakes were isolated by mechanical exfoliation of highly oriented pyrolytic graphite using an ordinary scotch tape and transferred on a silicon substrate to fabricate a metallic field-effect transistor [7]. Thanks to their "groundbreaking experiments regarding the two-dimensional material graphene", Geim and Novoselov were awarded the 2010 Nobel Prize in Physics [50].

1.2 Graphene properties

Graphene shows peculiar electrical, thermal, optical and mechanical properties. Graphene films exhibit a pronounced ambipolar electric field effect such that charge carriers can be tuned continuously between electrons and holes in concentrations up to 10^{13} cm^{-2} and their mobilities (μ) can exceed 100000 $cm^2V^{-1}s^{-1}$ even under ambient conditions [48]. Graphene electrical properties derive from its band structure: it is a zero-gap semiconductor with a π-bands linear dispersion at the K points of the Brillouin zone, also known as the Dirac points (**Error! Reference source not found.**). Due to this l inearity, the charge carriers in the graphene have no rest mass and behave like relativistic particles [9,48].

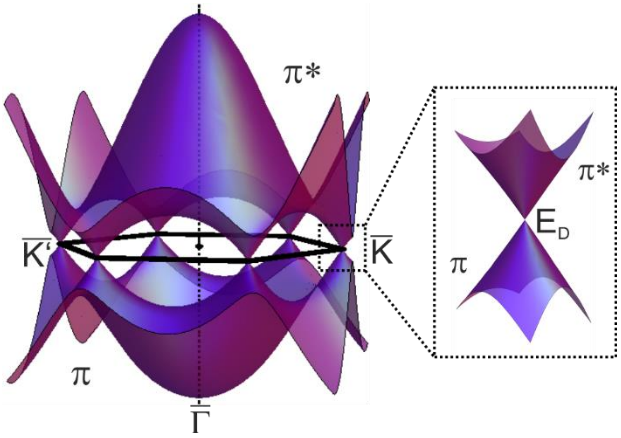

Fig. 1.2. **Electronic dispersion in the graphene lattice.** Plot of the π-bands over the Brillouin zone, with a zoom-in of the energy bands in the vicinity of the Dirac point (E_D). Adapted from [51].

In addition, graphene is the strongest material ever measured, with Young's modulus of the order of 1 TPa and the intrinsic strength of 130 GPa [8]. Furthermore it has other remarkable properties: high thermal conductivity up to 3000 W mK^{-1} near room temperature (RT) [52]; impermeability at standard gases [53]; optical transparency [54]; outstanding mechanical flexibility and chemical durability [55]; biocompatibility [56]. These interesting properties make it suitable for different applications in nanoelectronics, transparent conducting electrodes, hydrogen storage [57,58], biomedical and sensing fields [59,60]. In addition, properties and applications of vertical heterostructures composed of graphene and other 2D materials have been attracting a lot of attention in the fields of electronics and optoelectronics [61–63].

1.3 Graphene bioapplications

Graphene properties could be exploited in biosensing, drug delivery, antibacterial activity and imaging [64–67]. Furthermore, transparency and flexibility properties, together with electrical conductivity, make it an excellent candidate material for neural interfacing devices that combine stimulation and recording [28,29,68] and for tissue engineering applications [5,69,70].

Graphene can be produced with different methods, resulting in different materials in terms of size, shape, number of layers, purity, lateral dimensions and chemical modification that can influence its applications [71]. For example, GO and its chemical reduction known as rGO are usually preferred for biomedical applications thanks to the high water solubility and easy functionalization of the oxygenated species introduced during the oxidation processes [72,73]. However, in GO the large fraction of sp^3 carbon covalently bonded to oxygen to form epoxy and hydroxyl groups degrades the electronic performances of the material [74].

Highly crystalline graphene obtained via CVD has instead been mainly adopted for many applications including biosensing [75–77], stem cell differentiation [14] and neural electrodes [28,29].

One of the possible drawbacks in using GB materials in biomedical applications may be related to the unclear and highly debated cytotoxicity [78,79]. It has been demonstrated that GO induced functional alterations in primary astrocytes [24] and cortical neurons [20]. In spite of that, the potential cytotoxicity of graphene is often associated to disperse graphene flakes. Graphene flakes showed a shape and concentration-dependent cytotoxicity on PC12 cells [78], just as GO had a dose-dependent cytotoxicity in human fibroblast cells and mice [80]. On the other hand, when GO is functionalized using different reducing agents, its toxicity can be drastically reduced [81,82].

1.4 Graphene in neural interfaces

In the past years, several studies have been conducted to investigate the use of GB materials as biocompatible neural interfaces [11,14,19–24,27,83–87]

To date, most of the studies have investigated graphene covalent-functionalized forms such GO and rGO, or LPE graphene [10,17,19–23]. GB materials can be used to design 3D scaffolds, in form of composites, foams, fibers and hydrogels to enhance their optical, electrical and mechanical properties, in a condition closer to the in vivo environment [70]. With respect to those GB materials, pristine graphene, the defect-free layer of sp^2 hybridized carbon atoms, offers enhanced electrical and tribological properties and most notably an excellent electrical conductivity. Thus, it can be possibly used as an electroactive scaffold that enhances neuronal regeneration and functional recovery [70].

The effect of GB materials on neural cells, even in the absence of any coating agent, has been investigated in many studies. An impairment of excitatory transmission was found in primary neurons following a chronic exposure to graphene oxide flakes [20,23]. Bramini *et al.* observed that, even without interfering with neuron viability and intrinsic excitability, graphene exposure decreased the network electrical activity by creating an imbalance between synaptic excitation and inhibition [20]. Rauti *et al.* showed similar results on primary hippocampal neurons. They reported that higher concentration of GO affected synapse formation and function without altering cell survival [23].

It is important to notice that the previous studies employed a solution of graphene oxide. When a flat surface coated with graphene was used, the synaptic formation and network activity in hippocampal neurons were not altered [22]. Uncoated graphene produced by LPE was reported to retain unaltered neuronal behavior, supporting neuronal functional development in the absence of any perturbation of the neuronal network synaptic and electrophysiological properties (neuronal passive properties, spontaneous synaptic activity and short-term synaptic plasticity). Uncoated thermally reduced graphene (TRG) was shown to favor the multi-lineage differentiation of adult mouse olfactory bulb into neurons, astrocytes and oligodendrocytes. TRG supported the morphological differentiation of oligodendrocytes and the formation of functional synapses in neurons [21].

Graphene has also been interfaced with neural cells to exploit its applications in tissue engineering, as electroactive scaffold that can facilitate functional connection between neurons [69]. Indeed, it has been demonstrated that conductive materials can enhance the electric field produced by the cell, influencing cell bioelectric properties [85]. Electrical stimulation can also improve and direct neurite outgrowth [13,25] and can accelerate axonal elongation [5]. Neural conductive interfaces for neural regeneration application usually exploit conductive polymers, such as polyethylenedioxythiophene (PEDOT) and polypyrrole (PPy), or composite materials whose conductivity depends on the inclusion of graphene or CNTs [6,16,18,25,26,88]. Jakus *et al.* realized a 3D printable scaffold consisting of graphene with a minority of polylactide-co-glycolide that could be used as electrically conducting scaffolds for tissue regenerative engineering applications [16]. Qian and colleagues fabricated a multi-layered porous scaffold composed of single-layered graphene or multi-layered graphene (MG) and polycaprolactone (PCL). The in vivo studies revealed that these substrates improves axonal regeneration and nerve remyelination after physical nerve injury, with a successful sensory recovery [18]. Golafshan *et al.* developed a hybrid graphene nanosheets-sodium alginate/polyvinyl alcohol fibrous scaffold and observed an enhanced PC12 cells adhesion and proliferation [88]. Additional researches supported the anti-inflammatory ability of 3D graphene foams, probably due to their topographical structures, and the enhanced neural survival (neural stem cell and PC12) by the activation of microglia [89].

The use of pristine graphene with or without a polymeric coating is usually preferred to realize 2D devices, as planar electrodes to stimulate and record neural activity. Indeed, recently graphene and CNTs have been successfully used to improve recording and electrical stimulation of neurons [28,90] and surprisingly neural microelectrode arrays (MEAs) fabricated using graphene performed better than gold and indium tin oxide (ITO), in terms of signal-to-noise ratio (SNR) [91]. Park *et al.* developed a graphene-based, carbon-layered electrode array (CLEAR) device that was implanted on rodent brain for high-resolution neurophysiological recording. Thanks to graphene biocompatibility, transparency and flexibility the CLEAR device showed long-term in vivo stability and viability for optogenetic activation of focal cortical areas, electrophysiology and cortical imaging [29]. Kuzum and coauthors developed a transparent flexible neural electrode based on graphene for simultaneous electrophysiological recording and optical imaging, with an improved SNR and substantial reduction in electrical interference noise [28]. The technique has been recently improved to integrate 2-photon microscopy, optogenetic, stimulation and cortical recordings in the same in vivo experiment [92]. Recently, graphene has been also used to realize solution-gated field-effect transistor that were used to record visual and auditory responses in rats with performance similar to platinum black electrodes [30].

Polymer-coated graphene was also shown to enhance the differentiation of neural stem cells (NSC) into neurons rather than glia [14]. Park *et al.* exploited graphene as a transparent electrode, observing a good electrical coupling between graphene and neurons for electrical stimulation and confirming the neural activity of the differentiated cells [14]. The resulting neural network functionality and the graphene effect on the maturation of the NSC's electrophysiological state was also investigated by Guo *et al.* Graphene influenced both the passive and active bioelectric membrane properties, hyperpolarizing the resting membrane potential and increasing the firing of action potentials during development, resulting in an accelerated maturation and enhanced neural performance [85]. In addition, coated GB materials were found to support the growth of primary hippocampal neurons, without affecting cell viability and morphology and accelerating neurite sprouting and outgrowth especially during the developmental phase [11].

Even in the absence of a coating, CVD graphene was shown to be biocompatible, sustaining neuron survival and neurite outgrowth. Bendali *et al.* examined the survival and neurite outgrowth of adult retinal neurons both on bare and polymeric coated graphene. They confirmed the graphene potential as a cytocompatible material for interfacing neurons with electronic devices, even if the presence of a polymeric coating seemed to help cell adhesion and spreading [87]. Sahni *et al.* used bare graphene to culture cortical neurons and showed long, linear neurite growth and synapse-like structure formation. They reported also an increased adhesion of neurons on graphene, compared to the bare plastic dishes, that was explained by van der Waals overcoming the hydrophobic forces of the plastic dish [83]. More recently, Pampaloni *et al.* have disclosed that single layer graphene boosts neuronal activity, increasing the action potential frequency in hippocampal neurons by altering extracellular ion distribution at the material interface. They hypothesized that potassium ions are trapped at the carbon surface, leading to a local depletion at the neuronal membrane [27]. Also, it has been shown, that neural affinity strongly depends on the graphene quality. Veliev *et al.* showed that hippocampal neurons cultured on bare graphene had an improved adhesion and outgrowth, with a neuritic architecture similar to the conventional coated controls. On the other hand, the use of defective graphene prevented cell attachment, demonstrating that the presence of carbon atoms alone does not guarantee the material cytocompatibility, but rather the material crystalline quality plays a crucial role [86].

It should be noted that most of the existent studies that use pristine graphene as a neural interface investigate its effect on central neurons. To date, the interaction between pristine graphene and peripheral neural cells has been scarcely investigated, even if graphene positive effect on neurite outgrowth and proliferation could open opportunities in neuroscience, neural engineering and regenerative medicine [12,31].

2 Graphene synthesis and characterization

In this Chapter, section 0 gives an overview of the different graphene synthesis methods. Section 2.2 describes the characterization techniques mainly used in this work to investigate the structural, chemical and electronic properties of the graphene substrates: AFM, scanning electron microscopy (SEM) and Raman spectroscopy. An extensive description of the synthesis methods used in this thesis – epitaxial growth on SiC and CVD on copper – is given in section 2.3 and 2.4 The different growth processes specifically developed and adopted in this work are described, together with the approaches used to improve graphene quality. Finally, the optimized transfer approach developed to increase graphene adhesion on glass is presented.

This chapter contains information published in the peer-reviewed work with authors D. Convertino, A. Rossi, V. Miseikis, V. Piazza, C. Coletti: "Thermal decomposition and chemical vapor deposition: a comparative study of multi-layer growth of graphene on SiC(000-1)." MRS Advances 1(55):3667–72 (2016). Experiments and data shown in each figure were performed and analyzed by D. Convertino.

Graphene samples were also produced and characterized for collaborations that has led to the publication of numerous works cited in the chapter and coauthored by D. Convertino.

2.1 Graphene growth

Since its first isolation in 2004, a great effort has been made by the research community to produce graphene with different methods that span from micromechanical exfoliation, to chemical-based approaches, to thermal decomposition of silicon carbide and chemical vapor deposition on metals (Fig. 2.1).

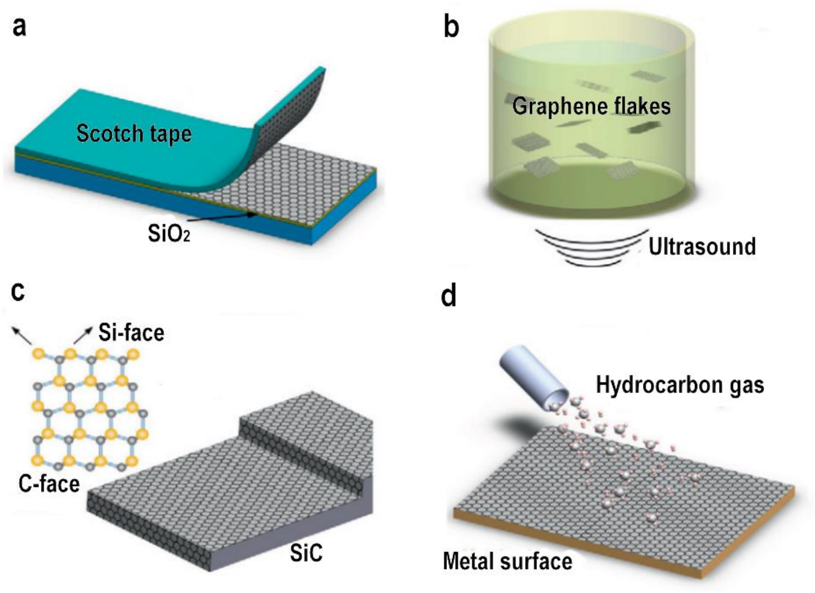

Fig. 2.1. **Schematic illustration of graphene synthesis methods.** (a) Micromechanical exfoliation. (b) Liquid phase exfoliation. (c) Thermal decomposition of SiC. (d) Chemical vapor deposition on transition metals. Adapted from [93].

Micromechanical exfoliation consists in a repeated peeling of flakes of graphite using scotch tape (Fig. 2.1(a)) [7]. The weak van der Waals interplanar interactions allow the isolation of single layers of graphene that can be transferred by simply pressing the tape onto another substrate. This graphene presents the highest quality level and it is preferred for fundamental studies thanks to its perfect crystallinity and low density of defects. However, the typical micrometric size of the exfoliated flakes makes them unsuitable for large-scale production and applications.

In LPE the exfoliation process is scaled up. The graphite is dispersed in a solvent, exfoliated using ultrasound and ultracentrifugated to remove the un-exfoliated flakes (Fig. 2.1(b)) [93]. The principle of LPE can also be used to exfoliate GO. The obtained GO has to be reduced using thermal or chemical treatments. These graphene-like structures have degraded quality and purity, altered electronic structure and physical properties due to the variable fraction of sp^2 and sp^3 hybridized carbon atoms and are usually used to produce conducting films and composites [94].

The two main techniques for wafer-scale synthesis of high quality graphene are thermal decomposition of SiC (Fig. 2.1(c)) [95,96] and CVD of graphene on transition metals (Fig. 2.1(d)) [41,97,98]. These techniques guarantee scalability and cleanliness, preserving the graphene quality in terms of transparency and electrical conductivity and for these reasons were adopted in this work.

Using thermal decomposition, the SiC wafer is annealed at high temperature leading to silicon desorption from the surface that leaves graphene layers behind [96]. Graphene thus can be obtained directly on a commercially available semiconducting or semi-insulating substrate and no transfer is required. The SiC wafer is commonly cut in a way that produces the surface orientations (0001) and $(000\bar{1})$, called the Si- and C-face, respectively. The choice of the SiC crystal face to grow graphene strongly influences the results [96]. Indeed, thermal decomposition is not a self-limiting process and areas of different film thicknesses may exist on the same SiC crystal, especially on the C-terminated surface where the growth process is much faster and generates multilayered, rotationally disordered graphene [40]. Prior to growth, both the surfaces are hydrogen etched to produce atomically flat surfaces [99]. Moreover, hydrogen intercalation of graphene grown on the Si-face is used to better decouple the atomic-thick material from the substrate and to achieve charge neutrality [100].

The optimization of the growth process on both the crystal faces are discussed in detail in the following sections.

The chemical vapor deposition approach is a surface-mediated process that exploits the catalytic behavior of transition metals to synthesize both single-crystals and polycrystalline graphene, subsequently transferred onto many different substrates. Nickel is usually preferred to grow multilayer graphene. Due to the appreciable solubility of carbon in nickel, carbon diffuses into the metal and then segregates to form non homogeneous multilayer films of graphene [97]. On the contrary, the low solubility of carbon in copper allows a self-limited growth that ceases as soon as the copper surface is covered with graphene. This results in a homogeneous single-layer film [41].

The two growth techniques to obtain large-scale highly crystalline graphene, namely thermal decomposition of SiC and CVD growth on copper, and the relative approaches specifically developed and optimized to produce the substrates used in this work will be described in detail in sections 2.3 and 2.4.

2.2 Graphene characterization

2.2.1 Atomic force microscopy

AFM is a scanning probe technique used for morphological characterization, force measurement and sample manipulation at the nanoscale. The principle of operation is to scan a flexible cantilever with a sharp tip back and forth across the sample’s surface with a feedback mechanism that enables a piezoelectric actuator to maintain the tip at a constant force or a constant height. A laser beam is focused on the cantilever and is reflected into a photodiode. During the scanning the cantilever bends and the laser beam deflection is measured by the photodetector. Typically, the AFM is operated in three modes that differ from each other by the tip and sample interaction forces: non-contact mode (attractive force), contact mode (repulsive force) and tapping mode (the cantilever oscillates at its resonant frequency lightly tapping on the surface). AFM is capable of producing a three-dimensional topography with a nanometric resolution. In addition to topography also sample's material properties and frictional forces can be detected by phase signal and lateral force signal respectively. Lateral force microscopy has been used for spatial mapping of frictional properties in partially graphitized SiC(0001) surfaces, providing a contrast between buffer layer and monolayer graphene [101]. Moreover, the AFM phase sensitivity to material changes allows to distinguish between different numbers of graphene layers from the contrast change [102,103].

In this work, the AFM images were taken using an AFM+ (Anasys Instruments) operated in tapping-mode using a standard tapping probe (PRE-EX-T125, Anasys Instruments). Typically, topography and phase channels were acquired to characterize the substrates.

2.2.2 Scanning electron microscopy

SEM is a technique that uses a focused high-energy electron beam to probe the sample surface. The interaction between the beam and the target sample generates electrons (e.g., either excited from the atoms of the sample or backscattered) that are used to gain information about the morphology and chemical composition of wide areas with a resolution of tens of nanometers. Indeed, secondary electrons and backscattered electrons, generated respectively by inelastic and elastic scattering interactions with the incident electron beam, are typically detected.

In this thesis, SEM imaging was performed at 5 keV using a Zeiss Merlin microscope, equipped with a field emission gun using an in-lens detector for secondary electrons.

2.2.3 Raman spectroscopy

Raman spectroscopy is a spectroscopic technique typically used to detect rotational, vibrational and other modes in a molecule. It measures the inelastic scattering generated by light interaction with the molecule. Each peak in Raman spectrum derives from a molecular or lattice vibration, giving information about molecular structure, crystallinity and residual stress.

The characteristic graphene Raman spectrum has two main peaks associated with phonon vibrational modes: the G band (~1580 cm^{-1}) and the 2D band (~2700 cm^{-1}). In case of disordered samples there is also the D band (~1350 cm^{-1}) [104,105]. The G band originates from a first order Raman scattering process. The 2D band is associated to a double resonance electron-phonon inelastic scattering process. When the process involves a phonon and a defect, we have the D band.

The position and shape of the 2D peak give an indication of the number of graphene layers. In particular, the single Lorentzian fitting of the peak with a full width at half maximum (FWHM) of < 30 cm^{-1} is characteristic of monolayer graphene. In bilayer and trilayer graphene, the 2D peak becomes broader and the fitting requires multiple Lorentzians. Moreover the 2D band energy increases significantly with increasing layer number [106]. In monolayer graphene, the 2D peak is two times more intense than the G peak. It has been demonstrated that the G to 2D band intensity ratio provides a good correlation with the number of graphene layers [107,108], even if considering the ratio alone could be not sufficient because it is also a benchmark for graphene doping [109].

Shifted G and 2D bands can also be associated with strain or doping or their combination [109–111]. The energy of the 2D peak blue-shifts in p-type doping and red-shifts in n-type doping, with respect to the case of pure undoped graphene. While the G-band of graphene shifts towards higher wave numbers both n and p type doping [109,112]. The separation of the strain and doping contribution from graphene's Raman spectra is complicated, due to G (ω_G) and 2D (ω_{2D}) band shifts dependency both on charges (n) and strain (ε). Lee *et al.* proposed a method to extract the contribution of charges and strain in the ω_G - ω_{2D} space using a vector model (Fig. 2.2) [110]. They demonstrated that each experimental point (P) can be decomposed into two components, whose shift is due to strain (e_T) or doping (e_H) to extract the strain and doping values from known reference values. The e_T and e_H vectors divided the ω_G - ω_{2D} space in four quadrants: Q1 for compressive strains and hole doping, Q4 for tensile strain and hole doping and Q2 and Q3 that are not allowed, because both n- and p-type doping cause an increase in ω_G.

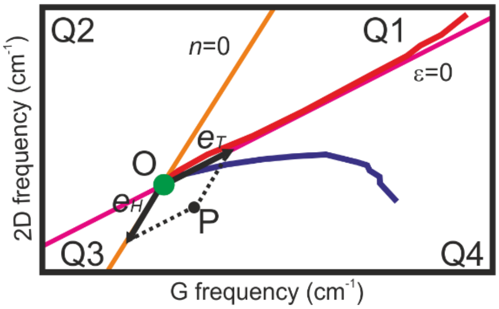

Fig. 2.2. **Vector model to separate the effect of doping and strain in graphene.** The green dot (O) represents the point (ω_{G0}, ω_{2D0}) that is not affected by strain and doping. The magenta line represents a strain-free graphene with varying doping (ε=0). The orange line represents doping-free graphene under uniaxial stress (n=0). Any experimental point (P) can be decomposed along the strain-free vector (e_H) and the doping-free vector (e_T). The blue and red lines are experimental trajectories for n-type and p-type graphene, respectively. Adapted from [110].

It has been demonstrated that the G and 2D band width can be used as a measure for the amount of nanometric scale strain variations. By analyzing the relation between the G and D line width, Neumann *et al.* found that the strain variations constituted a dominant contribution to the G and 2D lines broadening [111].

When graphene is grown on SiC, G and D bands are difficult to identify due to the Raman bands from the SiC substrate between 1200 and 1800 cm^{-1}. The SiC contribution is usually removed by subtracting a reference SiC spectrum, making both the bands visible [113], as depicted in Fig. 2.3.

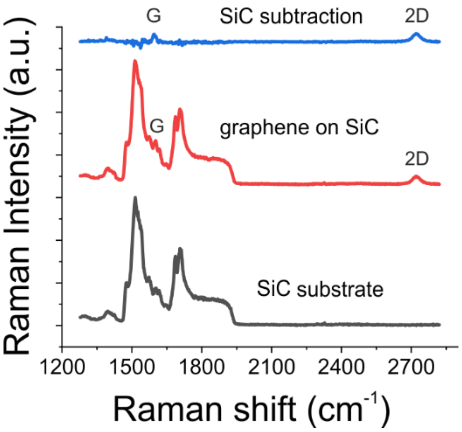

Fig. 2.3. **Raman spectra of SiC, graphene on SiC and graphene on SiC after background subtraction.**

When compared to micromechanically cleaved graphene, the 2D band FWHM of graphene on SiC is typically larger [106] and both G and 2D Raman peaks are strongly blue shifted (G band of ~10 cm^{-1}, 2D band ~39 cm^{-1}) due to the compressive strain caused by the SiC substrate [114]. Differently from the 2D band, the G band position and FWHM are not influenced by the number of layers [106].

In this this thesis, all the Raman characterizations were performed using a micro-Raman spectroscope, equipped with a motorized sample stage (inVia Raman, Renishaw) and a 532 nm laser with a spot size of around 1 μm in diameter. The laser power was kept at 1 mW with an acquisition time of 2 s, unless otherwise indicated.

2.3 Epitaxial growth on Silicon Carbide

SiC can assume different crystal structures, called polytypes. In this work, we grow graphene on the hexagonal SiC polytypes 4H- and 6H-SiC because they provide an ideal crystallographic symmetry for the growth of graphene (Fig. 2.4). By cutting a hexagonal SiC crystal along a plane perpendicular to the c-axis, two surfaces are formed, one terminated by Si atoms, known as (0001) or Si-face and the other terminated with C atoms, known as ($000\bar{1}$) or C-face (Fig. 2.4d). The growth of graphene has been carried out both on the Si-terminated and C-terminated surfaces of the SiC crystal with different results [96].

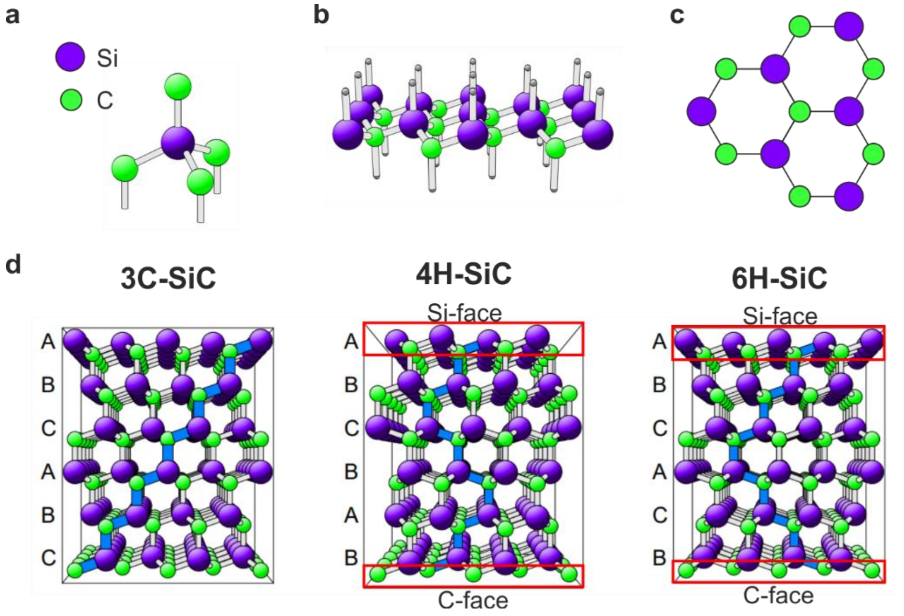

Fig. 2.4. **SiC crystal.** (a) The building block of the SiC crystal is a tetrahedron of four carbon atoms covalently bonded to a silicon atom in the center. (b-d) The SiC_4 tetrahedra forms the so-called bilayer and arranges in parallel planes of regular hexagonal networks whose stacking defines the different polytypes of SiC. (b) Hexagonal bilayer with Si and C in alternating tetrahedrally coordinated site. (c) Hexagonal frame of SiC bilayer. (d) Crystal structure of three different SiC polytypes: cubic 3C-SIC, hexagonal 4H-SiC and hexagonal 6H-SiC. The letter C or H denotes the cubic or hexagonal symmetry, while the number 3, 4 or 6 indicated the number of SiC bilayer within one stacking unit. One bilayer of Si and C has a 'c' dimension of 0.252 nm, that means that the 4H-SiC has a unit cell of 1 nm and the 6H-SiC of 1.5 nm [96,115]. The cubic polytype (3C-SiC) has an ABC, while the hexagonal polytypes 4H- and 6H-SiC have a stacking sequence of ABCB and ABCACB, respectively. The Si-face and C-face of both 4H- and 6H-SiC are highlighted with red rectangles. Adapted from [115]

2.3.1 Hydrogen etching

The crystalline quality of graphene grown on SiC by thermal decomposition strongly depends on the initial SiC surface quality. An as received optically polished SiC wafer usually presents high density of scratches on the surface arising from polishing damage (Fig. 2.5(a)). After a chemical mechanical polishing (CMP) the surface morphology is improved, but some residual polishing defects still remain (Fig. 2.5(b)). Hydrogen etching of SiC has been proposed as a method to reduce crystalline defects and achieve large atomically flat surfaces [99]. Due to the unintentional miscut of the surface even in on-axis substrates, the etching process produces a regular step array (i.e., reveals the atomic steps of the SiC surface), as shown in Fig. 2.5(c). On these atomically flat surfaces can be subsequently grown graphene of high crystalline quality [95].

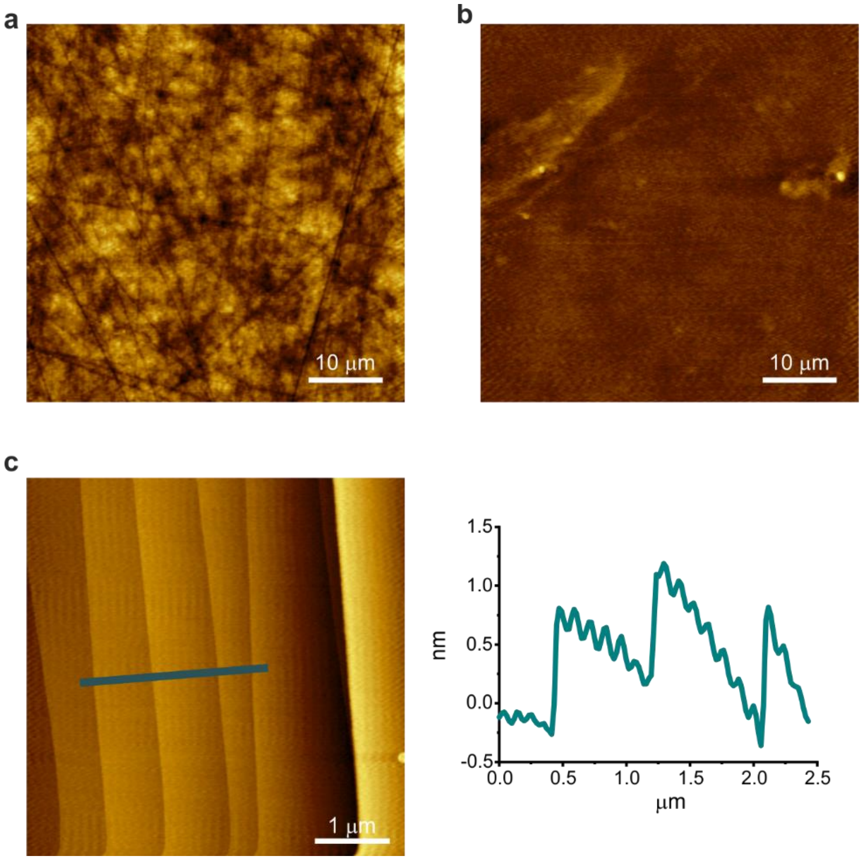

Fig. 2.5. **AFM images of 4H-SiC wafer.** (a,b) Before and (c) after hydrogen etching. (a) Optical polished C-face presents damages and deep scratches. (b) Chemical mechanical polished epi-ready Si-face SiC substrate is characterized by reduced roughness but still shows some polishing damages. (c) Hydrogen etched Si-face surface with atomically flat micrometric terraces separated by step (left). Step profile taken along the step flow reveals steps of unit cell height (1 nm) with an average distance of 1 µm (right).

In this work, we adopted hydrogen etching to etch both silicon and carbon basal planes of SiC crystals similar to what reported in Frewin *et al.* [116]. To this end, specific hydrogen etching processes were developed in our HT-BM Aixtron reactor. Etching was carried out by heating the samples under a flow of molecular hydrogen at a pressure of 450 mbar and at a temperature of around 1300 °C [44,117]. The high temperature causes silicon atoms sublimation exposing the underlying carbon atoms. They react with the hydrogen atoms forming hydrocarbons that leave the surface. The process continues until several hundred nanometers of SiC are removed, improving the surface morphology. Indeed, for this work, the presence of atomically flat terraces was instrumental to exclude the effects of macroscopic topographical features of the samples on the cell culture. In this way, only the physicochemical effect of graphene could be evaluated excluding the morphology of the substrate underneath.

2.3.2 Graphene obtained via thermal decomposition of SiC

As mentioned above, the two different basal planes of the hexagonal polytypes of SiC, show significantly different growth modes for graphene [96]. The graphitization process on the Si-face is characterized by the formation of an interface layer between the first graphene layer (monolayer graphene on SiC) and the underlying SiC substrate. This interface layer is known as zero layer or buffer layer and about 30% of the carbon atoms of this layer are covalently bound to the Si atoms of the Si-terminated substrate, with a periodicity of $\left(6\sqrt{3}\text{x}6\sqrt{3}\right)R30°$. The growth mechanism of graphene on the Si-face is via step-edge nucleation, due to an increased Si evaporation at the step edges [118]. Following Si sublimation, the buffer layer is released from the substrate as a new graphene layer and a new buffer layer is formed, maintaining the structure of the shifted interface layer, causing a 30° rotation of all the graphene layers with respect to the SiC substrate [119]. Moreover the buffer layer has a significant electronic influence, reducing graphene mobility and originating an intrinsic electron doping ($n \approx 1013\ cm^{-2}$) [40].

While on the Si-face it is easier to grow homogeneous mono and few-layer (up to 3) graphene, on the C-face is difficult to control the number of layers as the thermal decomposition process appears to take place in a rather quick and uncontrolled fashion [96]. In particular, the graphene layers typically obtained on the C-face lack a defined azimuthal orientation (i.e., turbostratic graphene) so that each layer behaves as an isolated graphene layer much less sensitive to SiC surface defects and is electronically decoupled from the neighboring ones. For this reasons, on this type of graphene, remarkable carrier mobilities have been measured [120]. In this work, we developed specific growth processes to obtain graphene on both SiC faces with atomic thickness and conclusively selected the ideal surface for our neural interface studies.

2.3.2.1 Graphene on the C-face of SiC

Knowing the difficulties to control the number of graphene layers on the C-face via conventional thermal decomposition growth, we developed a tailored CVD approach to improve the graphene surface topography and the uniformity of the layer thickness distribution. For subsequent neural interface studies in fact homogenous graphene samples shall be preferred to identify the physicochemical effect of graphene on cells. In the following text we report the comparison of the structural, chemical and electronic properties of the graphene obtained on the C-face of SiC with the two approaches (i.e., conventional thermal decomposition vs. CVD).

Following hydrogen etching, multi-layer graphene was grown on the C-face via thermal decomposition and via CVD. Like hydrogen etching, growth was carried out in a commercial resistively heated cold-wall reactor (HT-BM Aixtron reactor). Thermal decomposition was achieved by heating the samples in argon (Ar) atmosphere at a temperature of 1350 °C and a pressure of 780 mbar for 15 minutes, similar to what described in [40] and in our previous works [121–124]. CVD growth was achieved using methane (CH_4) as carbon precursor. Preliminary experiments were performed to optimize the growth process and it was found that addition of hydrogen in the gas mixture helped to reduce the formation of defects and to improve the homogeneity of the layer distribution. The sample was annealed at about 1350 °C within a 50% Ar and 50% H_2 atmosphere held at 780 mbar, while flowing 3 sccm of CH_4 for 5 minutes, similar to the procedure reported in our study [125].

After the thermal decomposition process, AFM analyses revealed a surface topography similar to that reported in previous works [126,127]. As shown in Fig. 2.6(a) and in the related line profile, pleats (or ridges) 2 to 10 nm high were observed. Such features are typically retrieved on graphene on SiC(000-1) (whereas they are not found on epitaxial graphene on SiC(0001)) and are due to the differences in expansion coefficients of SiC and graphene and to their weak coupling [126]. Most notably, the surface displayed a significant step bunching as visible in the representative AFM micrograph reported in panel (a). The related line profile shows a step with a height of about 40 nm. Adjacent micron-sized domains with different heights were also evidenced by the different grayscale contrast in the SEM micrograph in panel (b) and were found to be similar to those described previously [128,129]. Indeed, our growths further confirmed that thermal decomposition on the C-face takes place in a quick and uncontrolled fashion, thus yielding a relatively inhomogeneous surface. Although we found that the use of atmospheric pressure yields improvements with respect to the submicrometers domains typically obtained with UHV processes [44], the low surface energy of the C-face and the lack of a “growth enclosure” [129] most likely contributed to the obtained canyon-like morphology.

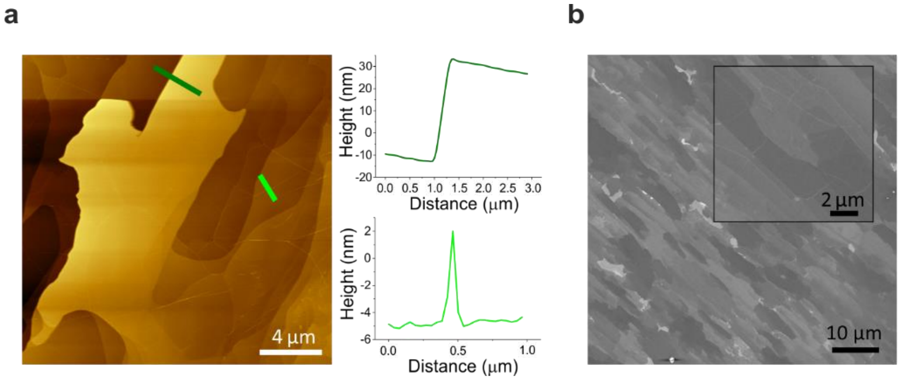

Fig. 2.6. **Graphene grown by thermal decomposition.** (a) AFM topography. Inset: profile analysis of a big step (top) and a ridge (bottom). (b) SEM image. Inset: high magnification of the same sample. Adapted from [44]

In the CVD grown samples, instead, differently from the thermal decomposition samples, the step-flow morphology was observed to be well-preserved and no dramatic variation in height within adjacent areas was observed, as reported in Fig. 2.7(a). Locally, one could appreciate inclusions of domains with an increased roughness (although still in the few-nanometers range). The representative SEM micrograph in Fig. 2.7(b) shows such inclusions as areas with a darker grayscale contrast. These inclusions most likely arise by a non-perfected CVD growth yielding the formation of sub-micrometer sized single-crystal domains. The grain size could possibly be increased by using higher hydrogen partial pressure during growth, an approach that needs to be investigated further.

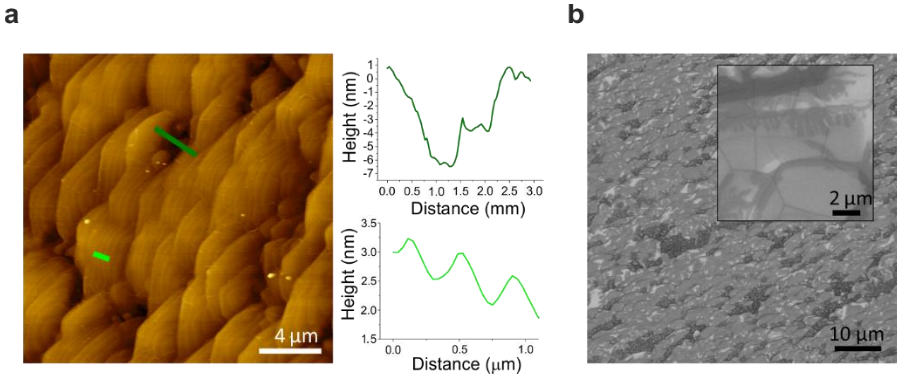

Fig. 2.7. **Graphene grown by CVD.** (a) AFM topography. Right insets: profile analysis of a rough area (top) and atomic steps (bottom). (b) SEM image. Inset: high magnification of the same sample. Adapted from [44]

We estimated the graphene thickness for the two different processes via Raman spectroscopy by measuring the attenuation of the representative SiC peak measured at ~ 1516 cm^{-1}. This peak is an overtone of the L point optical phonon and is attenuated in intensity when graphene overlayers are grown [130]. The remaining fraction of the substrate intensity after graphene growth is indicated as S and calculated as the multiplication needed to normalize the selected SiC peak in the bare SiC substrate to that of the graphene sample. The thickness (t) of the graphene overlayers is calculated as $t = -\ln(S)/2\alpha$ where α is graphene's absorption coefficient. Fig. 2.8 and Fig. 2.9 reports micro-Raman maps of the ratio S (panel (a)) and of the 2D-peak full width at half maximum (FWHM) (panel (b)) of the same area of a typical thermal decomposition sample and CVD sample, respectively. Values of S close to unity indicate a low attenuation and are therefore indicative of few-layer graphene. Instead, S values closer to zero are found for areas with thicker multilayer graphene.

In the map of the thermal decomposition sample in Fig. 2.8(a), the fractional SiC Raman signal S ranges from 0.9 to 0.4, thus indicating that the number of layers varies between 3 and 23. The 2D peak can be fitted with one Lorentzian, indicating a non-Bernal-stacked structure [131] with FHWM ranging from ~25 cm^{-1} to ~90 cm^{-1}. Areas with higher attenuation of SiC (lower values of S in Fig. 2.8(a)), due to an increased thickness of graphene, correlate well with wider 2D FWHM as previously reported in [131]. A characteristic spectrum after the subtraction of a reference SiC is shown in panel (c). The G peak was found at ~1580-1585 cm^{-1} and the 2D peak at ~ 2690-2720 cm^{-1}, both position ranges are comparable to those reported for similar samples in previous works [120,131]. Furthermore, absence of the disorder-induced D peak indicates high crystallinity of the grown graphene. Despite the good crystallinity, we evaluated such graphene samples as not suitable for the neural studies of this work due to the poor thickness control and canyon-like morphology.

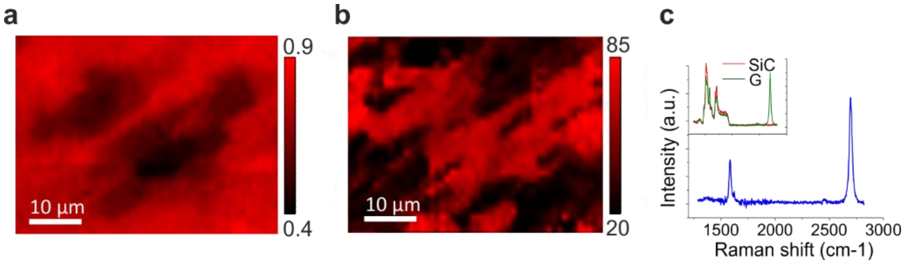

Fig. 2.8. **Raman characterization of graphene grown by thermal decomposition.** (a) Fractional SiC Raman signal (S) and (b) 2D FWHM Raman mapping. (c) Raman spectra of graphene after SiC signal subtraction (blue color). Inset: original spectrum without subtraction (green color) and SiC reference signal (red color). Adapted from [44].

The Raman mapping of S (a) and of the FWHM of the 2D peak (b) of a typical CVD-grown sample is showed in Fig. 2.9. In this case, the value of S was found to vary between 0.9 and 0.7, which indicates a much narrower graphene thickness distribution, ranging from 3 to 7 layers. As for thermal decomposition samples, the 2D peak can be fitted well with a single

Lorentzian presenting a FWHM ranging from ~40 cm^{-1} to ~60 cm^{-1}. A characteristic spectrum after the subtraction of a reference SiC is shown in panel (c). The G peak was found at ~1580-1595 cm^{-1} and the 2D peak at ~ 2690-2720 cm^{-1}. The larger variation in the G peak position observed in the CVD samples might be indicative of graphene doping and needs to be investigated further. The D peak was generally absent and found only very occasionally, in spectra presenting a low 2D peak. This indicates that also in this case a high crystallinity is achieved.

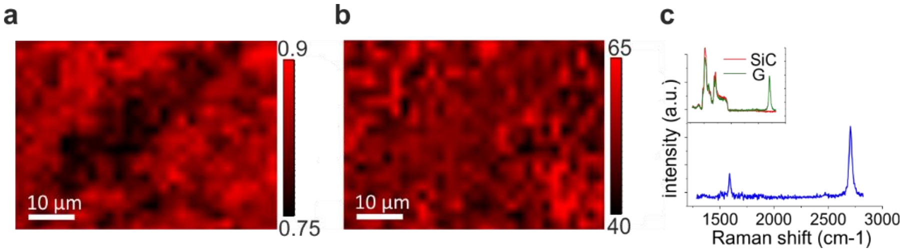

Fig. 2.9. **Raman characterization of graphene grown by CVD.** (a) Fractional SiC Raman signal (S) and (b) 2D FWHM Raman mapping. (c) Raman spectra of graphene after SiC signal subtraction (blue color). Inset: original spectrum without subtraction (green color) and SiC reference signal (red color). Adapted from [44].

By adopting a similar CVD process, a high number of graphene layers (up to 90) with good crystallinity were synthesized, which were used for investigating absorption in the THz [125,132]. As these samples were found to display saturable absorption, CVD-grown multi-layer graphene on SiC(000-1) might represent a favorable platform for the implementation of novel graphene-based mode-locked THz lasers [125].

Even if the CVD approach helped in improving thickness homogeneity and crystallinity, for cell culture experiments we decided to use graphene grown on the Si-face of SiC thanks to the better quality and thickness control, as it will be discussed in the following text.

2.3.2.2 Graphene on the Si-face of SiC

When we started to implement the thermal decomposition growth on the Si-face of SiC in our HT-BM Aixtron reactor, two different experimental approaches were already reported in literature. It was in fact known that different graphene quality could be obtained when annealing SiC(0001) in ultra-high vacuum (UHV) or under Ar atmospheric pressure [95,96,133]. Differently from UHV-grown graphene that was notoriously obtained in small domains of few hundreds of nanometers, Ar-grown graphene presented much larger domain sizes of several tens of microns thanks to a more controlled silicon sublimation [40]. We implemented both the UHV and Ar growth processes in our HT-BM Aixtron reactor and obtained the expected different morphologies as shown in Fig. 2.10.

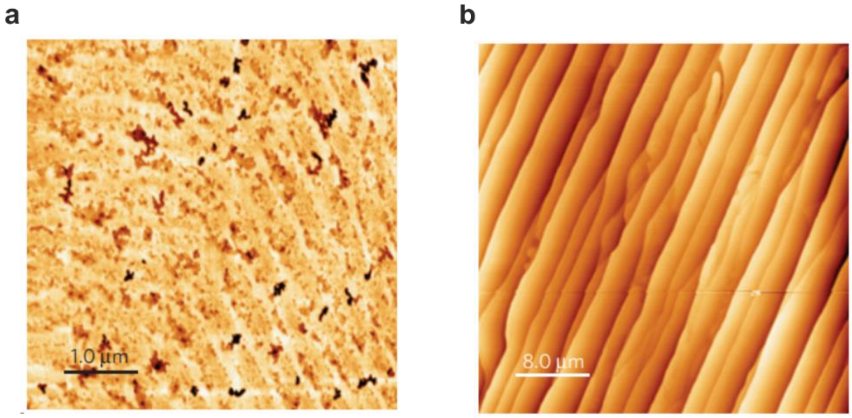

Fig. 2.10. **Morphology of epitaxial graphene growth in UHV and in Ar atmosphere.** (a) AFM image of monolayer graphene on SiC formed by annealing SiC in UHV. (b) AFM image of monolayer graphene on SiC formed by annealing SiC in argon. Adapted from [40].

In this work, in order to assure experimental reproducibility and deeply understand the graphene effect on cell viability and morphology, we carried out graphene growth under Ar atmospheric pressure. We checked each sample to guarantee a reproducible morphology and quality and exclude spurious effect on the cell culture. We optimized the selected growth process to assure a uniform graphene coverage of the substrate and reduce the formation of defects that could influence the cell morphology.

By changing the annealing temperature and time it was possible to control the number of graphene layers, ranging from mono-, bi- and few-layer graphene. The growth of buffer layer was performed at lower temperatures, ranging from 1200 °C to 1250 °C and a pressure of 780 mbar for 5-10 min. Monolayer graphene growth was performed by raising the temperature to 1300-1330 °C, as described in our previous works [57,117,134].

Assessment of the distribution of the number of layers was conducted via Raman spectroscopy. The graphene sheet was also characterized by AFM (Fig. 2.11(a,b)) and SEM (Fig. 2.11(c)) that showed the typical step-terrace structure of the graphitized SiC surface and the presence of graphene with different thicknesses within the terrace. The correlation of the AFM image with the two-dimensional spatial distribution of the width of the 2D Raman peak (Fig. 2.11(d, top)), and the ratio of 2D and G peak intensities (Fig. 2.11(d, bottom)), revealed the monolayer character of the graphene on the terraces. While bilayer inclusions were typically located at the terrace edges [117,135].

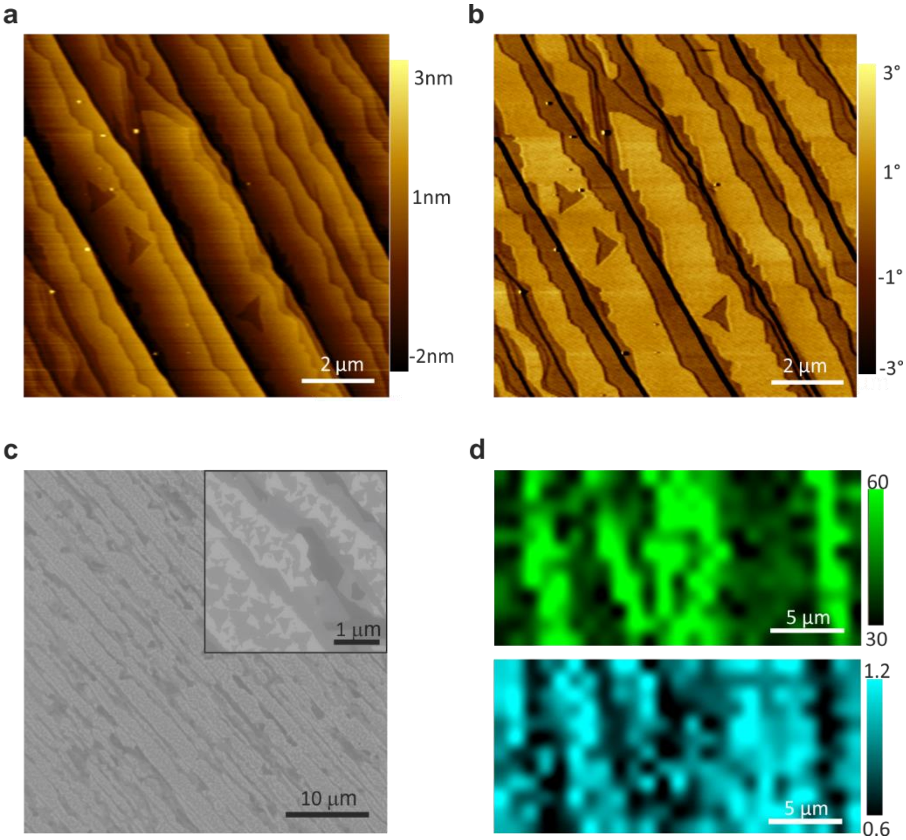

Fig. 2.11. **Epitaxial graphene characterization via AFM and SEM.** (a,b) Tapping mode AFM topography (a) and phase signal (b) of graphene grown on Si.face SiC. Height signal showing the terraces arising from hydrogen etching. The contrast in the phase signal is due to monolayer graphene (brighter) or bilayer graphene (darker). (c) SEM image of a mono-bilayer graphene sample with an inset showing a zoom-in. (d) 2D peak width (upper figure) shows a monolayer character on the terraces (darker areas) and bilayer inclusions in the proximity of the steps (lighter areas). The bilayer inclusions are confirmed by an increase in the ratio of G and 2D peaks intensity (lower figure).

To control better the SiC sublimation rate and obtain more homogeneous graphene samples, we annealed the samples with the etched face down. It should be noted that graphene grows not only on the face of interest, but also on the opposite face, thus yielding multilayer defective graphene on the C-face which caused the samples to be optically dark: a hurdle for the optical microscopy studies of our work. To solve this problem, we implemented hydrogen intercalation of buffer layer graphene similar to what reported in

Riedl *et al*.. In fact, by growing buffer layer graphene and then intercalating hydrogen at the interface of the buffer layer with SiC(0001) one could obtain quasi-free-standing monolayer graphene completely transparent (i.e., the transparency issue of the sample could be solved thanks to the lower processing temperatures involved). Specifically, hydrogen intercalation is a technique that uses molecular hydrogen to break and saturate the bonds between C and Si, releasing the buffer layer (Fig. 2.12(a)) that turns into a quasi-free standing monolayer graphene (QFSMG) (Fig. 2.12(c)). In the same way monolayer graphene (Fig. 2.12(b)) turns into a decoupled bilayer (Fig. 2.12(d)) [100].

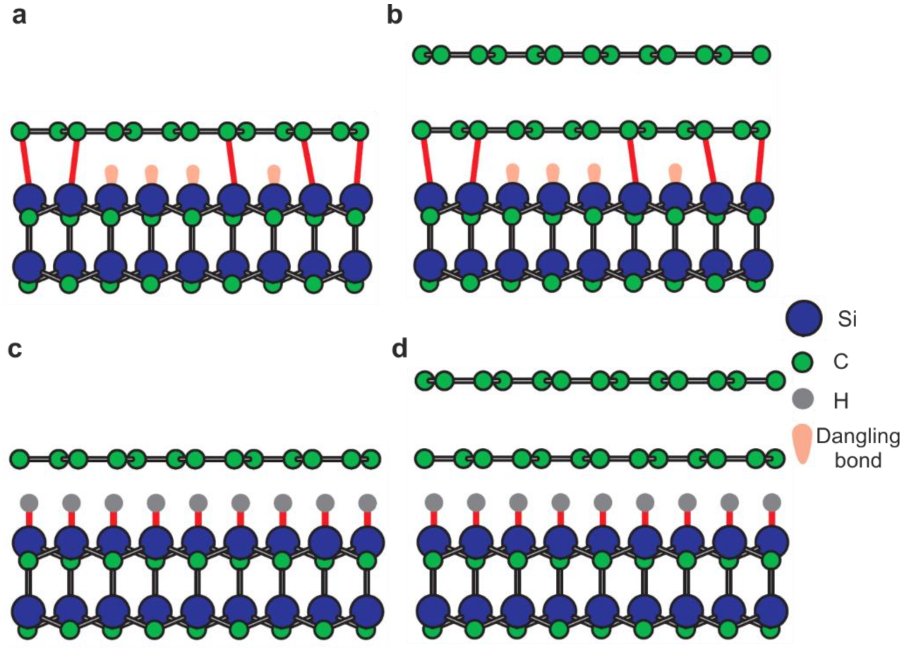

Fig. 2.12. **Structural model of buffer layer, monolayer graphene and QFSG graphene.** Schematic side view of (a) buffer layer with the carbon layer partially covalently bonded to the Si atoms of the SiC substrate, (b) as-grown monolayer graphene, (c) quasi-free standing monolayer graphene and (d) quasi-free standing bilayer graphene formed after hydrogen intercalation. Hydrogen atoms saturate the Si atoms of the Si-face SiC, releasing the buffer layer (c) and the monolayer (d) into a quasi-free standing graphene. Adapted from [100].

The process was carried out by exposing the grown buffer layer samples to molecular hydrogen at atmospheric pressures and temperatures between 600 °C and 1000 °C, typically for 10 minutes as reported in our previous work [136].

2.4 Chemical Vapor Deposition on copper

In chemical vapor deposition, hydrocarbon gases such as CH_4 represent the carbon precursor that decomposes at high temperature on a catalytic metal surface such as nickel or copper. As abovementioned, the lower carbon solubility in copper provides a self-limited growth mechanism that allows for the production of a homogeneous single-layer film [41]. At temperature around 1000 °C hydrocarbon molecules in contact with the surface decompose; the carbon atoms arrange into the honeycomb structure and the volatile species desorb. The adatoms (adsorbed C atoms on Cu surface) migrate on the surface and aggregate into small nuclei that expand depending on the rates of adatom diffusion and the deposition flux of C atoms [137]. Graphene nucleation density is the result of competition between the adatom species mobility and their desorption rate [138].

The large graphene films obtained via CVD techniques are typically polycrystalline, with a grain size of tens of microns that can degrade graphene's electronic properties due to the presence of grain boundaries [139]. For this reason, great effort has been given to realize single-crystal graphene without grain boundaries or to increase the domain size in polycrystalline graphene. In recent years, it has been shown that growing graphene in the presence of oxygen can limit the number of nucleation sites by passivating Cu surface active sites. Moreover, oxygen affects the graphene growth kinetics, allowing a diffusion-limited growth mechanism that enables the formation of centimeter-scale single-crystal graphene domains [140]. The nucleation can be further limited by reducing copper surface contamination and roughness with electrochemical polishing treatment [98]. Our group developed a process for quick production of large grain graphene in a commonly used commercial CVD reactor. It consists in reducing the nucleation density by annealing oxidized Cu foils in an inert Ar atmosphere and by employing a sample enclosure that limits the impingement flow. In addition, through a ‘pocket’ configuration consisting in manually folding of the copper foil, larger grain can be obtained [98]. Differently from epitaxial graphene on SiC that does not need transfer, CVD graphene is usually transferred from the growth substrate to the target substrate. One of the most common techniques is represented by the wet poly-methyl-methacrylate (PMMA) transfer techniques [41,98].

2.4.1 CVD graphene synthesis

In this thesis, graphene was synthesized using a 4-inch Aixtron BM Pro cold-wall reactor and adopting electropolished Cu foil (purity 99.99%, Alfa-Aesar). The growth process we implemented was similar to that developed in our group to synthesize large single-crystal graphene on foil [98]. However, in our case, we aimed at obtaining large-grain polycrystalline graphene so to have a complete coverage of the samples adopted for neural studies (i.e., single-crystals maximum size achievable in our reactor is 4 mm). The optimized process consisted in four main steps: (i) temperature ramp-up, (ii) annealing, (iii) growth and (iv) cool-down. The typical temperature profile of a growth process is shown in Fig. 2.13(a).

Specifically, the sample was placed on the graphite heater and enclosed using a quartz disk suspended on graphite spacers 6 mm thick (Fig. 2.13(b)). The copper foil was then annealed in Ar for 10 min to preserve the oxidation of the surface (i.e., achieved thanks to electropolishing) so to increase the size of the graphene domains. The growth was performed introducing methane and hydrogen for 30 min at a temperature of 1020-1040 °C and a pressure of 25 mbar. The gas flow rates were 2 sccm of CH_4, 20 sccm of H_2 and 980 sccm of Ar. At last, the chamber was cooled down under argon flow to a temperature of 120 °C before opening the chamber and exposing the sample to air. Average domain size of graphene was assessed to be 20-30 µm by SEM analysis (Fig. 2.13(c)). It should be noted that this size is larger than that retrieved in commercially available samples and this specifically-prepared higher-quality samples allow for an improved graphene uniformity and are consequently better suited for our neural interface studies.

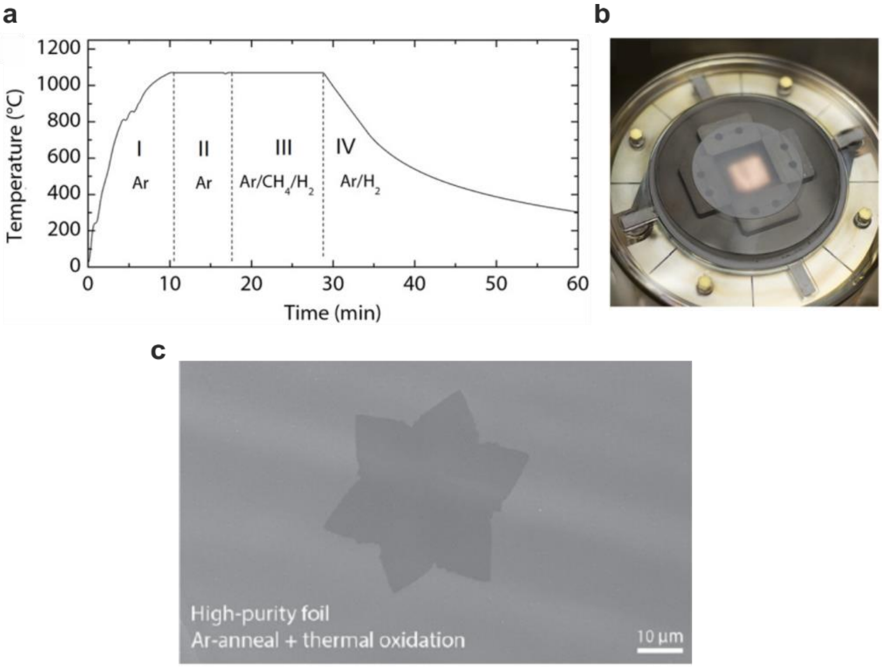

Fig. 2.13. **CVD graphene synthesis in an Aixtron BM Pro cold-wall reactor.** (a) CVD graphene synthesis temperature steps: (I) temperature ramp-up, (II) annealing, (III) growth and (IV) cool-down. (b) Quartz disk suspended on graphite spacers used to enclose the copper sample. (c) SEM image of a large isolated single crystal grown on high-purity Cu foil after intentional oxidation. Adapted from [98].

2.4.2 Transfer to glass coverslip

In this thesis we have specifically developed an approach to transfer graphene and integrate it with microfluidic chambers for compartmentalized cell culture. The transfer of single layer graphene (SLG) on glass was performed using the standard wet etching technique that deposits a polymer on the SLG/Cu foil in order to manipulate easily the thin graphene layer after substrate etching [41,98].

Fig. 2.14 illustrates the schematic diagram of the transfer process of SLG on copper (Fig. 2.14(a)) on glass coverslip. Before the transfer, the glass coverslip is cleaned using acetone and isopropanol and treated with oxygen plasma for 5 min at 100 W. A layer of PMMA (AR679.04, 4% in ethyl lactate) is spin coated on the SLG/Cu foil at 4000 rpm for 1 min and heated for 1 min at 90 °C (Fig. 2.14(b)). The graphene grown on the back-side of the Cu foil is removed by reactive ion etching (RIE) for 1 min, by using a Sistec RIE system with a gas flow rate of 80 sccm of oxygen and 20 sccm of argon. The PMMA/SLG/Cu foil is etched overnight using 0.1 M solution of iron chloride ($FeCl_3$) (Sigma-Aldrich) or 0.1 M solution of ammonium persulfate (APS) (Sigma-Aldrich) leaving the PMMA/SLG floating on the surface of the etchant solution (Fig. 2.14(c)). The membrane is repetitively rinsed in deionized (DI) water to remove any residuals of the Cu etchant. When $FeCl_3$ is used, the membrane is also treated for 10 min with HCl (%) to remove iron residuals, followed by several rinsing in DI water. PMMA/SLG membrane is then transferred on a glass coverslip. The glass coverslip is then used to lift the floating PMMA/SLG membrane and is left under the hood until the sample is completely dried (Fig. 2.14(d)). Finally, the sample is washed with acetone for at least 2 h to remove the PMMA, rinsed with isopropanol and blow dried with nitrogen (Fig. 2.14(e)).

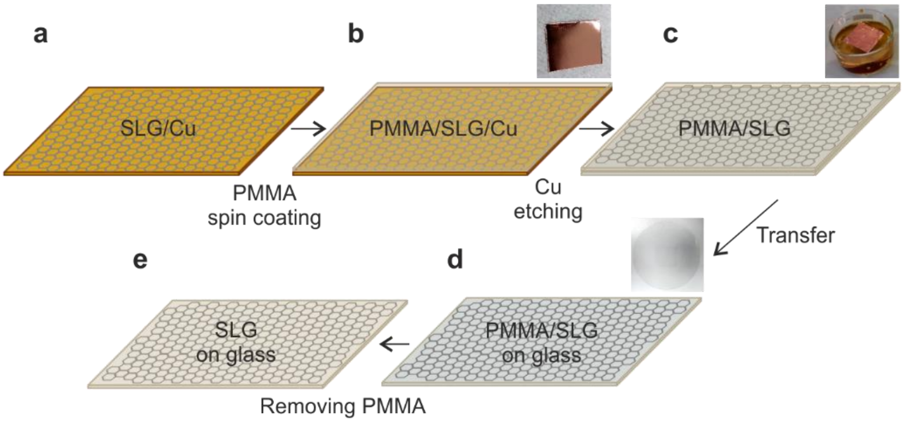

Fig. 2.14. **Schematic of the method for transferring graphene on glass using the wet etching technique.** (a) CVD-single layer graphene sample grown on Cu foil. (b) PMMA layer spin coating on top of graphene (c) Etching of the Cu metal using $FeCl_3$ or APS solution. (d) Transferring of graphene film to a clean glass coverslip. (e) PMMA removal by acetone

The obtained samples were analyzed by using AFM and Raman spectroscopy to check graphene quality. After an optical inspection, the samples prepared with the $FeCl_3$ solution appeared less clean and covered with polymer residuals. When iron chloride was used, even after an overnight in acetone the sample was covered with PMMA residuals. This was confirmed also by AFM topography images (Fig. 2.15(a)). A treatment with pure acetic acid for 1 h was used to clean the surface. The bigger residuals were removed and a decreased roughness was observed (Fig. 2.15(b)). On the contrary, the samples transferred with APS were optically cleaner and the AFM analysis showed a reduced PMMA contamination comparable with the one observed in the $FeCl_3$ transfer after acetic acid treatment (Fig. 2.15(c)).

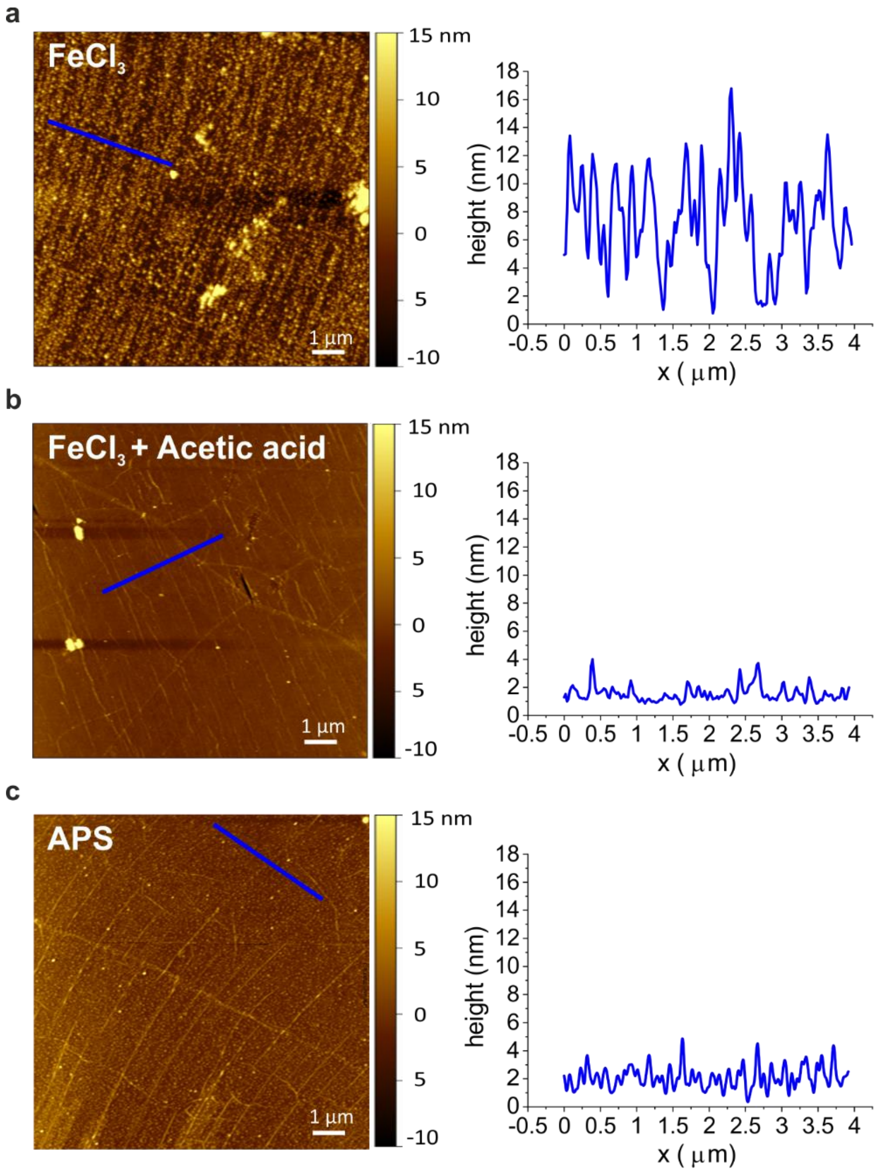

Fig. 2.15. **AFM topography with the relative line profile of CVD graphene transferred on glass via wet transfer.** (a) PMMA residuals are left on graphene after copper etching in $FeCl_3$. (b) PMMA residual are removed by acetic acid treatment resulting in a clean graphene surface. (c) Reduce PMMA residuals on graphene after copper etching in APS solution.

We observed also a difference in the Raman spectra of the samples obtained with the two different transfer protocols. The spectra of the samples transferred with APS showed a narrow 2D peak (FWHM ~29-34cm^{-1}) while the other had a larger FWHM of 30-40 cm^{-1}.

Therefore, in all the experiments further discusses in this work where CVD graphene is adopted (i.e. DRG studies), we decided to use the developed protocol of APS transfer. This allowed us to reduce the number of transfer steps, to obtain samples with high crystallinity and maximum cleanliness, and ultimately to avoid spurious effect in our neural interface studies due to PMMA contamination.

However, APS-transferred graphene showed sometimes a reduced adhesion to the substrate, resulting in wrinkling and folding of graphene when it was rinsed with water (Fig. 2.16).

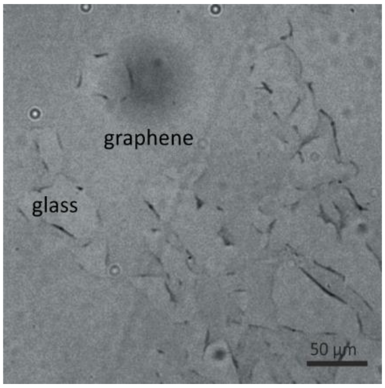

Fig. 2.16. **Optical micrograph of graphene detachment from the glass substrate after submersion in water.**

This has been ascribed to irregular diffusion of water underneath the graphene [141]. Unfortunately, the contact with water it is a fundamental step when graphene is used in the cell culture process. Water is used to rinse the samples after the cleaning with ethanol and it is the main component for the coating solution and media. To increase the PMMA/SLG film adhesion to the substrate, all the samples used in this work were annealed at 165 °C for 3h and then washed with acetone for at least 2 h to remove the PMMA. This step was followed by an annealing at 120 °C for 1 h to further improve the adhesion [142].

3 Investigation of the potential of epitaxial graphene as a conductive peripheral neural interface

In this chapter, the potential of graphene as a conductive peripheral neural interface is investigated. Epitaxial graphene obtained via thermal decomposition on SiC [95] was selected as the ideal substrate for such investigations. In fact, epitaxial graphene on SiC combines high crystalline quality, scalability, thickness homogeneity and an extreme cleanliness.

Graphene was used as a substrate for two cellular models: PC12 cells and DRG sensory neurons. The PC12 cell line is a non-neuronal cell line developed from a pheochromocytoma tumor of the rat adrenal medulla, that is able to differentiate upon NGF stimulation and constitutes a widely-used model for peripheral sympathetic neurons [143]. DRG sensory neurons are a widely used model to study axonal regeneration. They are pseudo-unipolar neurons that have one axon with two branches: the peripheral branch innervates the sensory organs and regenerates readily when injured, while the central branch extends into the spinal cord and does not regrow after spinal cord injury. Nevertheless, if the peripheral injury takes place before the central injury, the central branch is characterized by an improved regenerative response [43].

First, we performed an unprecedented analysis aimed at revealing how the typical polymeric coatings for neural cultures distribute on graphene at the nanometric scale. Previous studies emphasized the possibility of certain neurons to survive in uncoated graphene [87]. However, this is very unlikely to occur physiologically because neurons produce their own extracellular matrix (ECM) even in culture conditions. We investigated how ECM-like components distributed onto graphene, a non-trivial task given the high hydrophobicity and flatness of this material. We checked the homogeneity and quality of different polymeric coatings to identify the most suitable to adopt for the reported cultures.

DRG neurons were also interfaced with bare graphene to examine their interaction with graphene per se, in the absence of a coating. Optical microscopy was used to investigate neurite length, cell number and differentiation, while viability assays were used to assess cytocompatibility. We compared results on monolayer graphene on SiC (G) with the ones on four possible control substrates: hydrogen etched SiC (SiC), gold coated glass coverslip (Au), glass coverslip (Glass) and polystyrene plate (well). The latter, being routinely used in cell culture procedures, was used as classic control. SiC controls were implemented since graphene was grown directly on such substrates, which display a good biocompatibility [144] and present prospects for neural implants [145]. Finally, glass coverslips were coated with a very thin layer of gold to mimic the graphene layer grown on SiC. We used gold substrates as conductive controls, as gold, together with platinum (Pt, especially its porous form Pt-black), titanium nitride (TiN) and iridium oxide (IrOx), is typically interfaced with neurons in the fabrication of biomedical electrodes [146,147]; Pt-Black, TiN and IrOx are useful for the increased effective surface [148].

This chapter contains information published in the peer-reviewed work with authors D. Convertino, S. Luin, L. Marchetti, C. Coletti: “Peripheral neuron survival and outgrowth on graphene”. Frontiers in Neuroscience 12(JAN):1–8 (2018). Experiments and data shown in each figure were performed and analyzed by D. Convertino.

3.1 Materials and methods

3.1.1 Sample preparation

Graphene on SiC was prepared by adopting a technique which allows to obtain QFMLG [100].

The samples were cut from 1 degree off-axis 4H-SiC(0001) wafers (SiCrystal, W4H76N-1-PO-350), in square of about 6 x 6 mm^2. Before etching, samples were cleaned from organic and metallic contamination and the oxide layer was removed [149] with the following steps:

(i) sonication in acetone and isopropanol for 5-10 min to remove organic residuals;
(ii) DI rinse;
(iii) immersion in Piranha solution (H_2SO_4:H_2O_2 = 4:1) for 10 min to remove organic contamination;
(iv) DI rinse;
(v) immersion in HF solution (H_2O:HF (49%) = 9:1) for 1 min to remove the native oxide layer;
(vi) DI rinse;
(vii) blow dry with nitrogen.

Once treated, SiC wafers were hydrogen etched in our HT-BM Aixtron reactor to remove the polishing scratched and cover the surface with ordered terraces. The samples were heated under a flow of H_2 and Ar at a temperature of 1250 °C and a pressure of 450 mbar for 5 minutes. Few minutes were sufficient to remove polishing scratches.

Buffer layer graphene was obtained via thermal decomposition of H-etched wafers. The samples was placed in a commercial resistively heated cold-wall reactor and annealed in vacuum at 900 °C for 10 min to remove adsorbates from the samples. The sample was then annealed in Ar atmosphere at around 1250-1300 °C for 5-10 min.

The buffer layer samples were subsequently treated in hydrogen to obtain QFMLG. The intercalation was performed by annealing the samples for 10 min at 900 °C in ultra-pure molecular hydrogen at atmospheric pressures [136].

The controls adopted in the experiments were:

(i) Hydrogen etched SiC(0001) dices, the same used for graphene growth.

(ii) Gold coated glass coverslips. Glass coverslips were cleaned using acetone and isopropanol in ultrasonic bath. The samples were then metallized with a thin layer of gold (4 nm) in a thermal evaporator (Sistec) using 2 nm of titanium as adhesive layer.

(iii) Bare glass coverslips.
The samples were treated overnight with 65% nitric acid (Sigma-Aldrich). This is a standard procedure used not only to clean the substrate but also to etch the surface to increase cellular attachment.

(iv) Polystyrene tissue-culture treated 48-well plates (Corning).

The dimensions of all the substrates were about 6 × 6 mm^2.

3.1.2 Surface functionalization

Graphene and controls samples were coated with different polymeric solutions suggested for the target cell cultures. The substrates were incubated with the coating solutions at 37 °C at different incubation times, i.e., 1, 4 and 12 h, to test a possible effect of the time on the resulting topography. The following solutions were tested: 100 µg/ml PLL solution in water (P4832, Sigma-

Aldrich), 200 µg/ml Collagene Type I (Sigma-Aldrich) in DI water, 30 µg/ml PDL (P1149, Sigma-Aldrich) in PBS, 30 µg/ml PDL and 5 µg/ml laminin (Life Technologies) in PBS. The samples were incubated with the coating solution at 37 °C for 1, 4 and 12 h and rinsed three times in DI water before analyzing their topography via AFM.

AFM analyses were performed to investigate the morphology of both such coatings on graphene and the controls and compared with the one without the coating. Tapping mode was used to scan several areas up to 10 x 10 µm wise. AFM micrographs were analyzed using the software Gwyddion 2.45.

3.1.3 PC12 and embryonic DRG neurons cell culture

PC12 cells (ATCC CRL-1721TM) were maintained in a humidified atmosphere at 37 °C, 5% CO_2 in RPMI 1640 medium supplemented with 10% horse serum, 5% FBS, 1% penicillin/streptomycin and 1% L-glutamine (Gibco). Cells were plated at ~40–60% confluency onto the substrates previously coated with 100 µg/ml PLL in water (Sigma-Aldrich). Differentiation was achieved using two different procedures: (1) direct addition of 50 ng/ml NGF (Alomone Labs) in complete cell medium after seeding; (2) a 5–6 days priming with 15 ng/ml NGF in complete medium, followed by seeding on the substrates with 50 ng/ml NGF in RPMI medium supplemented with 1% horse serum, 0.5% FBS, 1% penicillin/streptomycin and 1% L-glutamine. In both cases, 2/3 of the medium was renewed every 2–3 days. With the second procedure an improved differentiation was observed.

Rat embryonic dorsal root ganglion neurons (R-EDRG-515 AMP, Lonza) were maintained in a humidified atmosphere at 37°C, 5% CO_2 in Primary Neuron Basal medium (PNBM, Lonza) supplemented with L-glutamine (1%), antibiotics (0.1%) and NSF-1 (2% final concentration). Neurons were plated on the substrates previously coated with a PBS solution of 30μg/ml PDL (Sigma-Aldrich) and 5μg/ml laminin (Life Technologies). For the survival of DRG neurons, 100 ng/ml of NGF (Alomone Labs) were added to the media). Since 24 h after seeding, 25μM AraC (Sigma-Aldrich) was added for inhibition of glia proliferation. Half of the medium was replaced every 3–4 days.

3.1.4 PC12 cell morphometric analysis and viability

The cells were observed at different time points using an inverted microscope equipped with a 20x/40x magnification objective (Leica DMI4000B microscope). Typically, 10 fields per sample were acquired to perform morphometric analysis of PC12 differentiation.

Three parameters were measured as previously reported [150]:

(i) the percentage of differentiated cells (Diff), determined counting the number of cells with at least one neurite with a length equal to or longer than the cell body diameter;
(ii) the average number of neurites per cell in the field (av. neurites/cell);
(iii) the mean neurite length measuring the longest neurite of each differentiated cell in the field (length).

PC12 cell viability was assessed with the Cell counting Kit-8 assay (CCK-8, Sigma-Aldrich), based on quantification of WST reduction due to the metabolic activity of viable cells. Samples were prepared according to the manufacturer’s instructions and measured at the GloMax® Discover multiplate reader (Promega). The results are reported as % over the polystyrene well, considered as control. All the experiments were repeated at least twice independently.

3.1.5 Statistical analysis

For all the experiments, we performed two independent cultures with two biological duplicates each. For the morphometric analysis of the PC12 cells, for each substrate we analyzed at least 200 cells (n_c=number of cell) from selected fields (n_f= number of field) of the four replicates (two biological duplicates per culture) obtained with a 40x objective (Au: n_f=17, n_c=203; Glass: n_f=33, n_c=1106; G: n_f=42, n_c=877; SiC: n_f=35, n_c=1004; well: n_f=37, n_c=724). For the DRG neurons we analyzed nf fields using a 40x objective for a total of n_c cells for each substrate (day1: Au, n_f =13, n_c=67, Glass: n_f =14, n_c=75; G: n_f =13, n_c=29; SiC: n_f =12, n_c=35; day2: Au, n_f=16, n_c=89, Glass: n_f =13, n_c=100, G: n_f=12, n_c=34, SiC: n_f =11, n_c=37). The number of cells analyzed (nc) is the total pool of the four experiments. All data are expressed as the average value (mean) ± standard error of the mean (s.e.m.) unless stated otherwise. Data were analyzed by using Origin Software and nonparametric Kruskal–Wallis test with Dunn’s multiple comparison test were used for statistical significance with $^*p < 0.05$, $^{**} p < 0.01$ and $^{***} p < 0.001$.

3.2 Surface characterization

Optical microscopy was used for quick inspection of the substrates, to select graphene samples free form macroscopic defects. The topography of the samples as well as the graphene number of layers and quality were assessed by both AFM and Raman spectroscopy. Fig. 3.1(a) reports the characteristic AFM topography of an atomically flat intercalated graphene sample, presenting nanometric steps. Fig. 3.1(b) shows the Raman spectrum of an intercalated graphene sample, obtained using a 532 nm laser and a 50x objective lens. The absence of the D band indicated high quality graphene. The 2D peak has a narrow FWHM of 28 cm^{-1} and can be fitted with a single Lorentzian, characteristic of monolayer graphene. The 2D peak position and FWHM distribution in a large area are reported in Fig. 3.1(c). The maps reveal that the 2D peak and FWHM are very homogeneous across the whole area. The broadening of the peak in some regions indicates contributions of bilayer graphene. While the energy of the peak, blue-shifted with respect to the case of pure undoped graphene, indicates a p-type doping, characteristic of a QFMLG.

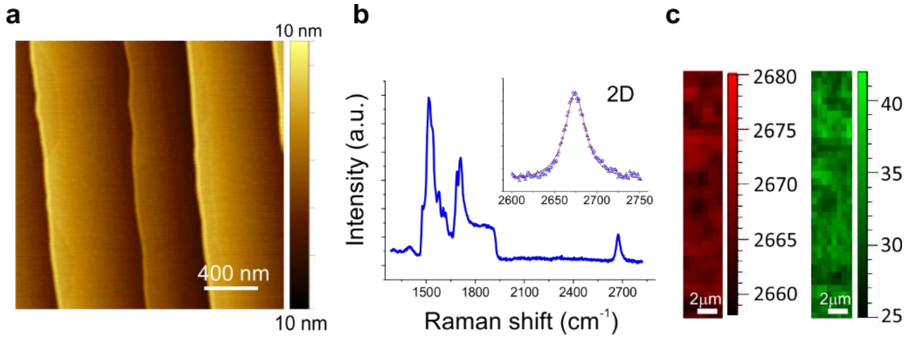

Fig. 3.1. **Graphene characterization via AFM and Raman spectroscopy.** (a) Characteristic AFM topography of an intercalated graphene sample, showing atomically flat terraces separated by steps. (b) Raman spectrum of an intercalated graphene sample. The insert shows the single Lorentzian fitting of the 2D peak, with a narrow FWHM of 28 cm-1. (c) 2D peak position (left) and FWHM (right) distribution in a large area. Adapted from [45]

We deposited a thin gold layer to have a conductive material that mimic graphene thickness. We chose to deposit gold on glass to mimic the graphene conductive layer on the SiC substrate. We checked also if following gold evaporation on SiC we could have a flatter surface resembling graphene morphology. We obtained a roughness comparable to that obtained on glass due to clustered deposition. Fig. 3.2 shows the AFM topography measured on SiC and glass after the evaporation of 4 nm of gold, with 2 nm of Ti as adhesive layer. Root-mean-square (RMS) calculated on 1x1 µm area was comparable for gold-coated glass and gold-coated SiC (0.6 nm). For this reason, we decided to use glass as substrate for gold evaporation.

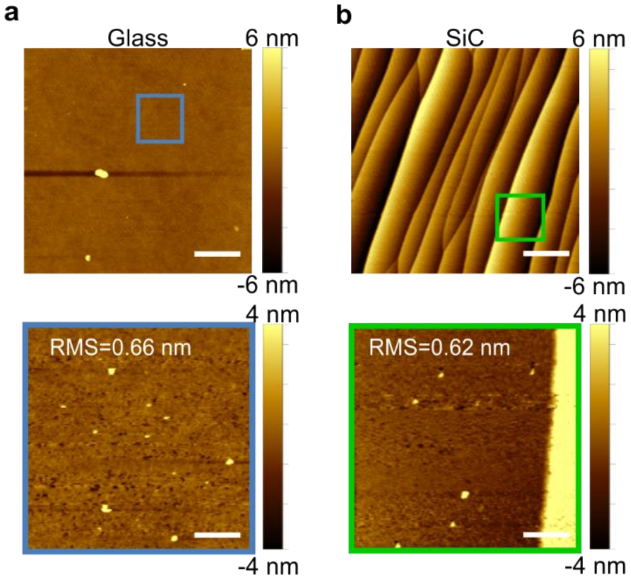

Fig. 3.2. **Gold samples morphology.** AFM topography of (a) glass and (b) SiC after gold evaporation (first row) and zoomed region (second row), with the RMS values. Scale bars: 1 µm for the first row and 200 nm for the second row.

Before cell culture, all substrates were sterilized by 30 minutes immersion in 96% ethanol and then rinsed several times with DI water.

3.3 Nano-resolved analysis of polymeric coating of epitaxial graphene and control substrates

NGF-induced neurite outgrowth of PC12 cells is favored by their adhesion on a substrate. This is typically achieved by coating the dish surfaces with polymers such as poly-L-lysine or biologically derived collagen [143]. We applied a water solution of both these coatings to all substrates adopted for our cultures and analyzed by AFM the quality and homogeneity of the coatings after different incubation times, i.e. 1 hour, 4 hours and 12 hours. Panels (a) and (b) of Fig. 3.3 show AFM phase and topography micrographs for the two different coatings and different incubation times on a graphene substrate. Clearly, the PLL coating presents better homogeneity with respect to Collagen Type I coating for which network-like aggregates can be detected. On the other hand, PLL tends to form a homogeneous carpet of spots of 1-2 nm (no aggregates) independent from the incubation time.

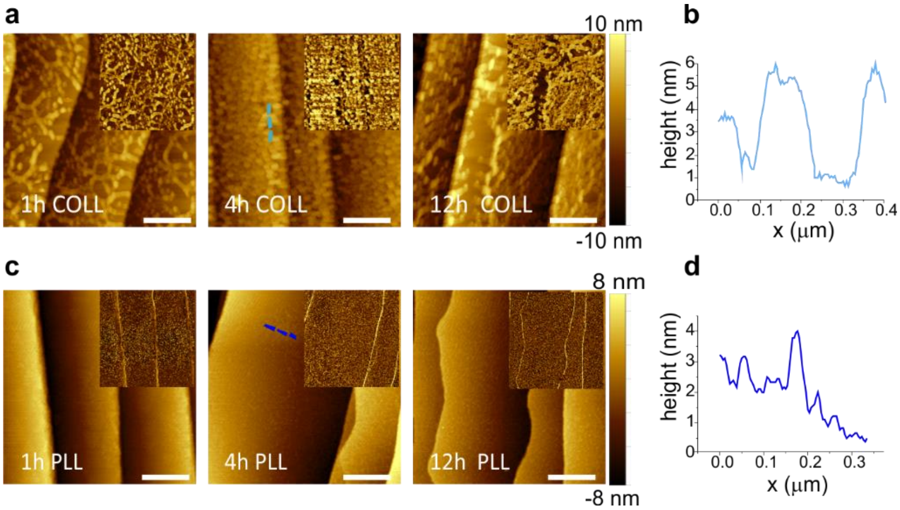

Fig. 3.3. **AFM micrographs of graphene with various polymeric coatings after different incubation times.** AFM topography images of graphene after three different times of incubation (1, 4 and 12 h) with (a) Collagen Type I coating (200 µg/ml in DI water), (c) PLL (100 µg/ml in DI water) (scale bar: 500 nm). The insets show phase images of the same areas. (b,d) AFM height profile, along the dashed lines

with corresponding color in the images, of graphene with each coating after 4 h-incubation. Adapted from [45]

The same characterization was performed for the polymeric coatings typically suggested for DRG neurons, i.e., PBS solution of PDL alone and PDL with laminin. Fig. 3.4 shows the AFM topography and phase images taken for PDL/laminin coated graphene substrates for the three different incubation times (i.e., 1, 4 and 12 h). Also in this case, after the coating, an increased roughness was observed for all time points and in particular the formation of a network-like structure was consistently observed.

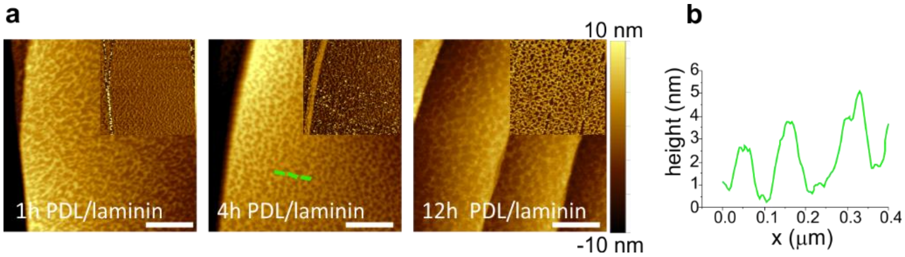

Fig. 3.4. **AFM micrographs of graphene with PDL/laminin coating after different incubation times.** (a) AFM topography images of graphene after three different times of incubation (1, 4 and 12 h) with PDL and laminin coating (30μg/ml PDL and 5μg/ml laminin in PBS) (scale bar: 500 nm). The insets show phase images of the same areas. (b) AFM height profile, along the dashed lines with corresponding color in the image, of graphene with each coating after 4 h-incubation. Adapted from [45]

PDL alone coating gave rise to a similar net (Fig. 3.5(b)). In order to exclude the effect of PBS, we dissolved the same polymeric amount in DI water and after 4h incubation we observed similar structures (Fig. 3.5(a)). This implies that the net morphology is independent from the salts in the PBS solution. To check if the different molecule arrangement of PLL and PDL on graphene was dependent on their concentration (PDL = 30 μg/ml, PLL = 100 μg/ml), we tested also a PDL coating solution in DI water with the same concentration used for PLL (100 µg/ml). Differently from PLL that distributed homogeneously on graphene, PDL at both concentrations tends to form aggregates. The obtained structures were similar to the ones observed for the lower PDL concentration, confirming its independency on solution concentration (Fig. 3.5(c)). It is worth noticing that differently form the PLL water solution that was a ready-to-use product, the PDL was supplied as lyophilized powder subsequently dissolved in DI water. Thus, the presence of the network-like structure on graphene could be ascribed to the interaction of the partially undissolved polymer with the highly hydrophobic graphene surface.

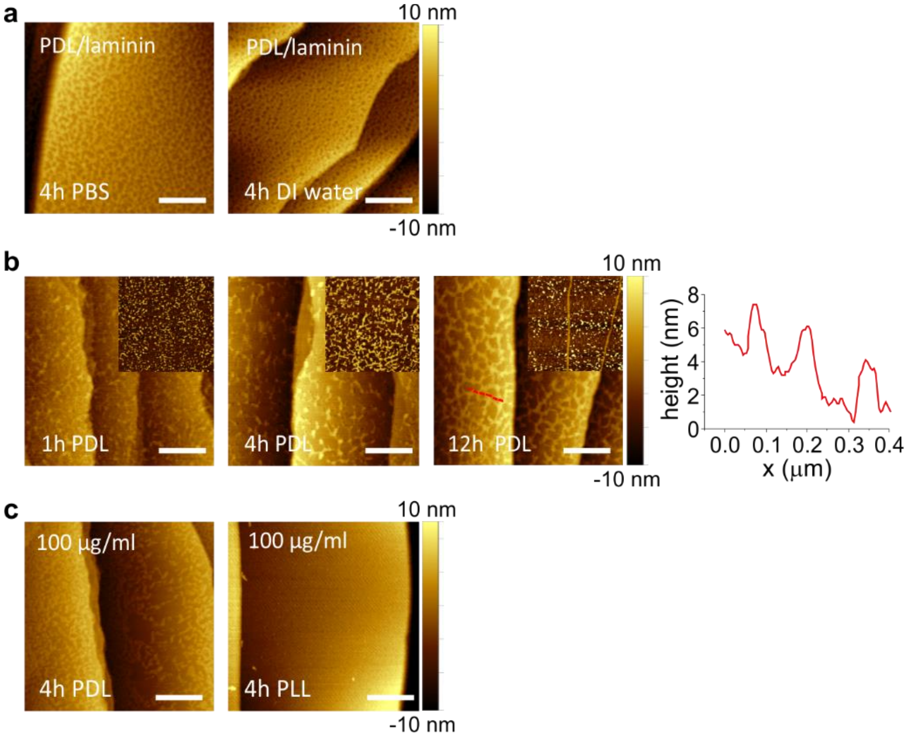

Fig. 3.5. **AFM micrographs of graphene with different PDL coating solutions.** (a) AFM topography of graphene samples coated with PDL/laminin (30 µg/ml PDL and 5 µg/ml laminin), dispersed in DI water and PBS after 4h incubation show similar net structures. (b) AFM topography images with a characteristic line profiles of graphene after three different times of incubation (1, 4 and 12 h) with PDL alone (30 µg/ml). (c) AFM topography of graphene samples coated with PDL and PLL in water at the same concentration (100 µg/ml) after 4h incubation have different arrangements, showing that the

different morphology is not dependent on the concentration but probably on the molecular weight of the two polypeptides (scale bar: 500 nm). Adapted from [45]

We also analyzed the same coatings on control substrates (SiC, gold and glass). On SiC, PLL and Collagen presented analogous topographies homogeneous carpet of spots of few nanometers (Fig. 3.6(a) and (b)). Even in the presence of PDL, on SiC no network formation was observed with or without laminin (Fig. 3.6(c) and (d)). The stability of the coating was confirmed for all the probed incubation times.

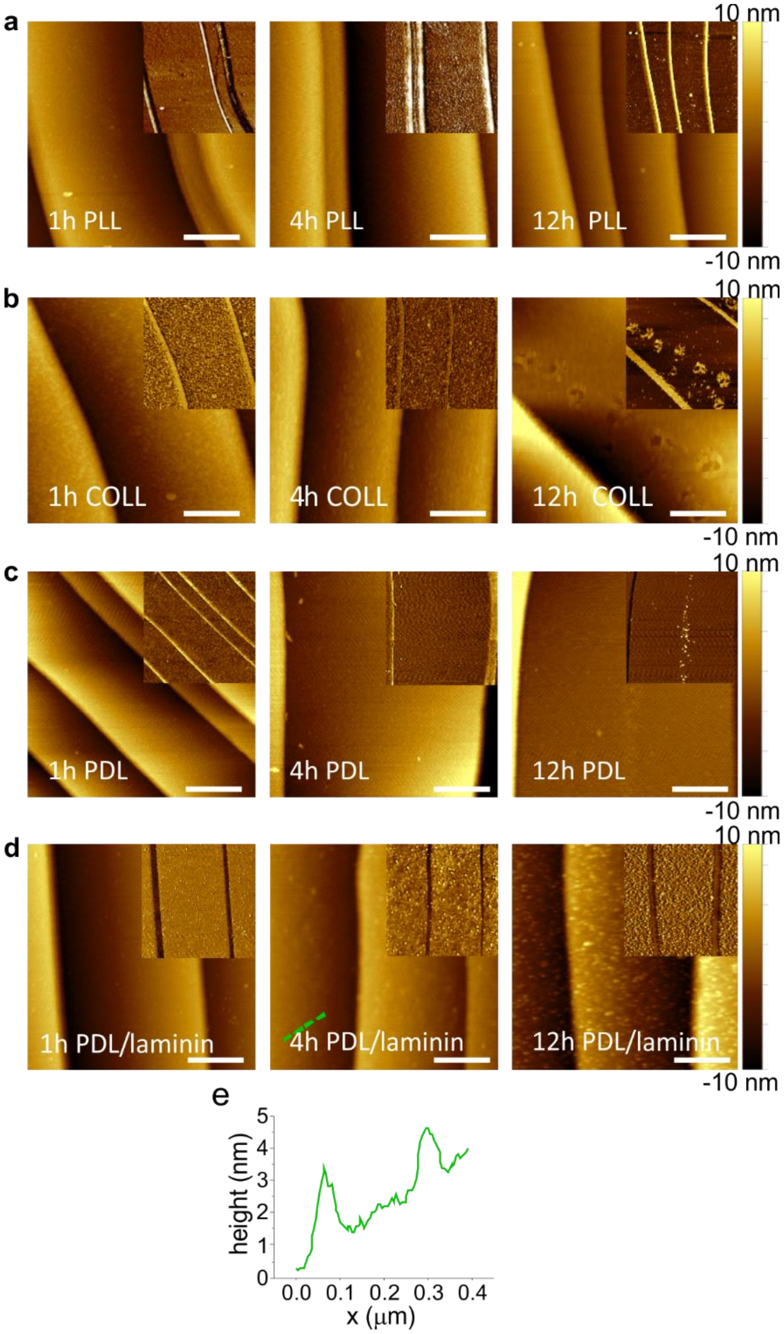

Fig. 3.6 **AFM micrographs of SiC with various polymeric coatings after different incubation times.** AFM topography images of SiC samples after three different times of incubation (1, 4 and 12 h) with a coating solution of: (a) PLL, (b) collagen, (c) PDL, (d) PDL/laminin (scale bar: 500 nm). The insets show phase images of the same areas, which are not sensitive to slow changes in height and improve identification of nanometric structures. (e) All the samples are coated with a homogeneous carpet of

spots of few nanometers, as showed in the AFM line profile of a SiC sample after 4 h incubation with PDL/laminin. Adapted from [45]

Due to the higher surface roughness of gold and glass substrates already before the coating, with RMS roughnesses of about 1 nm comparable to the features of the polymeric layer, no conclusions about the quality of the coating could be drawn (Fig. 3.7(a,b)).

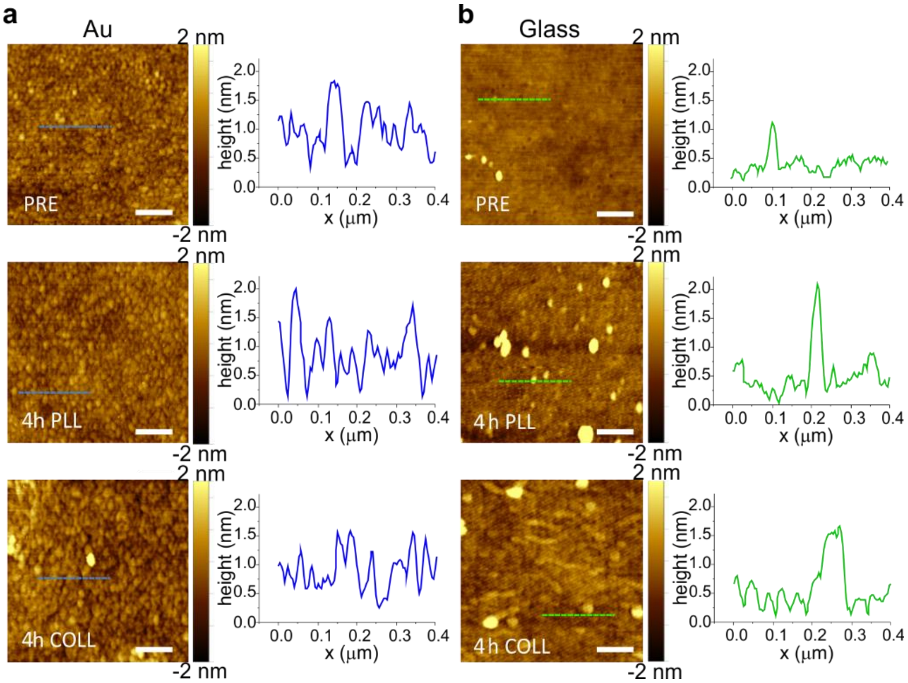

Fig. 3.7. **Gold and glass characterization after polymeric coating.** AFM topography and roughness profiles of gold (a, Au) and nitric-acid-treated glass (b, Glass) before protein coating and after 4h incubation with PLL (4h PLL) and Collagen Type I (4h COLL) (scale bar: 200 nm). Both the surfaces revealed an initial roughness comparable to the one after any coating, preventing the recognition of nanometric details of the coatings. Adapted from [45]

However, presence of the coating was confirmed by the variation in the hydrophilicity observed with contact angle measurements in Fig. 3.8.

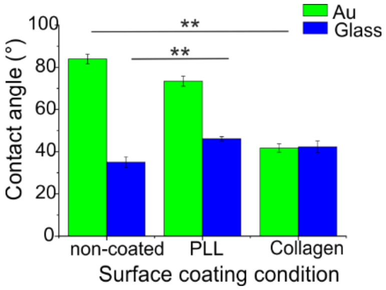

Fig. 3.8. **Contact angle measurements of Au and Glass**. The samples were measured before protein coating and after 4h incubation with PLL and Collagen Type I (Collagen). All measurements were made using DI water as a probe liquid. Values are the mean ± standard deviation for 3 samples. Adapted from [45]

Non-coated gold was more hydrophobic than non-coated glass. The coatings had opposite effects on the substrates, increasing hydrophilicity for gold and increasing hydrophobicity for glass. Contact angles were measured using a CAM 101 contact angle meter, from KSV Instruments Ltd. (Finland) and estimated by measuring the angles between the baseline of the droplet and the tangent at the droplet boundary.

Interestingly, the coating solutions distributed differently on graphene and SiC, despite their similar morphologies before the coating, with nanometric terraces and comparable roughness (Fig. 3.9(a,b)). All polymeric coatings exhibited similar distributions on SiC, while there were significant differences between the coatings on graphene. The dissimilar arrangement of the coatings on the substrates can be reasonably ascribed to the different hydrophilicity of graphene and SiC [151]. As shown by the contact angle measurements reported in Fig. 3.9(c), graphene is in any instance (pre and post-coating) more hydrophobic than SiC.

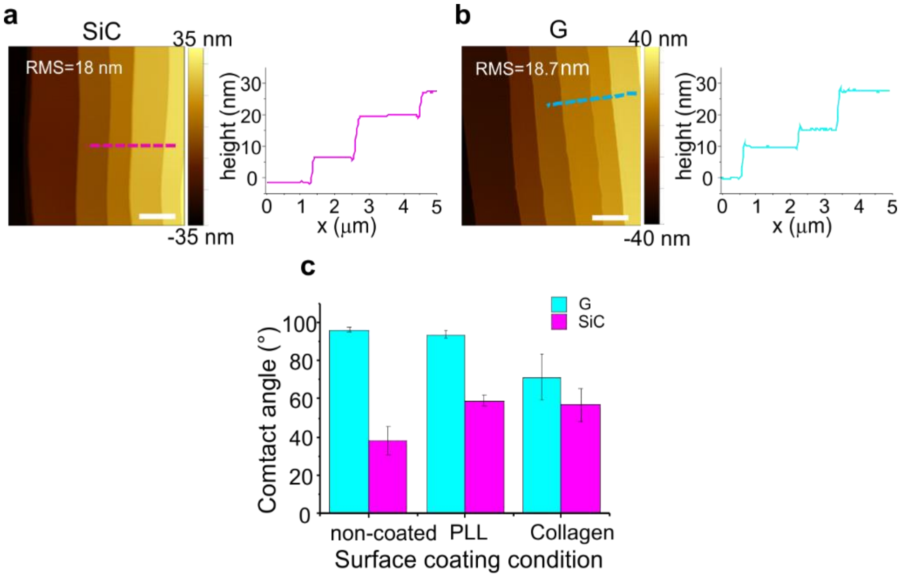

Fig. 3.9. **AFM topography and contact angle measurements of SiC and graphene.** AFM topography of SiC (a) and bare graphene, G (b) samples, with characteristic line profiles across the terraces. Scale bar: 2µm. (c) Contact angle measurements of silicon carbide (SiC) and graphene (G) before protein coating and after 4h incubation with PLL and Collagen Type I (Collagen). All measurements were made using DI water as a probe liquid. Values are the mean ± standard deviation for 3 samples. Non-coated graphene was more hydrophobic than non-coated SiC. Adapted from [45]

The contact angle estimated for graphene was 95.8° ± 1.3° while it was 38.3° ± 7.2° for SiC, in agreement with literature [149,151,152]. SiC hydrophilicity likely facilitated (for all the various coatings adopted) a homogenous adhesion of molecules. The network-like structures often revealed by our analysis on graphene indicate that such pristine hydrophobic surfaces are less prone to be homogenously coated, an important aspect that should be considered in future works when studying cell cultures on graphene.

For the PC12 cells cultured in this work, a PLL coating with an incubation time of 4 h was adopted. While, PDL with laminin coating (with an incubation time of 4 h) was selected to carry on the following DRG culture experiments in order to mimic the extracellular matrix.

3.4 Neurite outgrowth of PC12 cell on graphene

We first investigated the effect of graphene on PC12 cells. Fig. 3.10 reports typical optical micrographs obtained for PC12 cells cultured at day 5 (in the presence and absence of NGF) and at day 7 (with NGF) on the different substrates. The analyses conducted at day 5 evidence that almost no differentiation took place in the absence of NGF, while a significant neurite outgrowth occurred on all substrates upon NGF treatment.

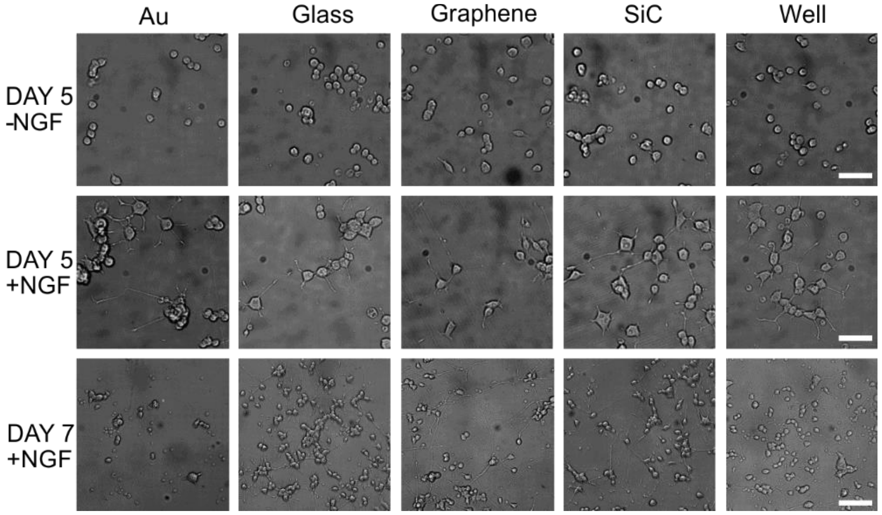

Fig. 3.10. **PC12 cells cultured on graphene and control substrates.** Typical optical microimages of PC12 cells grown on gold (Au), glass coverslip (Glass), graphene (G), SiC and polystyrene (well) coated with PLL (100 µg/ml in DI water), 4 h incubation) in the absence of NGF (first row, scale bar: 50 µm), PC12 cells differentiation at day5 (second row, scale bar: 50 µm) and day 7 (third row, scale bar: 100 µm). Adapted from [45]

Selected morphometric parameters describing the differentiation process were quantified at day 5 and are reported in panels (a), (b) and (c) of Fig. 3.11: the percentage of differentiated cells in the fields (Diff), the average number of neurites per cell (av. neurites/cell) and the length of the longest neurite per differentiated cell (length).

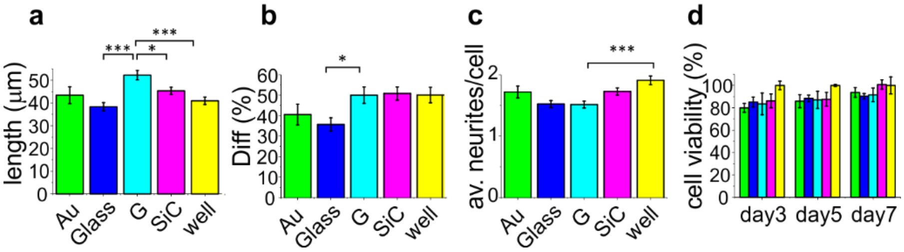

Fig. 3.11. **Morphometric analysis and cell viability of PC12 cells cultured on graphene and control substrates.** Histograms show the quantification of (a) neurite length, (b) percentage of differentiation and (c) average number of neurites per cell after 5 days of NGF treatment of two independent experiments per substrate. For each substrate we analyzed at least 200 cells (nc) from selected fields (nf) (Au: nf=17, nc=203; Glass: nf=33, nc=1106; G: nf=42, nc=877; SiC: nf=35, nc=1004; well: nf=37, nc=724). (d) Cell viability after 3, 5 and 7 days tested by WST-8. The results are reported as % over the polystyrene control sample. Bars colored as in the other graphs. Data reported as mean ± SE. Nonparametric Kruskal–Wallis test was used for statistical significance, with * $p < 0.05$, *** $p < 0.001$. Adapted from [45]

This analysis showed that 50% of the cells on graphene differentiate with a mean neurite length of 52.3 µm (panels (b,c)). Remarkably, the average length was significantly longer on graphene than on glass (***), well (***) and SiC (*) by 27%, 22% and 13%, respectively. The percentage of differentiation on graphene was better than on glass (*), while the average number of neurites per cell was lower on graphene than on the control well (***). These results indicate that PC12 cells grow longer neurites on graphene, with a neuronal differentiation that is comparable to that obtained for the standard control wells. Furthermore, we found that at day 7 living PC12 cells forming neurite networks were present on all the substrates. To better assess graphene cytocompatibility, the viability of undifferentiated PC12 cells was assessed after 3, 5 and 7 days of culture and no statistically significant differences were observed between graphene and the other substrates (Fig. 3.11(d)). Differently from reference [12], we did not observe increased PC12 proliferation on graphene, which could be due to the effect of the FBS coating used in that study.

Our data are in agreement with previous observations that graphene induces neurite sprouting and outgrowth of hippocampal neurons due to an overexpression of GAP-43 protein [11]. Also, Lee *et al.* showed an induced neurite outgrowth of human neuroblastoma SH-SY5Y cells on graphene, probably mediated by FAK and MAPK cascades and upregulation of genes involved in neurogenesis (NFL, nestin and MAP2) [153]. Both the studies excluded a neurogenic effect from substrate topography and wettability. Thus, we speculate that also for PC12 cells, graphene surface chemistry and electrical conductivity can specifically increase neurite length during differentiation.

3.5 DRG primary neurons on epitaxial graphene

Next, we investigated the effect of graphene on primary neurons using DRG cells while using the same controls adopted in the previous culture. As motivated in 3.1, all the samples were coated with PDL/laminin. Fig. 3.12(a) shows typical optical microscopy images obtained at 1, 4, 9 and 15 days of culture. Starting from day 4, we observed numerous processes and an increase in the neurite length (Fig. 3.12(b)) and in the cell body area (Fig. 3.12(c)). Neurons were observed on all the substrates up to 17 days of culture. We observed that both at day 1 and day 2 the average axon length was higher on graphene than on the other substrates (Fig. 3.12(b)). This observation confirms the trend reported for PC12, although in this case no statistical significance was retrieved. Axonal length was not quantified for longer culturing times due to the highly dense network forming after day 2 (see day 9 and 15 in Fig. 3.12(a)).

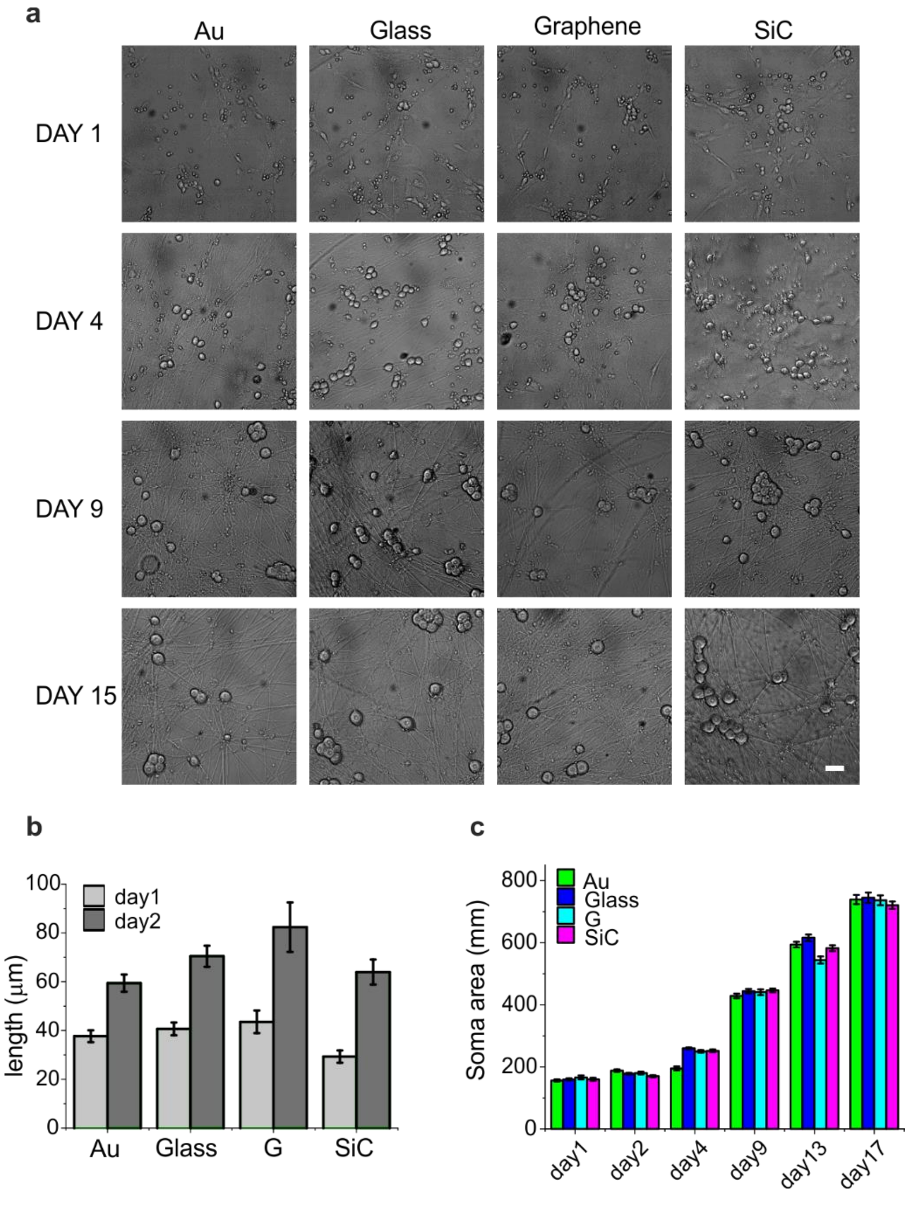

Fig. 3.12. **DRG neurons cultured on graphene and control substrates.** (a) DRG neurons cultured on gold (Au), glass coverslip, graphene (G) and SiC coated with PDL and laminin (30 µg/ml PDL and 5 µg/ml laminin in PBS, 4 h incubation) at different days of culture. Scale bar: 50 µm. Scale bar: 100 µm. (b) Axon length quantification at 24 and 48 hours after cell seeding. (c) Increase of the cell body area with time in DRG cells. For cell soma analyses, cell bodies were approximated to an oval shape and relative areas were evaluated using ImageJ. More than 100 cells per sample were analyzed. We analyzed nf fields for a total of nc cells for each substrate (day1: Au, nf =13, nc=67, Glass: nf =14, nc=75; G: nf =13, nc=29; SiC: nf =12, nc=35; day2: Au, nf=16, nc=89, Glass: nf =13, nc=100, G: nf=12, nc=34, SiC: nf =11, nc=37) and data are reported as mean ± s.e.m. Adapted from [45]

Given that neuronal growth was previously assessed also in cells grown on non-coated graphene [21,22,80,83,86,87,154], we tested also the bare substrates to observe their effect on neurons. Differently from non-coated glass, where they did not survive, DRG neurons could be nicely cultured on non-coated graphene and gold up to 17 days. On coated graphene, neurons distributed homogeneously on the entire samples (Fig. 3.12(a) and Fig. 3.13(a)), while on uncoated graphene neurons formed small interconnected cell islets already after 24h from seeding (Fig. 3.13(a)). Cell body area on bare graphene was comparable with the one on the coated substrate. Higher cell body area on uncoated graphene was observed starting from day 4, but the values did not differ significantly (Fig. 3.13(b)).

After 2-3 days of culture, we observed neurites radially sprouted from the islet, and at longer times neurons formed cell bodies aggregates and neurite bundles (Fig. 3.13(a,c)), probably due to a reduced neural adhesion in the absence of coating, as previously observed for retinal ganglion cells [87] or cortical neurons [83]. The surface modification with the hydrophilic coating turned out to be useful in order to improve adhesion and neuron homogeneous distribution [11,154]. In fact, we rarely observed neurite bundles on coated graphene, while they were present on uncoated graphene already after 2 days of culture and they increased in size with time (Fig. 3.13(d)). Moreover, as previously suggested, the coating could mask the presence of surface inhomogeneity and defects that affect neural adhesion [86].

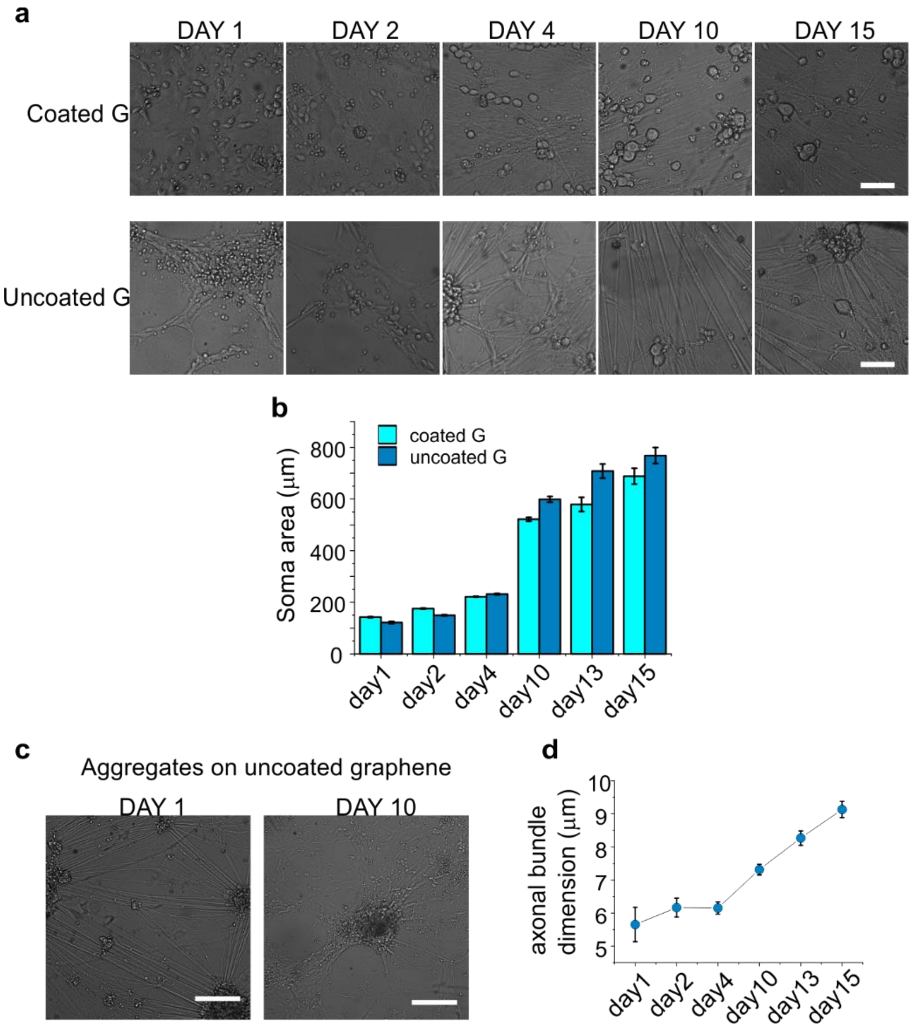

Fig. 3.13. **DRG neurons cultured on bare substrates.** (a) DRG neurons cultured on coated and uncoated graphene at different culture days. Scale bar: 50 µm. (b) Increase of the cell body area with time in DRG cells on coated and uncoated graphene. (c) Cell bodies aggregates and neurite bundles on uncoated graphene at different days of culture. Scale bar: 100 µm. (d) Quantification of axonal bundles dimension on uncoated graphene. The diameter of the axonal bundles was evaluated using ImageJ. Data are reported as mean ± s.e.m.. Adapted from [45]

Concerning material stability issues, it should be noted that graphene showed a good stability and remained intact during the entire culturing period, as revealed by Raman measurements after cell removal (Fig. 3.14). The 2D peak and FWHM are very homogeneous across the whole area and the values resemble those measured before the cell culture, with a narrow 2D peak of ~30 cm^{-1} centered at ~2670 cm^{-1}.

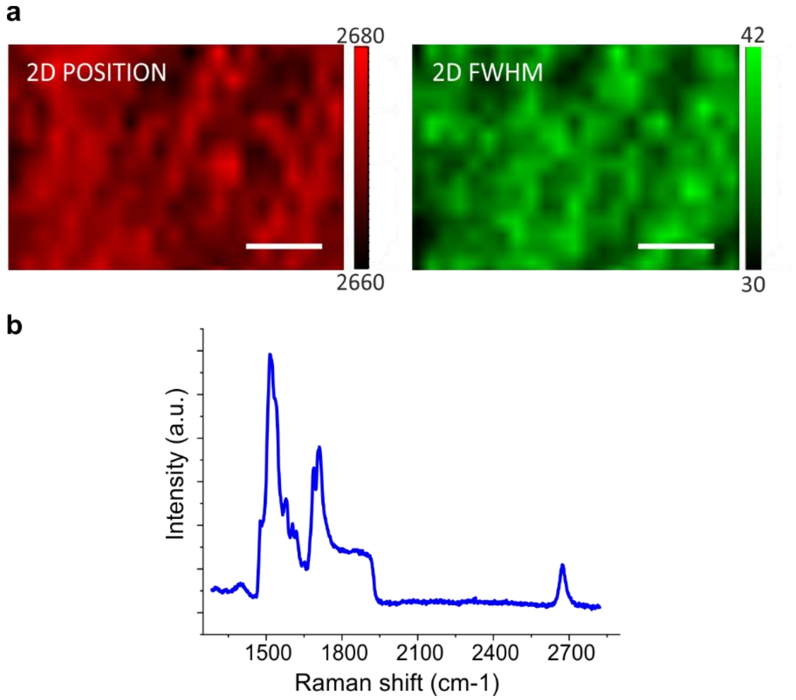

Fig. 3.14. **Raman characterization of graphene sample after cell culture.** Raman was excited with a 532-nm laser. (a) 2D peak position and FWHM distribution in a large area (scale bar: 5 µm). (b) Characteristic Raman spectrum. Raman characterization validates the full coverage of graphene after cell culture. Adapted from [45]

3.6 Conclusion

To summarize, in this first part of the thesis we provided novel data about the use of graphene as a substrate for peripheral neuron cultures. We chose to use graphene on SiC because, thanks to its high quality and cleanliness, it allowed us to examine the graphene effect on peripheral neurons with fewer concerns for contaminations and crystalline quality that may affect neuron adhesion [86].

We use the PC12 cell line as a consolidated model for peripheral sympathetic neurons and show that such cells grow well on graphene with an increased neurite length (up to 27%) at 5 days of differentiation when compared to controls. Remarkably, graphene performs better than gold, which we used as conductive control. Culture of DRG neurons also shows a positive outcome on graphene: neurons survive both on bare and coated graphene until day 17, with a dense axon network that is comparable to the control substrates. In order to investigate graphene influence on axonal outgrowth, further studies using compartmentalized chambers [155] are reported in the next chapter. The obtained results confirm the potential of graphene as an active substrate in conduit devices for nerve guidance: it would allow the transmission of electrical signals between neurons and make external electrical stimulation feasible to enhance axon regeneration. While for many biomedical applications graphene-based materials with higher roughness might be desirable, in specific cases when high transparency and electrical conductivity are required, pristine highly crystalline graphene might be the ideal choice [28,156]. It should be noted that flexibility is a requirement in neural regeneration that cannot be met by using graphene on SiC. To use graphene as neural interface other graphene production methods, such as CVD, could be more suitable.

4 Graphene promotes axon elongation through local stall of Nerve Growth Factor signaling endosomes

In this chapter, our investigation of the molecular details underneath the effect of graphene on DRG primary neuron cultures during the early developmental phase is discussed. Indeed, despite several works reporting an increased differentiation of neuronal cells grown on graphene, the nanoscale events driving axon elongation on this material remained elusive. We studied the axonal transport of NGF, the neurotrophin supporting development of peripheral neurons, as a key player of the time course of axonal elongation of DRG neurons on graphene.

We found a statistically significant higher neuron outgrowth on graphene during the first 3 days of culture, with an axonal sprouting up to 79% greater than in the control. To shine light on this result, the role of NGF neurotrophin, a key molecule involved in neurite elongation and survival during DRG development [46,47] was investigated by single-molecule fluorescence microscopy. Remarkably, we found that axonal sprouting on graphene correlates with a significant reduction of NGF vesicles retrogradely transported to the soma, in favor of a stalled pool retained locally in the developing axons. This correlates with a mutual charge redistribution observed both for the material via Raman spectroscopy and the cell membrane via electrophysiological recording. Furthermore, ultrastructural analysis indicates a reduced inter-microtubule distance and a stretched axonal topology. Combined electrophysiology and ultrastructural analyses show that profound rearrangements occur in the axon developing on graphene, which might be causally involved in the local accumulation of NGF and therefore in the increased axon elongation.

This chapter presents experimental data contained in a manuscript in preparation with authors D. Convertino, F. Fabbri, N. Mishra, M. Mainardi, V. Cappello, G. Testa, S. Capsoni, L. Albertazzi, S. Luin, L. Marchetti, C. Coletti: ”Graphene promotes axon elongation through local stall of Nerve Growth Factor signalling endosomes”.

Moreover, the data comparing labeling and axonal transport performance of Abberior488 and Alexa488 in fluoNGF are contained in a manuscript in preparation with author R. Amodeo, D. Convertino, F. Bonsignore, C. Ravelli, M. Calvello, S. Luin, S. Mitola, A. Cattaneo, Signore G., L. Marchetti: “Comparative study of different membrane receptors and fluorophores in the performance of YBBR-related chemical tag labelling reactions”.

CVD graphene transfer and characterization, DRG harvesting and dissociation, cell culture and immunofluorescence staining, fluoNGF production and characterization, transport measurements, STORM imaging and all the data analysis (except for the data concerning Raman characterization of the neuron/graphene system and patch clamp recordings) were performed by D. Convertino.

4.1 Nerve growth factor

Discovered in 1950 by Rita Levi-Montalcini, NGF is a neurotrophic factor known to promote growth and survival of peripheral sensory and sympathetic nerve cells of mammalians [157,158]. NGF belongs to a family of neurotrophic factors named neurotrophins; this family includes brain-derived neurotrophic factor (BDNF), neurotrophin 3 (NT-3), and neurotrophin 4/5 (NT-4/5) [159].

Subsequent studies have shown that NGF is produced and released by sympathetic and sensory target tissues and binds the membrane TrkA receptors at the axonal tip triggering the internalization of the NGF-TrkA complex into signaling endosomes. After internalization it is retrogradely transported to cell bodies, where it prompts gene expression and activation of different signaling pathways [160]. Sympathetic and sensory ganglia in tissue culture have been demonstrated to produce a dense halo of axons when treated with NGF. Furthermore, by using NGF deprivation experiments, NGF has been shown to be required for the survival of dissociated sympathetic and some sensory neurons grown in the absence of non-neuronal cells [161]. The neurotrophic hypothesis provides an explanation of the phenomenon: developing neurons compete for target-derived neurotrophic factors and only successful competitors survive.

The biological action of NGF is mediated by two NGF-receptors, the high-affinity receptor TrkA, having a tyrosine kinase activity, and the low-affinity transmembrane glycoprotein, a non-selective pan-neurotrophin receptor p75NTR that regulates signaling through TrkA. Following NGF binding, TrkA tyrosine residues are phosphorylated and become docking sites for signaling molecules that activate the MAPK pathway, the phosphoinositol-3-kinase (PI3K) pathway, and the phospholipase C-gamma (PLCγ) pathway, known for regulating neural survival, growth and differentiation [162]. Receptor p75NTR binds to NGF as well and increases TrkA responsiveness to NGF [162].

4.1.1 Axonal transport and signaling endosome model

The classic neurotrophic factor hypothesis showing the neurotrophin retrograde signaling via long-distance transport of signaling endosomes is reported in the schematic Fig. 4.1.

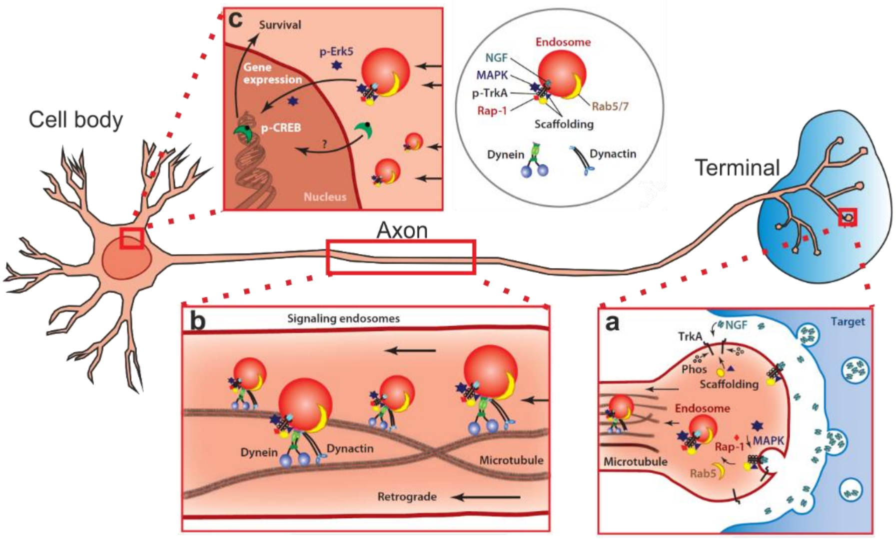

Fig. 4.1. **Neurotrophin retrograde signaling via long-distance transport of signaling endosomes**. (a) Endosome formation at the axonal terminal following NGF binding to the TrkA receptor. (b) Retrograde transport driven by dynein along the microtubule. (c) Signaling cascade at the cell body. Adapted from [163].

The signaling endosomes are retrogradely transported by dynein along the microtubule to the cell body, where they induce various signaling cascades that regulate gene expression by activating nuclear transcription factors such as cAMP response element-binding protein (CREB) [159,163], thus ensuring neuron survival.

While retrograde endosome transport was accepted to be the main mechanism sustaining the survival of neurons, Campenot proposed an alternative model that also takes into account the local effect of NGF following the phosphorylation cascade caused by the receptor binding [164]. He supposed that only a part of binding NGF is transported to the cell body, controlling neuronal survival, gene expression and protein synthesis. The remaining part could exert biological effect, such as neurite growth, which are localized to the site of extracellular application [165].

NGF binding, internalization and axonal transport have been studied through different approaches. It was observed for the first time in 1974 by using iodine-125-labeled NGF (^{125}I-NGF). The ^{125}I-NGF injected into the anterior eye-chamber accumulated in the superior cervical ganglion of the injected side, supporting the existence of NGF retrograde transport along the axons to the cell bodies [166]. Another common technique uses quantum dot-labeled NGF (QD-NGF), which was demonstrated to retain its biological function and guarantees an excellent brightness and photostability for single molecule tracking [167]. An alternative fluorolabeling strategy, employed for the first time by our group, uses a site-specific enzymatic covalent binding to obtain a 1:1 (organic dye : neurotrophin monomer) stoichiometry [168,169]. In this work, we chose to use the latter technique thanks to its main advantages: due to its very small dimension the tag does not interfere with protein folding and stoichiometry in complexes or vesicles, and the labeling strategy guarantees a 1:1 fluorophore:neurotrophin monomer stoichiometry.

The labeling is based on a method firstly described by Yin *et al.* [170] and reported in De Nadai *et al.* [168] and Di Matteo *et al.* [169] (Fig. 4.2). We used a modified neurotrophin obtained by fusing an 11 residue peptide named ybbR with the C-terminus of the NGF sequence [169] .The NGF-ybbR was adopted for site-specific protein labeling by Sfp synthase enzyme. The enzyme catalyzes a reaction that covalently links the 4′-phosphopantetheinyl group of the coenzyme A (CoA) to a serine residue in the ybbR sequence. We utilized fluorescent derivatives of CoA (CoA-Alexa488 and CoA-Abberior488) to produce fluorescent NGF (fluoNGF).

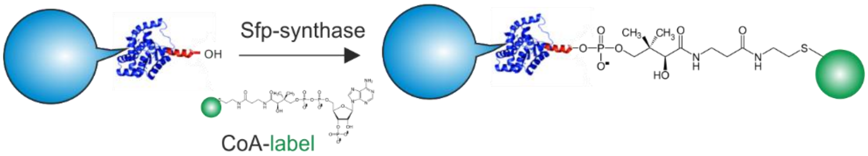

Fig. 4.2. **Site-specific protein labeling by Sfp synthase.**

The fluorescent neurotrophin was then purified via high-performance liquid chromatography (HPLC). This is a chromatographic technique used for resolving mixtures of molecules. The analyte is dissolved in a buffer (mobile phase) and pumped at high pressure through a column, which contains specific packing material (stationary phase) needed to carry out separation. Separation of the component in our case is based on molecule charge. Molecules (in our case, proteins) charged oppositely to the ligands on the stationary phase interact with them and are temporarily retained in the column. They are then eluted from the column by increasing the ionic strength of the buffer. The buffer is gradually substituted with a buffer containing salt (from 0% to 100% of a buffer containing 1M NaCl). When salt is added, the ions establishes a competition with the protein for the charged groups on the stationary phase, leading to the elution of the protein from the column that is detected by measuring the absorbance at 280 nm.

4.2 Materials and methods

4.2.1 CVD graphene synthesis, transfer and characterization

CVD graphene samples were synthesized and transferred on 10 mm round glass coverslip for standard cell culture and on rectangular coverslip 22 x 50 mm for culturing using microfluidic chip for compartmentalized cell culture as reported in detail in sections 2.4.1 and 2.4.2, respectively.

The samples were characterized by Raman spectroscopy, confirming the single layer nature of the graphene samples, with prominent G and 2D peaks, narrow 2D peak (FWHM = 29-34 cm^{-1}) and absence of the D-peak [171,172]. Carrier concentration measurements were performed at RT using an Ecopia HMS-3000 Hall System operating in van der Pauw configuration, with the four golden probes placed in the corner of 5 x 5 mm substrates.

4.2.2 Surface functionalization

Graphene and control samples were coated using PDL with laminin coating solution (30µg/ml PDL and 5µg/ml laminin in PBS). An incubation time of 4 h was used for coating the 10 mm round glass coverslip [45]. When the microfluidic chambers were used, an overnight incubation was chosen as suggested by the company.

4.2.3 DRG neurons cell culture

4.2.3.1 Harvesting and dissociation of dorsal root ganglia

All animal procedures were approved by the Italian Ministry of Health (notification n°917) and were fully compliant with Italian (Ministry of Health guidelines, Legislative Decree n°26/2014) and European Union (Directive n°2010/63/UE) laws on animal research. The experiments were carried out in strict accordance with the approved guidelines. In addition, the principles of the Basel Declaration, including the “3R” concept, have been considered throughout the whole project.

The primary sensory neurons used in this study were obtained from the dorsal root ganglia of wild-type B6129 P3-P4 neonatal mice.

We performed the dissection under a dissection hood equipped with a stereo microscope (Fig. 4.3a), using bone scissors, fine straight scissors, small spring scissors and thick and fine forceps (Fig. 4.3b). Briefly, the mice were killed via cervical dislocation and pinned with the dorsal side facing up (Fig. 4.3c) and the dorsal side of the spinal cord was incised and lifted until reaching the caudal part (Fig. 4.3d). The spinal marrow was removed to locate the DRGs (Fig. 4.3e). The DRGs were carefully removed and collected in a petri filled with a solution of PBS with 50 units/ml of Pen-Strep on ice (Fig. 4.3f). 20-30 DRGs were collected per animal from all spinal levels.

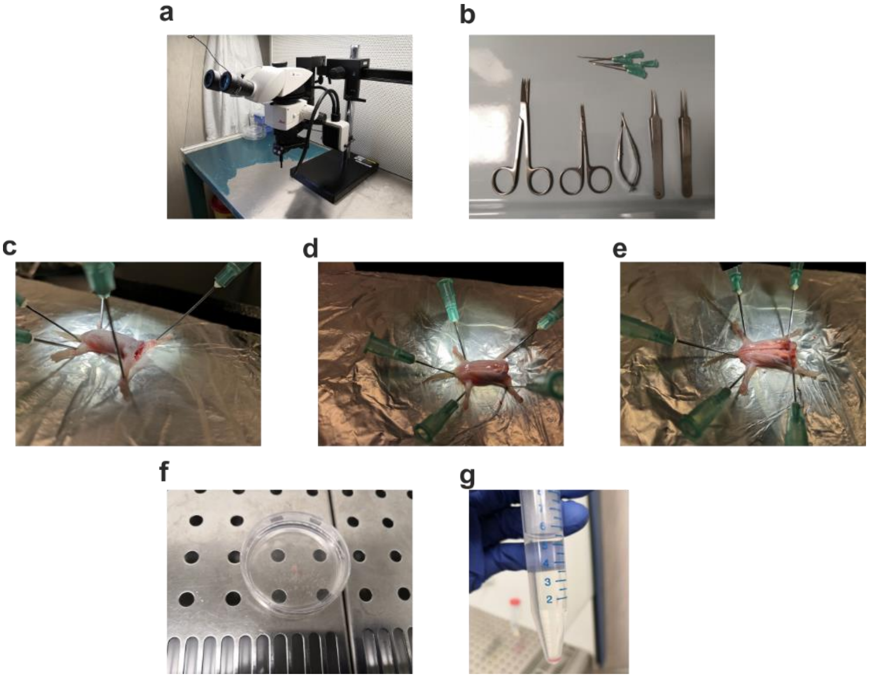

Fig. 4.3. **Mouse dissection.** (a) Stereo microscope. (b) Dissection tools. (c) Mouse pinned to the dissecting board. (d) Removal of back skin. (e) Removal of spinal marrow. (f) DRGs from 5 mice collected in a petri dish. (g) Cell pellet.

The DRGs were enzymatically digested by incubating them for 40 min at 37 °C in a PBS solution containing 0.03 % Collagenase from Clostridium histolyticum (C7657 Sigma), 0.3% Dispase II protease (D4693 Sigma) and

0.18% glucose. After digestion, ganglia were transferred to a 50 mL conical centrifuge tube with 5 mL of PBS containing 0.01% Deoxyribonuclease I from bovine pancreas (D5025 Sigma) and 0.05% Trypsin inhibitor from Glycine max (T9003 Sigma). Ganglia were dissociated by mechanical agitation through a fire-polished glass Pasteur pipette until the suspension was homogeneous. The solution was then centrifuged for 10 min at 1000 rpm and the cell pellet (Fig. 4.3(g)) resuspended in Primary Neuron Basal medium (PNBM, Lonza) supplemented with 1% L-glutamine (Lonza), 0.1% Gentamicin Sulfate/Amphotericin-B (Lonza), 2% NSF-1 (Lonza). For the survival of DRG neurons, 100 ng/ml of NGF (Alomone Labs) was added to the media. Since 24 h after seeding, 2.5µM AraC (Sigma-Aldrich) was added for inhibition of glia proliferation. Half of the medium was replaced every 3–4 days.

4.2.4 Microfluidic cell culture platform

In this thesis, Polydimethylsiloxane (PDMS) compartmentalized microfluidic chambers (RD150 or RD450, Xona Microfluidic), previously described by Taylor in 2005 [155] have been employed to study axonal elongation and NGF axonal transport in living DRG neurons.

The device is made by two compartments, the soma side and the axonal side. Both the compartments have two inlets connected by a main channel for cell seeding and medium replacement. The main channels are connected by 10 µm wide, 3 µm high and 150 or 450 µm long microgrooves (Fig. 4.4(a,b)).

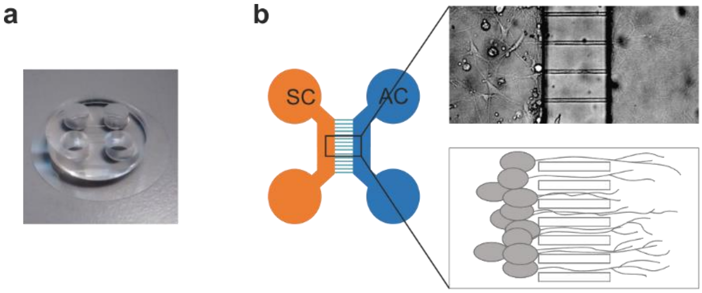

Fig. 4.4. **Microfluidic cell culture platform.** (a) PDMS device on a glass coverslip. (b) Schematic of the device showing the two compartments: the soma compartment (SC) and the axon compartment (AC). Neurons are plated into the SC and extend their axons to the AC through the microgrooves.

Neurons are plated into the soma compartment and extend their axons to the axonal compartment through the microgrooves thanks to a NGF gradient (50 ng/ml of NGF in the soma compartment and 100 ng/ml in the axon compartment) [168]. The microgrooves are small enough to act as a barrier that allows the passage of neuritic processes into the axonal side but not of cell bodies (Fig. 4.4(b)). A volume difference between the two compartments (~50 μl, higher volume on the soma side) allows their fluidic isolation owing to the high resistance of the microgrooves [155]. The microgrooves not only isolate axons but also physically guide axons to grow in straight lines, allowing easy experimental manipulation and analysis.

We combined this technology with graphene, simply transferring graphene on the glass coverslip before the device assembling (Fig. 4.5).

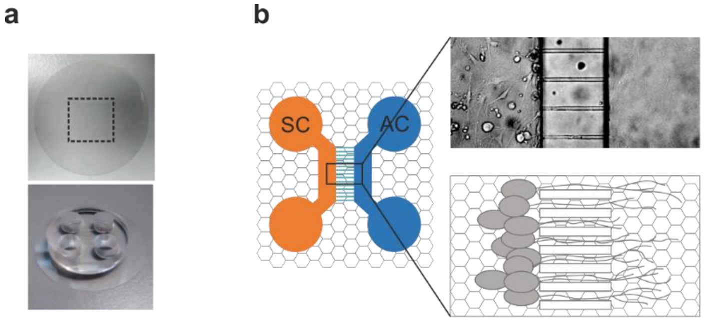

Fig. 4.5. **Schematic representation of compartmentalized microfluidic cell culture on graphene.** (a) Optical image of CVD grown graphene transferred on glass before (top, black dashed square) and after (bottom) assembling the device. (b) Neurons are seeded in the SC and extend their axon in the microchannels reaching the AC always in contact with graphene.

In the standard protocol, the device is covalently sealed to glass using plasma bonding. Since plasma is commonly use to etch graphene, we performed a non-plasma bonding realizing a watertight seal by conformal contact [155].

Prior to assembly of the glass substrates with the chamber, both the coverslips and the devices were immersed in 96% ethanol for 30 min, rinsed several times with DI water and dried under a tissue culture hood to guarantee sterility. The device was then assembled by simply placing it on top of coverslip and pressing down with the back of a pair of tweezers. It was washed with ethanol and DI water. Due to the high hydrophobicity of the device and glass, a micropipette was used to push the water into the main channels and remove any possible bubbles. Next, the coating solution (150-200 µl, 30 µg/ml PDL and 2 µg/ml laminin in PBS) was added to each compartment and incubated overnight at 37 °C. The sample was cleaned repeatedly with DI water and incubated with DI water for 1 hour. It was then washed for the last time with the cell culture medium and left in the incubator for at least 10 min before cell seeding.

4.2.5 DRG neurons seeding

Neurons were seeded using two different approaches specifically designed to gain quantitative information on axonal length on graphene. The standard approach used neurons seeded on a graphene transferred on a glass coverslip, while the compartmentalized approach employed a microfluidic chamber placed on top of a graphene-coated glass coverslip.

Neurons plated on glass coverslips were used as controls in both cases. Glass coverslips were previously treated overnight with 65% nitric acid (Sigma-Aldrich), washed several time with DI water and left in 96% ethanol.

In the standard approach, cells were seeded on round, 10mm diameter coverslips placed in a 24 well plate. Neurons were placed as a drop of 80 µl on each coverslip and incubated at 37°C to allow cell attachment. After 1 h, 500 µl of culture medium were added. Neurons were maintained in a humidified atmosphere at 37°C, 5% CO_2 in Primary Neuron Basal medium (PNBM, Lonza) supplemented with 1% L-glutamine (Lonza), 0.1% Gentamicin Sulfate/Amphotericin-B (Lonza), 2% NSF-1 (Lonza), 2.5 µM AraC (Sigma Aldrich) and 100 ng/ml NGF (Alomone Labs).

When a more homogeneous cell distribution was preferred (e.g. low cell density for axonal elongation measurements), neurons were suspended in a larger volume of culture medium and 500 µl of culture medium were added to each well.

For compartmented culture, 10 µl of dissected neurons were loaded in the soma compartment at a concentration of 2.5 to 4.5 million cells per ml. The device was incubated for 1 h to allow the cells to attach and then each well was filled with the media. Moreover, after 24h from seeding the NGF gradient was applied. The medium was renewed every 1-2 days, with a pre-warmed fresh one, maintaining the NGF gradient to prevent the salt concentrations increasing due to medium evaporation. When devices with microchannels of 150 µm are used, usually the axons reach the axon compartment after 2 days.

4.2.6 DRG axonal length quantification

For axonal length quantification using the compartmentalized approach, neurons were seeded in devices with microchannels of 450 µm and maintained with an NGF gradient for 4 days. Axon lengths were measured daily in the microgrooves compartment and in the axon compartment using an inverted Leica AF6000 microscope with an oil immersion 63x objective at 37 °C, 5% CO_2. The length quantification was performed excluding the axonal segments in the soma compartment due to impossibility to distinguish single axons in the network complexity.

For axon length quantification of neurons on graphene coated glass coverslip, neurons were seeded at a very low density to distinguish single axons. The length was quantified by manually tracing the axon from the soma to the axonal growth cone. We performed two independent cultures with three and four biological replicate each. We analyzed at least 40 cells from more than 10 selected fields obtained with an inverted microscope equipped with a 20× objective (Leica DMI4000B microscope).

4.2.7 Immunofluorescence staining

Neurons were fixed at various days in vitro using 2% (w/v) Paraformaldehyde (PFA), 4% (w/v) sucrose in PBS for 20 min at RT and rinsed 3 times with PBS. Fixed neurons were then permeabilized in 0.1% (v/v) Triton-X-100 in bovine serum albumin (BSA) 2% (w/v) in PBS for 7 min. After 5 washing in PBS the samples were blocked in blocking buffer (BSA 5% in PBS) for 1 h and subsequently stained with mouse anti-NfH antibody (1:500, neurofilament heavy chain, Abcam ab7795) in incubation solution (BSA 2.5% in PBS) for 2 h. After PBS washing, the samples were stained for 1 h at RT with secondary antibodies anti-mouse-Alexa488 (1:100, Invitrogen, A21202) diluted in incubation solution. Coverslip were mounted on glass slide in Fluoroshield with DAPI mounting media (Sigma-Aldrich).

Alternatively, neurons were stained with primary mouse anti-beta III Tubulin antibody (1:200, Abcam, ab78078), with secondary antibodies anti-mouse-Alexa488 (1:100) diluted in incubation solution for 1 h and then with Alexa-647 conjugated phalloidin (500 nM in PBS, Invitrogen A22287) overnight at 4 °C. Coverslip were mounted on glass slide in Vectashield mounting medium (Vector Laboratories).

4.2.8 Fluorescence microscopy

Neurons stained with Alexa488-anti-NfH were imaged using a confocal microscope (Leica TCS SP5 SMD on an inverted DM6000 microscope) using a 20x or 40x oil-immersion objectives. Images were acquired illuminating the sample with a 488-nm laser for Alexa488 and a diode 405 laser line (Picoquant, Berlin, Germany) for 4′,6-diamidino-2-phenylindole (DAPI).

Neurons stained with Alexa488-anti-beta III Tubulin and Alexa647-conjugated phalloidin were imaged using an inverted epi-fluorescence microscope (Leica AF6000) equipped with Leica TIRF-AM module, electron multiplying charge-coupled-device camera (ImagEM C9100-13, Hamamatsu), and 100× oil immersion objective (NA 1.47), allowing the acquisition of fields of 512 × 512 pixels (117.03×117.03 µm) typically comprising several cells. Alexa647 was imaged using the 635 nm laser line with a 110 nm penetration depth for excitation and a Cy5 Leica1152303 emission filter. Alexa488 was imaged using the 488 nm laser line with 90 nm penetration depth for excitation, a 482-510 excitation filter and a BP 525/20 Leica emission filter. Laser power, gain and EM gain values were kept constant within different groups to allow quantitative comparisons

4.2.9 NGF fluorolabeling

For the fluorolabeling reaction 45 µg of NGF-ybbR were diluted in PBS and spun at 7000 rpm for 1 min at 4 °C. The following reagents were then added: 73 µM CoA-Alexa488/Abberior488, 17µM Sfp Synthase, 36 mM $MgCl_2$ in PBS up to 135 µl final volume. The reaction was performed in the same tube were the NGF was stored. The solution was incubated at 37 °C and 350 rpm for 30 min. When the reaction was completed the solution was purified via HPLC to separate the fluorescent neurotrophin from the population that has not reacted.

We performed a cation exchange HPLC, using a Propac SCX-20 column (Dionex, Thermo Fisher Scientific) with 100 mM HNa_2PO_4 mobile phase with 0 M to 1 M NaCl gradient. The temperature was kept at 4 °C. The elution time of the reacted neurotrophin was shifted due to the negative charge of the fluorophore. FluoNGF was separated from the non-reacted neurotrophins and from the free fluorophore by measuring the absorbance at 280 nm and 488 nm.

Prior to use, fluoNGF was quantified via spectrophotometer. The fluorescent signal was measured and compared with a calibration curve obtained by repeated dilutions of CoA-Alexa488 or CoA-Abberior488 of known concentration. The fluoNGF was stored at 4 °C for at most 15-20 days.

The presence of the protein was then confirmed by Sodium Dodecyl Sulphate - PolyAcrylamide Gel Electrophoresis (SDS-PAGE) analysis[1].

The fluoNGF solution was mixed with Laemmli buffer without bromophenol blue and heated at 95 °C for 5 min. It was then loaded in a Tris-Glycine eXtended precast gel (Criterion TGX 4-20%, Biorad) in the Tris/glycine/SDS running buffer. The gel was run at 80 V for 10 min, then the voltage was increased up to 100 V until the end of the run. Finally, the fluoNGF gel was scanned using an ImageQuant LAS 4000 imager (GE Healthcare Life Sciences) to visualize the bands that identify the NGF marked with Alexa488 or Abberior488.

4.2.10 Transport measurements

To image transport of fluoNGF in live DRG neurons, the compartmentalized culture was supplied with 2nM fluoNGF in the axon side and incubated for 1 h (Fig. 4.6(a)). The device was then mounted on a homemade microscope stage kept at 37 °C and 5% CO_2 during measurements. Time-lapse images were acquired in the channel compartment using an inverted epi-fluorescence microscope (Leica AF6000) equipped with Leica TIRF-AM module, a 100x oil immersion 1.47 NA objective and a Hamamatsu camera (ImagEM C9100-13, Hamamatsu).

NGF conjugated with Alexa 488 (or Abberior488) was excited by epi-fluorescence microscopy using a 488 nm laser, with an exposure time of 100 ms. Up to 1000 frames for each experiment have been acquired. Live cell

---

[1] SDS-PAGE is a type of polyacrylamide gel electrophoresis that separates molecules based on their molecular weight. It uses sodium dodecyl sulfate (SDS) to denature the proteins and negatively charge them in a uniform way. Upon the application of a constant electric field, the proteins start to run in the gel with a speed that depends on their molecular weight.

fluorescence imaging was effectuated in the channel compartment, after 30 min from the neurotrophin administration for a total time course of about 45 min.

The typical acquired time-lapse video on glass is shown in Fig. 4.6(b). The colored circles and lines represent the vesicles and the relative trajectory during a time window of 300 frames (corresponding to 30 seconds).

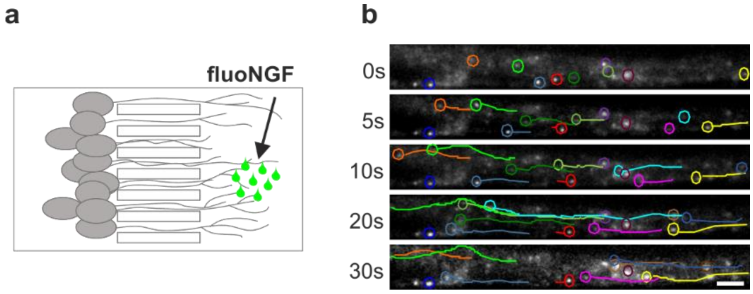

Fig. 4.6. **Live axonal transport of fluo-NGF.** (a) Schematic representation of compartmentalized microfluidic cell culture. Neurons are seeded in the soma compartment and extend their axon in the microchannel reaching the axon compartment, where fluoNGF is administered (green droplets). (b) Representative images of the time lapse videos of NGF vesicles of DRG axons on glass. Colored circles underline vesicles at the end of a time-movie; the line in the same color-code highlights the trajectory run by that vesicle during the time-movie. Scale bar: 5 µm.

4.2.10.1 Single particle tracking analysis

Tracking of single vesicles containing NGF was performed with homemade script in MatLab (The MathWorks) implemented by Prof. Stefano Luin (Scuola Normale Superiore, Pisa) starting as described in De Nadai *et al.* [168].

Briefly, we selected manually the channels (usually 2) present in each field of view, and used functions distributed by Raghuveer Parthasarathy [173] for sub-pixel localization (by radial symmetry fitting) and tracking (https://pages.uoregon.edu/raghu/particle_tracking.html). Trajectories longer than 5 frames were considered and divided in subtrajectories on the basis of the vesicle velocity calculated using a mobile window of 5 frames, considering retrograde (positive) movement for velocities higher than 0.5 µm/s and anterograde (negative) transport for velocities lower than -0.5 µm/s. We calculated the velocity distribution of this mobile subtrajectories, weighting the velocity of each subtrajectory with its time length and considering its s.e.m. as in [168].

Differently from [168] we maintained all the trajectories, even the ones with a total shift less than 10 µm, and classified the whole trajectories in 4 populations based on the way they moved along the channel: (i) stall, (ii) anterograde, (iii) retrograde and (iv) oscillating. For this classification, trajectories shorter than 30 frames were discarded. Vesicles were classified as "stalled" when: a1) being composed by less than 10% of moving subtrajectories; a2) displaying a total average anterograde or retrograde speed less than 0.03 µm/sec; or b) displaying a total displacement less than 1.14 µm. Vesicles showing an oscillatory transport with a succession of anterograde and retrograde motions and average total speed less than 0.1 µm/sec, or with total shift less than 2.28 µm, were classified as "oscillating". The other trajectories were considered "retrograde" or "anterograde" depending on the direction of the total shift, respectively from the axons to the soma or vice versa.

4.2.11 Patch clamp recordings on DRG cultures

In this work, recordings were performed on DRG primary neuronal cultures by Dr. Marco Mainardi (BIO@SNS Laboratory, Scuola Normale Superiore, Pisa), by adapting the procedure described in Siano *et al.* [174]. Cells were continuously bathed using Tyrode's solution containing (in mM): NaCl 150, KCl 4, $MgCl_2$ 1, $CaCl_2$ 4, Glucose 10, HEPES 10, pH 7.4 with NaOH. Borosilicate glass pipettes were pulled with a P-97 puller (Sutter, CA) to a resistance of 5-6 MΩ when filled with an internal solution containing (in mM): K-Gluconate 145, $MgCl_2$ 2, HEPES 10, EGTA 0.1, Mg-ATP 2.5, Na-GTP 0.25, phosphocreatine 5, pH 7.35 with KOH. After achieving a gigaohms resistance seal (gigaseal) and, then, whole-cell configuration, at least 3 min were allowed for complete equilibration between cytosol and internal solution. After switching to I=0 configuration, the resting membrane potential was measured for at least 2 min. Subsequently, in current clamp configuration, current injection was adjusted to obtain an initial membrane potential of -60 mV before delivering 20 pA current steps. Access resistance and membrane capacitance were monitored, and recordings were accepted only if series resistance had varied less than 20% of the initial value. Data were acquired using a MultiClamp 700A amplifier, connected to a Digidata 1322A digitizer (Molecular Devices, CA). Data were analyzed using Clampfit 10.7 (Molecular Devices).

4.2.12 Stochastic optical reconstruction microscopy

STORM is a super resolution technique based on the localization of photoswitchable fluorophores [175]. The high resolution is achieved through the accurate localization of a small fraction of activated fluorophore molecules. The fluorescent probes are photoswitchable molecules that can be turned on and off using light of different color. A STORM image is a reconstruction from a series of imaging cycles in which only a small fraction of fluorophores is activated, avoiding their spatial overlapping. This allows us to obtain a resolution of ∼20 nm, which is an order of magnitude below the diffraction limit.

Recent studies showed that actin, spectrin and associated proteins form a ring-like structure around the axon circumference, in a broad range of neuronal cell types including DRG neurons, with a mean distance of ~190 nm [176,177]. The typical membrane-associated periodic skeleton (MPS) of actin and spectrin is shown in Fig. 4.7. It is known to progressively develop from the proximal to distal parts of the axon and to be less developed in dendrites compared to axons [178].

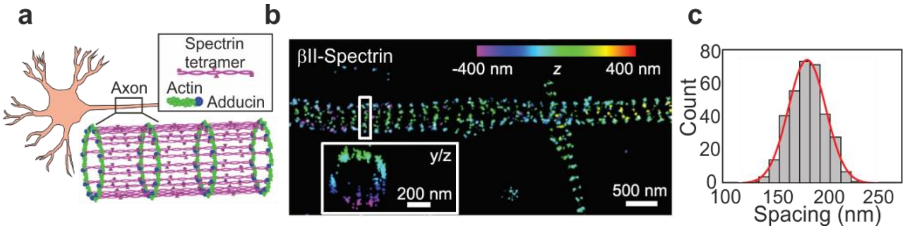

Fig. 4.7. **Membrane-associated periodic skeleton (MPS) in axons.** (a) Model for MPS in axons. Actin filament (green), capped by adducing (blue) form ring-like structure wrapping around the axons. Spectrin tetramers (magenta) connect the rings. (b) 3D-STORM image of βII-spectrin in axons. Inset: cross section showing the ring of the region depicted in the white box. (c) Histogram of the spacing between adjacent spectrin rings, with a mean distance of 182 ± 12 nm. Adapted from [176]

4.2.12.1 Fluorescent labelling for STORM imaging

STORM imaging was performed in the laboratory of Prof. Lorenzo Albertazzi (Institute for Complex Molecular Systems (ICMS), Eindhoven University of Technology, Eindhoven).

We used STORM imaging to study the ultrastructural organization of spectrin in DRG neurons. We used the protocol reported in He *et al.* [177] and Han *et al.* [179]. Neurons were fixed at DIV 2, using 4% (w/v) PFA in PBS for 20 min at RT and rinsed 3 times with PBS. Fixed neurons were then permeabilized in 0.2% (v/v) Triton-X-100 in in PBS for 5 min. After 3 washes in PBS the samples were blocked in blocking buffer (BSA 3% w/v in PBS) for 1 h and subsequently stained with primary antibodies in blocking buffer overnight at 4 °C to label βII spectrin (1:300, BD Biosciences, 612563). After 3 washes in

PBS, the samples were stained for 1 h at RT with secondary antibody anti-mouse-Alexa647 (1:100, Invitrogen, A31571). Coverslips were mounted on glass slide in Vectashield mounting medium (Vector Laboratories).

4.2.12.2 Storm sample imaging and data analysis

STORM microscopy was performed using a Nikon N-STORM system configured for total internal reflection fluorescence imaging. Alexa-647-labelled samples were excited by 647 nm laser line. An ultraviolet laser (405 nm) was used to activate the photoswitchable dyes during acquisition.

Fluorescence was collected using a Nikon 100x, 1.4 NA oil immersion objective and passed through a quad-band-pass dichroic filter (97335 Nikon). Time-lapses of 30000 frames were recorded on a 256 × 256 pixel field (image pixel size 160 nm) of an EMCCD camera (ixon3, Andor). Data were analyzed with the STORM module of NIS Elements (Nikon), ImageJ and Origin.

We selected a region of interest (ROI) in each image containing a portion of the axon with more than 5 ring-like structures and used a Fourier transform of the intensity profiles of spectrin along the axon to calculate the fundamental frequencies corresponding to the spatial period, as reported in Fig. 4.8. The intensity profiles shown in Fig. 4.8 were extracted from the ROI using the "Plot Profile" tool in ImageJ.

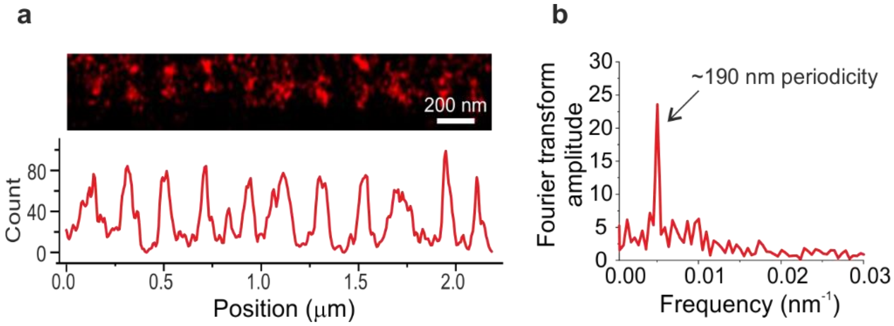

Fig. 4.8. **MPS analysis.** (a) STORM image of a segment of axon (top) with the projection to the long axis of the axon showing regular peaks (bottom). (b) Fourier transform of the projection with fundamental frequencies corresponding to the spatial period of ~190 nm.

4.2.13 Transmission electron microscopy

TEM is a technique that allows the examination of ultrastructure of fixed samples. The samples are fixed with reagents that preserve the structure, stained with heavy metals to increase the contrast and embedded in a resin that allows the sectioning using an ultramicrotome. The typical thickness of the section is 70 nm, which allows the electrons to pass through the section.

DRG neurons (DIV3) were processed by Dr. Valentina Cappello (CNI@NEST, Istituto Italiano di Tecnologia, Pisa) as described before [180]. Briefly we fixed cells on coverslips with 1.5% glutaraldehyde in 0.1 M sodium cacodylate buffer, pH 7.4, post-fixed in 1% OsO_4, 1% $K_3Fe(CN)_6$, 0.1 M sodium cacodylate buffer, stained with our homemade staining solution [181], dehydrated in a growing series of ethanol, and flat-embedded in Epoxy resin. Ultra-thin sections (80 nm) were cut with a LEICA UC7 and imaged with a Transmission electron microscope Zeiss LIBRA 120 Plus, operating at 120 KeV and equipped with an in-column omega filter; images were recorded at different magnifications. We imaged more than 30 ultra-thin section covering a thickness of around 4 μm. Both for graphene and control, we selected sections at a comparable distance from the substrate. The images related to two independent experiments were morphologically and morphometrically analysed using NIH ImageJ software.

For microtubule (MT) quantification, more than 200 axons were examined for graphene and control groups, taken for more than 25 TEM images per sample. We observed MTs running adjacent with some intersection points, and used them to measure the intratubular distance at regular intervals. We measured the MT spacing by taking a pair of MTs and following them along the axon, monitoring their distance at regular points of 200 nm using a grid.

4.2.14 Statistical Analysis

We pooled together all values from samples of the same experiment. Data were analyzed using Origin Software. ANOVA with Bonferroni multiple comparison test or Holm-Sidak post-hoc test for parametric data and by Mann-Whitney for non-parametric data were used for statistical significance with $*p < 0.05$, $**p < 0.01$ and $***p < 0.001$. Data are presented as mean ± s.e.m.

4.3 Abberior488 and Alexa488 in fluoNGF: a comparative study of labeling and axonal transport performance

4.3.1 Comparison of NGF labeling by Abberior488 and Alexa488

We examined the labeling performance of ybbR-tagged NGF by two different green excitable fluorophores: Abberior488 and Alexa488. This experiment was aimed at understanding whether both the labelling reaction on purified NGF and fluoNGF internalization in neurons are influenced by the chosen CoA-fluorophore. Indeed, the two fluorophores are distinguished by different mass, net charge and quantum yield (Table 1) and these factors may influence either the labeling reaction to a positively charged specie like NGF is, or cell internalization.

Table 1. **Fluorophores characteristics.**

Fluorophore	**Excitation wavelength (nm)**	**Emission wavelength (nm)**	**ε (M^{-1} cm^{-1})**	**Quantum Yield**	**Net charge at pH7.4**	**Mass added to the protein upon S6 conjugation (g/mol)**
Abberior 488	501	524	86000	0.89	**-2**	**1133.6**
Alexa 488	495	519	73000	0.92	**-3**	**981**

To this purpose, we produced in parallel two different preparations of fluoNGF using either CoA-Abberior488 and CoA-Alexa488 as fluorophore substrates, and our established procedure [169]. The two reaction products were then purified by ion-exchange HPLC [169]: the chromatograms in Fig. 4.9(a) show that the two fluoNGF species were both recovered in sufficient amounts, with elution times of respectively 13.3 min and 13.8 min for NGF-Alexa488 and NGF-Abberior488. Also, the concentration and recovery yields were slightly higher for NGF-Abberior488 than for NGF-Alexa488, as confirmed by SDS-PAGE analysis of the eluted fractions (Fig. 4.9(b)) and by quantification of fluoNGF concentration by spectrofluorimetry [168]. The average quantity recovered was 4.8 ± 3.0 µg for NGF-Abberior488 and 2.6 ± 1.5 µg for NGF-Alexa488. However, this might be due to some batch-to-batch variability reported for the labelling efficiency rather than to a different performance of the two fluorophores in the labelling reaction.

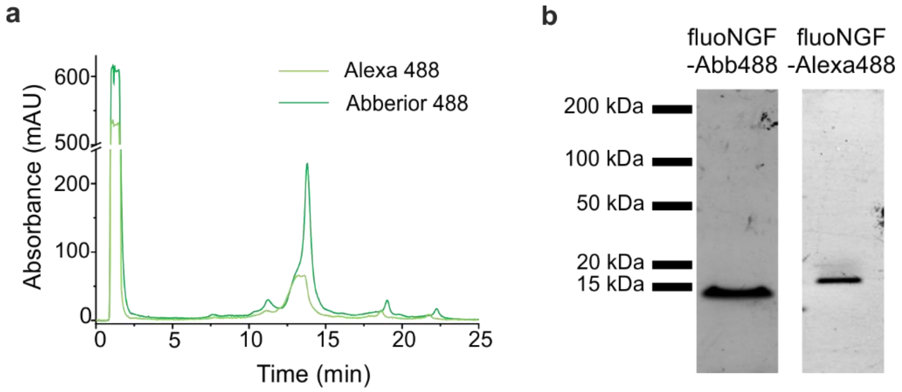

Fig. 4.9. **FluoNGF preparation.** (a) Superimposed HPLC chromatographic profiles of absorbance at 280 nm versus elution time of the reaction of fluoNGF-Alexa488 (light green) and fluoNGF-Abberior488 (dark green). (b) SDS-PAGE analysis showing ≈100 ng purified fluoNGF-Abberior488 (left) and ≈30 ng fluoNGF-Alexa488 (right) with the characteristic fluoNGF band at 14kDa, as revealed by the comparison with the standard molecular weights reported on the left.

4.3.2 FluoNGF internalization in PC12 cells

Previous studies have demonstrated that the fluoNGF is fully functional and retains all the physiological properties of the native neurotrophin in terms of cell proliferation, cell differentiation and activation of TrkA and p75NTR signal transduction pathways [168,169].

To confirm this, we checked the fluorescent neurotrophin internalization in differentiated PC12 cells, which endogenously express both NGF receptors. We tested fluoNGF-Alexa488 since it was selected to carry on the following transport measurement of fluoNGF in live DRG neurons on graphene. The cells were incubated with 100 ng/ml of fluoNGF-Alexa488 at 37 °C for 1h and imaged by confocal microscopy. Bright puncta distributed homogeneously all over the cell membrane and cytoplasm indicating the presence of fluorescent endosomes containing fluoNGF (Fig. 4.10).

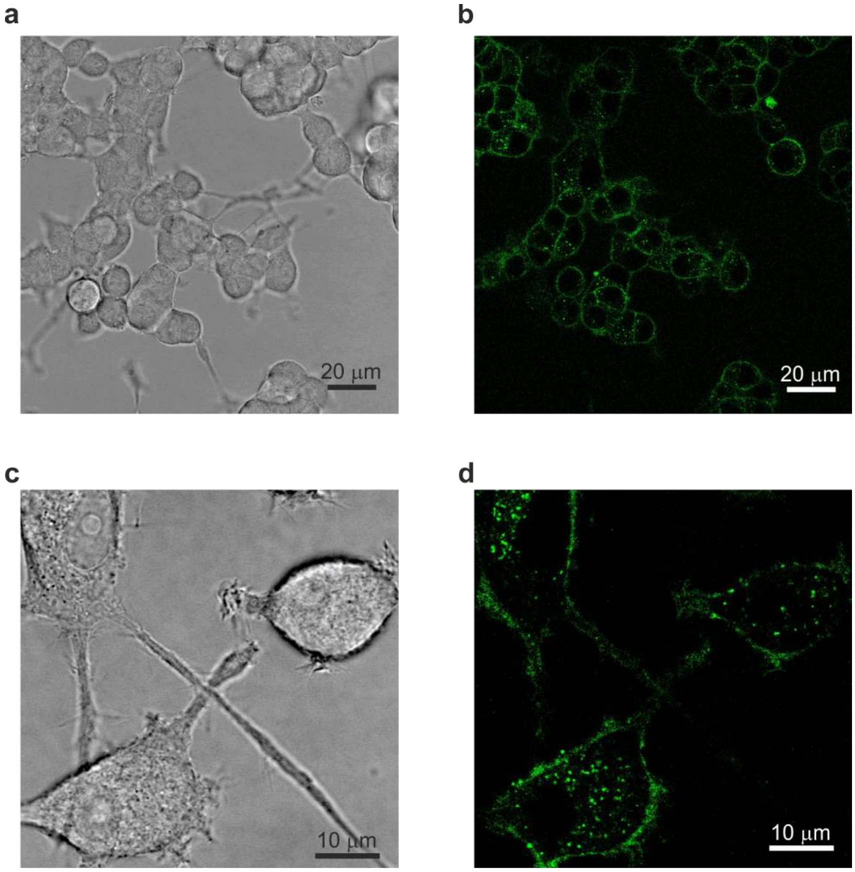

Fig. 4.10. **Live-cell confocal images of PC12 cell after 1h exposure to fluoNGF.** (a,c) Bright-field illumination (Transmitted light) of a wide field (a) and a zoomed region (c). (b,d) Fluorescent signal emitted by fluoNGF in the same areas.

4.3.3 Abberior488 and Alexa488 axonal transport comparison

We then investigated the dependence of axonal transport of NGF labelled by the two different green excitable fluorophores: Abberior488 and Alexa488.

We imaged by fluorescence microscopy the NGF vesicle flux being retrogradely or anterogradely transported in the channel compartment (Fig. 4.11(a)). We first quantified the total amount of internalized vesicles per 1 mm axon, which did not significantly differ for Alexa488 and Abberior488 conjugations (Fig. 4.11(b)). Thus, the two different fluorophores, and the different resulting fluoNGF charge after their conjugation do not affect the neurotrophin internalization process. Furthermore, we quantified in the two cases the distribution of speed of anterogradely and retrogradely moving fluoNGF vesicles (Fig. 4.11(c)), which are represented by positive and negative velocities, respectively. In agreement with our and others' previous observations [167,168], the number of vesicles transported retrogradely was significantly higher than those transported in the opposite direction. Importantly, both fluoNGF preparations showed a similar speed distribution, meaning that also the axonal transport properties are not affected by the chosen fluorophore.

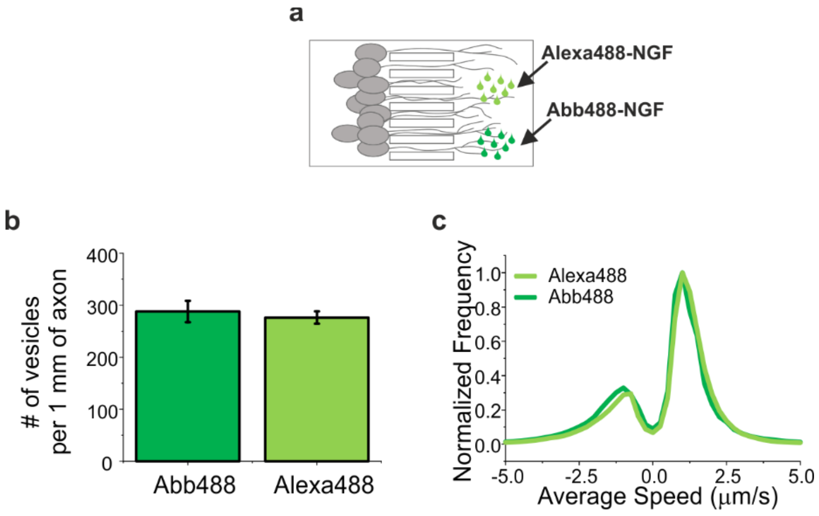

Fig. 4.11. **Abberior488 and Alexa488 axonal transport comparison**. (a) Schematic representation of the microfluidic device. DRG neurons extend their axons in the microgrooves reaching the axon compartment where fluoNGF is administered. (b) Mean ± s.e.m. of the number of vesicles per 1 mm of axons after the administration of Alexa488-NGF and Abb488-NGF at the axon compartment of DRG neurons. Data are not significantly different according to a Mann-Whitney test, with $\alpha=0.05$. The number of compartmentalized DRG cultures was 4 for NGF-Alexa488 and 2 for NGF-Abb488, with a number of vesicle of 7674 and 4089, respectively. (c) Normalized speed distribution for moving parts of vesicle trajectories. Distribution with maxima normalized at 1. The number of compartmentalized DRG cultures was 4 for NGF-Alexa488 and 2 for NGF-Abb488, with a number of moving vesicles of 1230 and 497, respectively.

4.4 Graphene promotes axon elongation in developing DRG neurons

The effect of graphene on axon outgrowth in primary peripheral neurons was investigated using DRG neurons dissected from P4 mice. All the samples were coated with PDL/laminin [45] and neurons were cultured in the presence of NGF as described in 4.2.3. In order to precisely determine axonal length, we used a compartmentalized microfluidic chamber placed on top of a graphene-coated glass coverslip (Fig. 4.12). An NGF gradient was applied to force DRG axons to reach the axonal side by crossing the microgrooves. This approach allows to selectively apply treatments to axons and mimics well the physiological NGF stimulation where the trophic factor is produced by target innervated tissues and is endocyted at the distal axon tips, far from the cell soma [182,183].

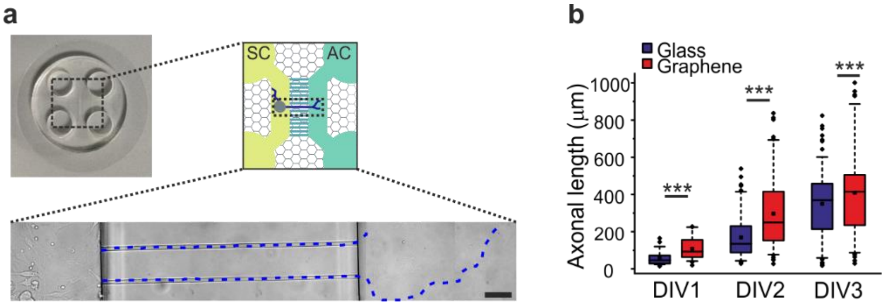

Fig. 4.12. **Increased axonal elongation in DRG neurons grown on graphene.** (a) Schematic representation of DRG axonal length quantified on graphene inside a microfluidic chamber. On the left, optical image of an assembled device on graphene. On the right, cartoon showing the microfluidic chamber with the SC and AC connected by microchannels. The bright field image shows axons crossing and filling the microchannels in blue. Scale bar: 50 µm. (b) Quantification of the axonal length at different DIV on glass and graphene in a microfluidic device. A significant difference was found between graphene and control according to Two-way Anova Test. (***P_substrate <0.001, ***P_DIV <0.0001, Two-way Anova). The number of measured axons was: DIV1, glass n=42, graphene n=50; DIV2, glass n=109, graphene n=101; DIV3, glass n=147, graphene n=119; In the box plots the horizontal line is the median value, boxed area extends from the 25th to 75th percentile, whiskers from the 5th to 95th percentiles, the square is the mean and the circles are outliers.

Fig. 4.12(b) reports the axon length distribution measured at three time points. We found gradually augmenting neurite length both on graphene and glass, with a significant increase on graphene. Remarkably, in the first two days of culture, the axons were significantly longer on graphene by 79% and 73%, respectively (Table 2). At day 3, reduced although significant differences were found, with the axons on graphene 17% longer than on glass.

Table 2. **Axonal length on microfluidic chamber at different DIV.** Length values plotted in Figure 1b, with the percentage of length increase on graphene with respect to the control at different DIV.

Substrate	DIV	Axonal length (µm)	s.e.m.	Percentage increase (%)[1]
Graphene	DIV1	115	8	79.3 %
Glass		64	6	
Graphene	DIV2	305	19	73.6 %
Glass		176	11	
Graphene	DIV3	420	22	16.6 %
Glass		360	15	

[1] Percentage increase on graphene with respect to the control.

The effect of graphene on axon outgrowth in primary peripheral neurons was investigated also with a standard approach, using neurons seeded on standard glass coverslips and on graphene transferred on glass coverslips, yielding results that further confirm preferential neuron outgrowth on graphene.

Neurons were seeded at a very low density to distinguish single axons, as reported in the schematic in Fig. 4.13. The length was quantified by manually tracing the axon from the soma to the axonal tip.

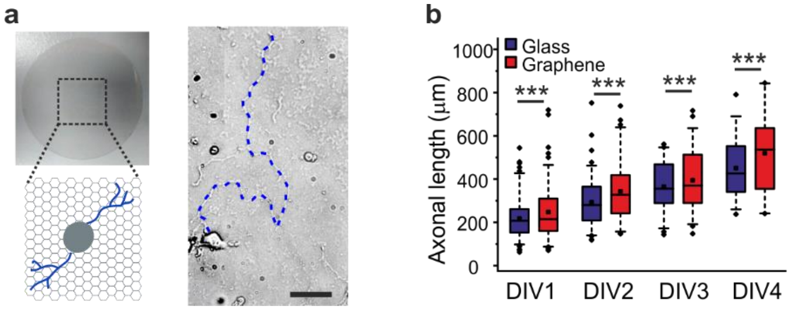

Fig. 4.13. **Morphology and axonal elongation in DRG neurons grown on graphene.** (a) Schematic representation of DRG axonal length quantified on graphene transferred on a glass coverslip. On the left, optical image of CVD grown graphene transferred on glass. On the right, the bright field image shows a neuron with axons marked in blue. Scale bar: 50 µm. (b) Quantification of the length of measurable axons at different DIV on glass and graphene. A significant difference is found between graphene and control according to Two-way Anova Test. (***P_substrate <0.001, ***P_DIV <0.0001, Two-way Anova). The number of measured axons was: DIV1, glass n=109, graphene n=106; DIV2, glass n=84, graphene n=70; DIV3, glass n=44, graphene n=51; DIV4, glass n=23, graphene n=33. In the box plots the horizontal line is the median value, boxed area extends from the 25th to 75th percentile, whiskers from the 5th to 95th percentiles, the square is the mean and the circles are outliers.

We were able to quantify the neurite length up to 4 days of culture, as later the neuronal network was too dense to distinguish isolated axons. Indeed, especially in more dense cultures, already after 3 days of culture, cells on graphene displayed a more complex distribution, a network of small cell-body aggregates connected by axons, differently from the control surface where they distributed homogeneously (Fig. 4.14(a)). This is more evident after axon immunostaining using anti-neurofilament heavy (NHF) antibody (Fig. 4.14(b)).

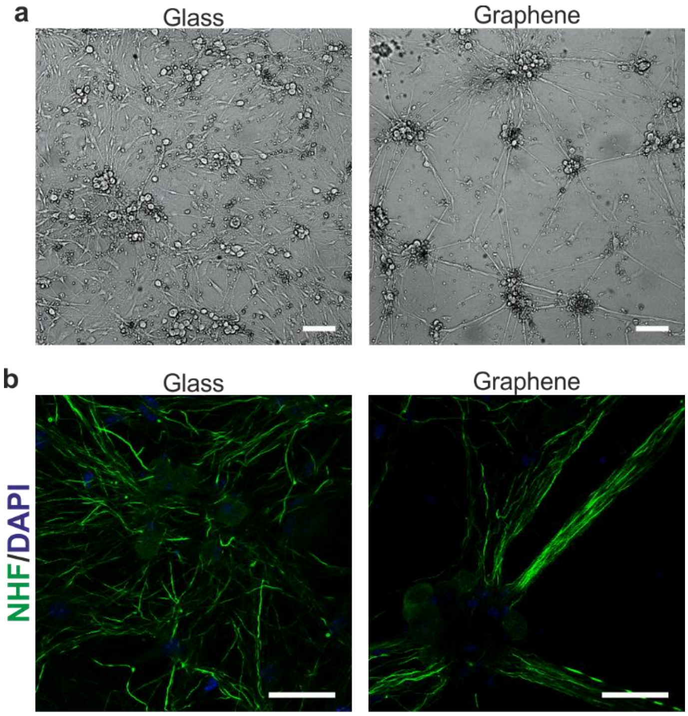

Fig. 4.14. **DRG neurons morphology.** (a) Representative bright field images showing DRG neuron morphology on glass and graphene after 3 DIV. (b) Fluorescent microscopy images of DRG neurons stained with NHF to identify axons and DAPI to identify nuclei.

Fig. 4.13(b) reports the axon length distribution measured on a coverslip at four time points. We found gradually augmenting neurite length both on graphene and glass, with a significant increase on graphene. The maximal elongation was observed at DIV2 where the axons were up to 17% longer than the control. For the details, see Table 3.

Table 3. **DRG axonal length in standard culture at different DIV.** Length values represented in the box plot in Fig. 4.13, with the percentage of length increase on graphene with respect to the control at different DIV.

Substrate	**DIV**	**Axonal length (μm)**	**s.e.m.**	**Percentage increase (%)**[1]
Graphene Glass	DIV1	247 218	12 9	13.4 %
Graphene Glass	DIV2	343 292	16 13	17.3 %
Graphene Glass	DIV3	394 365	20 17	8.1 %
Graphene Glass	DIV4	519 450	33 30	15.4 %

[1] Percentage increase on graphene with respect to the control.

In the compartmentalized approach, as reported in Fig. 4.12, we observed a significant slower elongation at DIV1 and DIV2, both for graphene and control compared to the standard approach (Two-way Anova Test. (***P <0.001)) (Table 4), that may be ascribed to the reduced NGF stimulation felt by axons inside the microchannels.

Table 4. **DRG Axonal length in standard and compartmentalized cultures at different DIV.** Comparison between the length values reported in the box plots in Fig. 4.12 and Fig. 4.13, with the percentage of length increase on standard approach involving the coverslips with respect to the microfluidic chamber.

DIV	Substrate	Approach	Axonal length (μm)	s.e.m.	Percentage increase (%)[1]
DIV1	Glass	Chamber	64	8	240
		Coverslip	218	9	
	Graphene	Chamber	115	8	130
		Coverslip	265	12	
DIV2	Glass	Chamber	176	11	66.3
		Coverslip	292	13	
	Graphene	Chamber	305	19	12.4
		Coverslip	343	16	
DIV3	Glass	Chamber	360	15	1.4
		Coverslip	365	17	
	Graphene	Chamber	420	22	6.4
		Coverslip	394	20	

[1] Percentage increase on coverslips with respect to the microfluidic chamber.

Also, the obtained results support the trend previously reported for embryonic DRG neurons on epitaxial graphene, where both at DIV1 and DIV2 the average axon length was higher on graphene than on the other observed substrates [45]. Furthermore, the time-dependent axonal increase well agrees with what reported for non-compartmentalized hippocampal neurons on CVD graphene, where an initial ~30% increased elongation was reported for DIV2, followed by a stabilization at ~13% more in the following days. It is thus established that graphene strongly impacts the early development of axon elongation in peripheral sensory neurons.

4.5 Graphene alters retrograde transport of Nerve Growth Factor signaling endosomes

As discussed in 4.1, survival of sympathetic and sensory neurons is known to rely on the retrograde axonal transport of NGF signaling endosomes back to the cell body [46,47,184] , while numerous studies indicate that axon elongation is prompted by a local effect of NGF which does not directly involve mechanisms in the cell body [185,186]. Hence, we examined whether the observed graphene-induced axon outgrowth is correlated with an altered NGF axonal transport.

To assess the effect of graphene on the transported vesicles, NGF vesicular trafficking was examined, using glass as control. Visual inspection of the detected vesicles suggested that graphene induces a strong reduction of retrogradely transported NGF vesicles at DIV2, while this is not the case at DIV5 (Fig. 4.15)

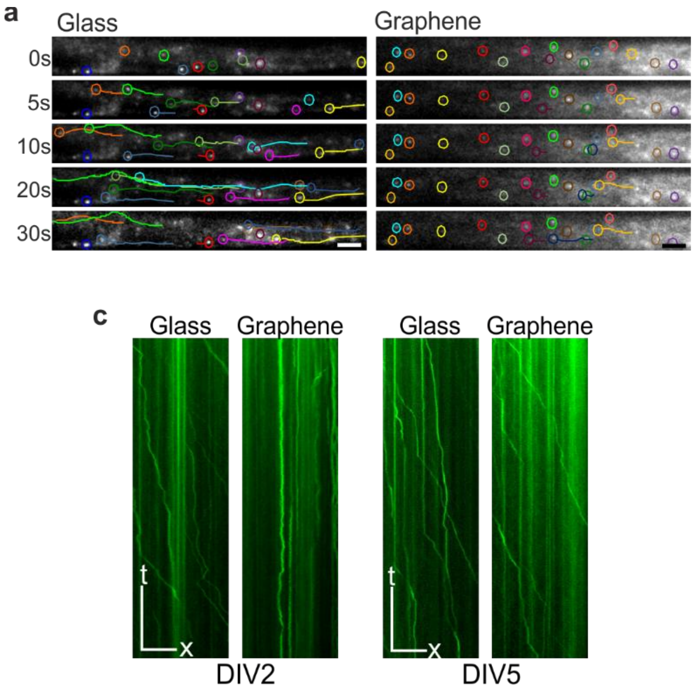

Fig. 4.15. **Live axonal transport of fluo-NGF on graphene.** (a) Representative images of the time lapse videos of NGF vesicles of DRG axons on glass and graphene. Colored circles underline vesicles at the end of a time-movie; the line in the same color-code highlights the trajectory run by that vesicle during the time-movie. Scale bar: 5 µm. (b) Representative kymographs of fluoNGF vesicles along a single axon at DIV2 and DIV5. x-scale bar: 5 µm; y-scale bar: 10 s.

To clarify if the altered retrograde transport in graphene is due to an altered vesicle internalization, we quantified the total amount of internalized vesicles, expressed as number of particles per 1 mm of axon (Fig. 4.16) in control and graphene, and found no significant difference between the two groups, both at DIV2 and DIV5. This is in agreement with the reported unmodified neuron survival rate on graphene compared to the control [45].

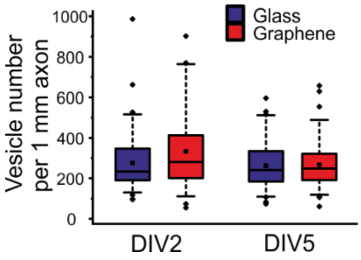

Fig. 4.16. **Amount of internalized vesicles on graphene and glass at DIV2 and DIV5.** Box plots illustrating the number of vesicles per 1 mm of axons after the administration of fluoNGF at the axon compartment of DRG neurons cultured on graphene and glass at DIV2 and DIV5. Data are not significantly different according to a Mann-Whitney test. In the box plots the horizontal line is the median value, boxed area extends from the 25th to 75th percentile, whiskers from the 5th to 95th percentiles, the square is the mean and the circles are outliers. The number of vesicles at DIV2 in three independent cultures was 3604 for graphene and 5188 for glass. The number of vesicles at DIV5 in two independent cultures was 4905 for graphene and 5399 for glass.

We next ruled out that the observed effect was due to a slowing down of the vesicle movement. We thus quantified the velocities during retrograde and anterograde motion of the vesicles on graphene and glass (represented by positive and negative velocities, respectively, in Fig. 4.17). We found that velocities of anterograde and retrograde transport were not altered by graphene both at DIV2 and DIV5. Also, we observed, similarly to what reported in [167,168], that on glass vesicles moved preferentially with retrograde movement than with anterograde one, resulting in an asymmetric distribution. Surprisingly, on graphene we observed a symmetric distribution at DIV2, indicating a comparable retrograde and anterograde movement for NGF vesicles. On the contrary, at DIV5 vesicles on graphene and glass exhibited similar distributions of speeds with predominant retrograde transport.

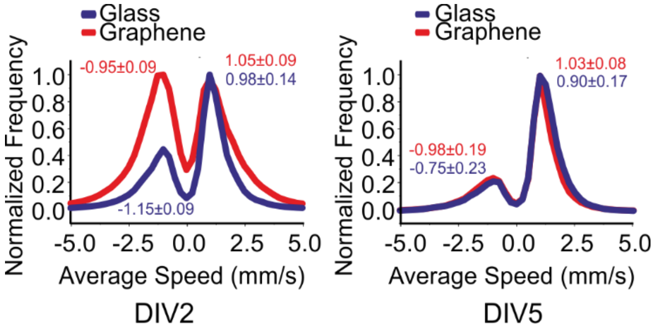

Fig. 4.17. **Normalized speed distribution for moving parts of vesicle trajectories on graphene and glass at DIV2 and DIV5.** The mean ± standard deviation (SD) of each peak is reported in the graph in the same color scale. Distributions with maxima normalized at 1. The number of vesicles at DIV2 in three independent cultures was 3604 for graphene and 5188 for glass. The number of vesicles at DIV5 in two independent cultures was 4905 for graphene and 5399 for glass.

The obtained data prompted us to analyze the entire population of NGF vesicles and classify them based on their movement. We distinguished four different categories: stalled (stl), retrograde (ret), anterograde (ant) and oscillating (osc).

We found that in graphene and control the majority of the NGF vesicles were stalled, both at DIV2 and DIV5 (Fig. 4.18).

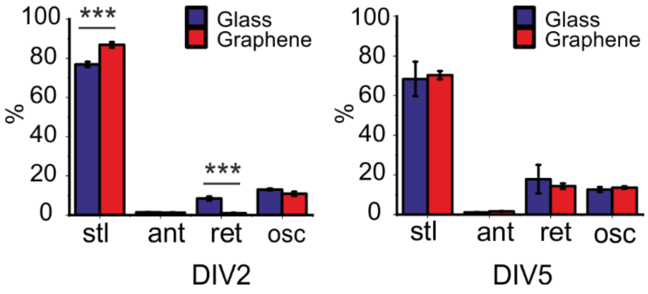

Fig. 4.18. **Histograms showing the mean ± s.e.m. of the percentage of vesicles for each population at DIV2 and DIV5 of the independent cultures.** Vesicles were classified in four categories: stalled (stl), retrograde (ret), anterograde (ant) and oscillating (osc). The percentage of stalled and retrograde vesicles on graphene at DIV2 were significantly different from the control (***P<0.0001, One-way Anova, with Bonferroni's Multiple Comparison Test). The distribution of the populations at DIV5 did not significantly differ, according to One-way Anova. The number of vesicles at DIV2 in three

independent cultures was 3604 for graphene and 5188 for glass. The number of vesicles at DIV5 in two independent cultures was 4905 for graphene and 5399 for glass.

However, on graphene at DIV2 the number of retrogradely transported vesicles was 8.5-fold reduced with respect to the control, in favor of a 13% increase of the stalled vesicles. Details about the percentage for each movement category are reported in Table 5

Table 5. **Percentage of vesicles for each movement category at DIV2 and DIV5.** Percentage of vesicles represented in the box plot in Fig. 4.18 in the main text.

Movement categories	**Substrate**	**Percentalge (%)**	**s.e.m.**	**DIV**
Stalled	Graphene	86.9	1.4	DIV2
	Control	76.9	1.3	
	Graphene	70.3	2.0	DIV5
	Control	68.4	1.1	
Retrograde	Graphene	1.0	0.2	DIV2
	Control	8.5	1.0	
	Graphene	12.1	1.1	DIV5
	Control	16.0	1.6	
Anterograde	Graphene	1.2	0.2	DIV2
	Control	1.3	0.2	
	Graphene	1.6	0.2	DIV5
	Control	1.0	0.1	
Oscillating	Graphene	9.7	0.8	DIV2
	Control	12.2	0.6	
	Graphene	12.8	0.7	DIV5
	Control	11.4	0.7	

When comparing the oscillating and anterograde populations we found no significant difference between graphene and control. Importantly, these data could not have been appreciated when using previous analysis methods, which apply a threshold in the speed or in the distance covered by the vesicles

[168,183,187]. Hence, it appears that in the first developmental stage the graphene effect on NGF transport is to reduce retrogradely moving vesicles in favor of a locally stalled population. Importantly, this effect almost disappears in more mature DRG cultures, where we found that both the percentage of stalled and moving vesicles were superimposable to control (Fig. 4.18). Thus, graphene alters NGF retrograde transport in a time-dependent fashion that perfectly matches its predominant effect at early developmental phase in axon elongation (Fig. 4.12), suggesting a causal role for this trafficking alteration in the process. We next investigated possible electrophysiological and structural changes prompted by the material, that may help to better elucidate the cause-effect links between material interface, NGF vesicle stall and axon elongation.

4.6 Reciprocal charge redistribution between graphene and neuronal membrane

Electric activity has been recently associated to increased retrograde flux and reduced dwell time of signaling endosomes in hippocampal neurons [188]. Also, it has been indicated that graphene influences central neurons excitability by modifying the extracellular concentration of potassium (K^+) ions and thus the ionic currents [27]. Accordingly, it can be expected that graphene induces a measurable variation in the neuron membrane potential and electrical activity also in DRG neurons, which may provide an explanation for the observed altered NGF trafficking on graphene. Hence, we carried out patch-clamp electrophysiology measurements to study the effect of graphene on membrane resting potential and neuron excitability. To allow a direct comparison with the previously reported axonal elongation and transport studies, experiments were performed at similar time points. Indeed, we observed a significant hyperpolarized resting membrane potential for graphene-cultured DRG neurons with respect to glass-cultured controls [24], regardless of the DIV investigated with a reduction of the hyperpolarization at DIV4, that can be appreciated in the trend of membrane potentials (Fig. 4.19).

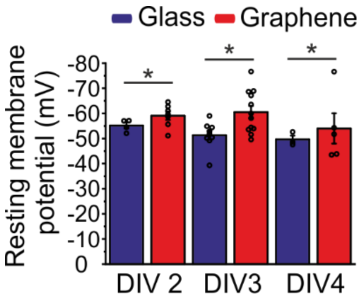

Fig. 4.19. **DRG resting membrane potential on glass and graphene.** Graphene-cultured DRGs show hyperpolarized resting membrane potential in comparison to glass-cultured controls (*P_substrate <0.05, Two-way Anova). The number of measured neurons, collected in three independent cultures, was: DIV2, glass n=4, graphene n=7; DIV3, glass n=9, graphene n=12; DIV4, glass n=3, graphene n=5.

Neural activity was further investigated by evoking action potential in response to an increasing injected current. When comparing the number of spikes, we observed that at DIV2 the mean number of spikes in graphene was significantly lower than in the control (Fig. 4.20). However, this difference disappeared at DIV4, where control and graphene neurons displayed a similar number of spikes (Fig. 4.20).

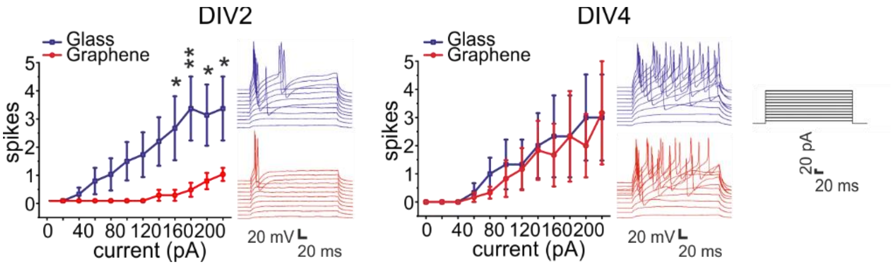

Fig. 4.20. **Spike number in response to current injection and representative traces on graphene and glass-cultured DRG at different DIV.** On DIV2, graphene-cultured DRGs show reduced spike number in response to current injection with respect to glass-cultured controls. On DIV4, no difference in spiking was observed between graphene- and glass-cultured DRGs according to Two-way Anova Test. (**P_substrate X current <0.001, ***P_substrate X current <0.0001, Two-way Anova, with Holm-Sidak post-hoc test). The number of measured neurons, collected in three independent cultures, was: DIV2, glass n=5, graphene n=6; DIV4, glass n=3, graphene n=6.

These results demonstrate that the early days of contact with graphene are also characterized by a change in neuron excitability. This is followed by a phase of adaptation, in which neurons reach a less hyperpolarized membrane potential which likely accounts for the recovered excitability. It is known that carbon-based pi-electron-rich surfaces are ideal adsorption sites for K^+ ions [189,190]. Accordingly, a modified (i.e., reduced) extracellular K^+ concentration due to preferential adsorption of K^+ ions at the graphene surface was recently proposed to explain the tonically firing phenotype of hippocampal neurons on graphene [27]. We propose that the same K^+ gradient may also explain the observed decreased DRG excitability. Indeed, due to the more negative resting membrane potential of DRG with respect to central neurons [191], it is reasonable to assume that an increased flux of K^+ ions decreases neuron firing in the former case. The recovered excitability at day 4 is likely due to the reduced hyperpolarization. These data support the hypothesis that the altered NGF retrograde transport observed on graphene in the developmental phase depends on a varied DRG excitability. Specifically, we correlate the reduced retrograde transport with a reduced DRG excitability. Once the latter is restored with time, also a normal retrograde transport is recovered, guaranteeing neural survival [192].

The observed electrophysiological alterations are most probably the results of a strong electrostatic interaction in the neuron-graphene system. A previous study has demonstrated that when a cell interacts with graphene, the surface charge present on the membrane of the cell exerts a negative potential on graphene, changing its charge-carrier concentration [75].

Table 6 shows the carrier concentration of two representative graphene sample, coated and immersed in medium. In all the presented cases, the positive values displayed for the sheet concentration confirm holes as majority carriers in all the conditions, demonstrating an intrinsic p-type doping of the graphene substrates.

Table 6. **Sheet carrier concentration for pristine graphene, after coating and after cell medium.** Measurements were performed using an Ecopia HMS-3000 Hall System operating in van der Pauw configuration.

Sample		Sheet concentration (cm^{-2})
1	As transfer	2.11×10^{13}
	Post coating	1.6×10^{13}
	Post medium	9.99×10^{12}
2	As transfer	2.29×10^{13}
	Post coating	1.22×10^{13}
	Post medium	6.75×10^{12}

The holes concentration in the p-type graphene could thus justify the strong graphene interaction with the negatively charged surface of the cell membrane [193]. To understand if a charge redistribution on the substrate occurs in the neuron proximity also in our experimental conditions, we performed Raman spectroscopy and mapping on DRG neurons at DIV2 on graphene (Fig. 4.21(a)).

Fig. 4.21(b) shows the comparison of two representative Raman spectra obtained on bare graphene (red line) and on the neuron/graphene system following sample fixation with PFA (4% w/v) (green line).

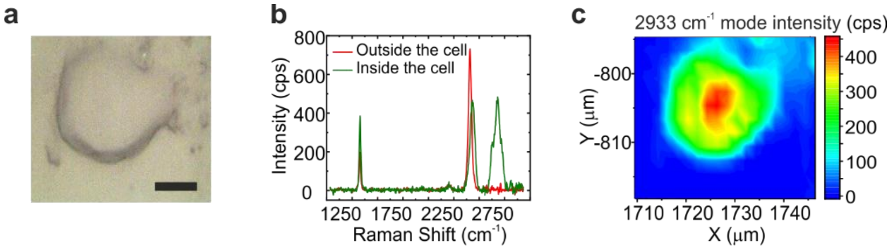

Fig. 4.21. **Raman characterization of the neuron/graphene system.** (a) Bright field of the DRG neuron on graphene. (b) Representative Raman spectra obtained on bare graphene (red line) and on

neuron/graphene interface at DIV2 (green line). (c) Raman map of the 2933 cm^{-1} mode intensity, identifying the cell position.

It is worth noting that the defect activated Raman mode (D mode) [172,194] is absent in both spectra, indicating the high quality of the employed material and that the PDL/laminin coating and cell growth do not induce any damage on the underlying graphene. In the neuron/graphene system spectrum in addition to the well-known G and 2D Raman modes [194], a complex band peaked at 2933 cm^{-1}, with one shoulder at 2885 cm^{-1} is present. These Raman modes can be attributed to the cell and in particular to the CH_3 stretching (proteins) and to the CH_2 antisymmetric stretching (lipids), respectively [195]. Fig. 4.21(c) shows the Raman map of the 2933 cm^{-1} mode intensity, identifying the cell position.

As discussed in 2.2.3, the 2D/G ratio is a benchmark for graphene doping [109], meanwhile the position of the G and 2D modes is employed as an indicator for the possible tensile/compressive strain of the graphene lattice [110].

Fig. 4.22 shows the 2D/G intensity ratio distribution of a bare graphene area after coating with PDL/laminin and after the cell growth. There are no main modifications to the distribution, indicating a homogeneous graphene doping. In case of pristine graphene, the distribution has the peak with relative FWHM at (4.5 ± 1.2), after the coating the distribution peak increases up to (5 ± 1) with a tail toward low values. After the cell growth the distribution has the peak at (4.5 ± 1.3).

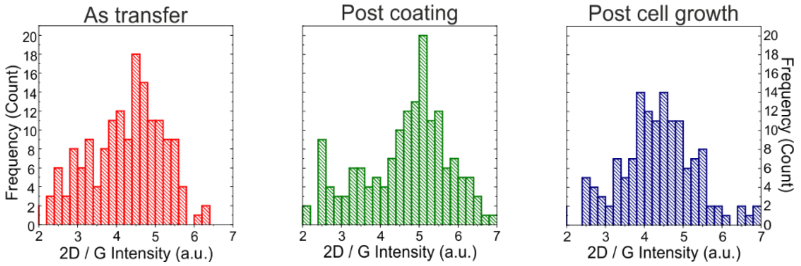

Fig. 4.22. **2D/G intensity ratio distribution of bare graphene (red), graphene after coating with PDL/laminin (green) and after the cell growth (blue).**

We then evaluated the doping in the same neuron/graphene system reported in Fig. 4.23. The 2D/G intensity ratio map was found to be decreased precisely underneath the neuron (Fig. 4.23(a)). Indeed, the histogram in Fig. 4.23(b) shows a bimodal distribution, where the distribution of 2D/G intensity ratio of bare graphene is peaked at 2.8, while the ratio in case of the graphene underneath the neuron decreases down to 1.5. This result is a clear indication of the increase of the local doping of graphene underneath the neuron.

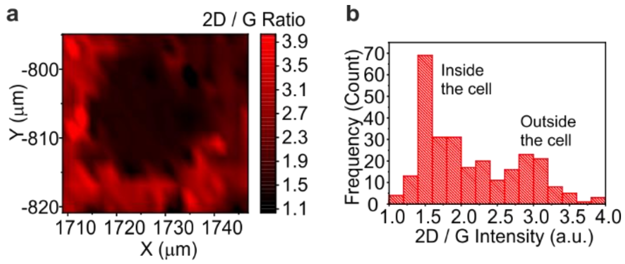

Fig. 4.23. **2D/G intensity ratio in the neuron/graphene system.** (a) Map of the same area reported in Fig. 4.21, revealing a shift of the ratio in the area underneath the cell. (b) Histogram of 2D/G intensity ratio showing the bimodal distribution of the intensity outside the neuron and the intensity underneath the neuron.

We ascribe the discrepancy between the values of 2D/G Intensity after cell growth reported in Fig. 4.22 and the values reported in Fig. 4.23 to the sample fixation.

Comparing the data with literature [109], it is possible to demonstrate that graphene doping increased from $2x10^{12}$ cm^{-2} to $6x10^{12}$ cm^{-2} when the neuron is on top of it. This value is in agreement with that reported for a graphene-astrocytes system [75]. This increased doping could be ascribed to the aforementioned cell-enhanced graphene-cation interaction, ultimately impacting cell excitability [27].

Another important benchmark for the quality of graphene is the FWHM of the 2D mode. The broadening of the 2D peak is attributed to nanoscale strain fluctuations [111].

Also in this case we first assessed the strain distribution on bare graphene and after the polymeric coating and the cell growth. Fig. 4.24 shows the 2D FWHM for pristine graphene, after coating and after cell growths, respectively. In all the presented cases, the distribution is peaked at 27 cm^{-1} with a FWHM of 2 cm^{-1} and a tail toward higher values, demonstrating the presence of areas with larger strain fluctuations.

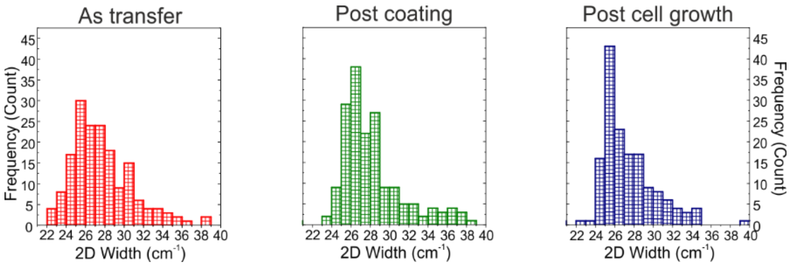

Fig. 4.24. **2D mode FWHM distribution of bare graphene (red), graphene after coating with PDL/laminin (green) and after the cell growth (blue).**

We then analyzed the 2D mode FWHM of the same neuron-graphene system reported in Fig. 4.25, revealing that the 2D mode get narrower in the case of graphene underneath the neuron (Fig. 4.25(a)). This is supported by the 2D FWHM distribution in Fig. 4.25(b), where the bimodal distribution demonstrates that the peak set at 30 cm^{-1} is mainly due to the area under the cell meanwhile the peak at 37 cm^{-1} is due to bare graphene. This indicates a reduced graphene structural deformation under the cell [111]. However, this sharpening effect of the 2D peak is not homogeneous under the cell, there is an area on the right side of the cell where the 2D FWHM shows an increase up to 40 cm^{-1}, demonstrating that the interaction between graphene and neurons has a complex behavior.

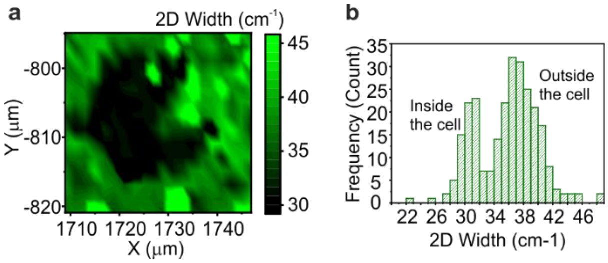

Fig. 4.25. **2D mode FWHM in the neuron/graphene system.** (a) Raman map of the 2D mode FWHM of the same area reported in Fig. 4.21. (b) Histogram of 2D mode FWHM showing the bimodal distribution of the width of graphene outside or underneath the neuron.

Also in this case we observed a discrepancy between the values of 2D FWHM after cell growth reported in Fig. 4.24 and the values reported in Fig. 4.25 and ascribed this difference to the sample fixation.

Fig. 4.26 (a) and (b) show the position maps of graphene 2D and G mode obtained on the same neuron/graphene system. In both the maps, the G and 2D modes are shifted to higher Raman shift in case of the neuron/graphene system. The position of the G and 2D modes is employed as an indicator for the possible tensile/compressive strain of the graphene lattice [110]. The correlation plot in panel (c) shows that the area under the cell suffers a tensile stress in comparison to the bare graphene [111]. This tensile stress can be due to the growth of neurites after 2 days of the cell deposition.

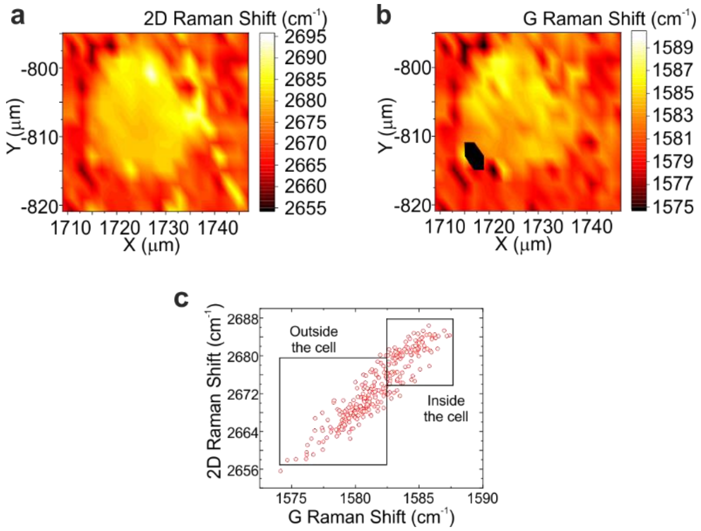

Fig. 4.26. **2D and G mode shift in the neuron/graphene system.** (a) Raman map of the position of the 2D mode. (b) Raman map of the position of the G mode. (c) Correlation plot of the 2D-G Raman peaks position.

4.7 Reduced microtubule distance and a stretched axonal topology of axons on graphene

The axonal cytoskeleton is a complex system of proteins including MTs and actin filaments that ensures shape maintenance, capacity to direct movements and extension of the growth cone [196]. In particular, NGF retrograde axonal transport is mediated by the dynein-MT transport system [163]. To rule out whether the altered NGF axonal transport observed at DIV2 could be related to alterations in the axon cytoskeleton or whether the neuron/graphene system interaction could influence axonal structure, we examined axonal topology and MTs organization of axons grown on graphene.

We first investigated the membrane-associated periodic skeleton (MPS). We examined the MPS with STORM, to study possible variations induced by graphene. DRG neurons were fixed at DIV2 and immunostained for βII spectrin for STORM imaging (Fig. 4.27).

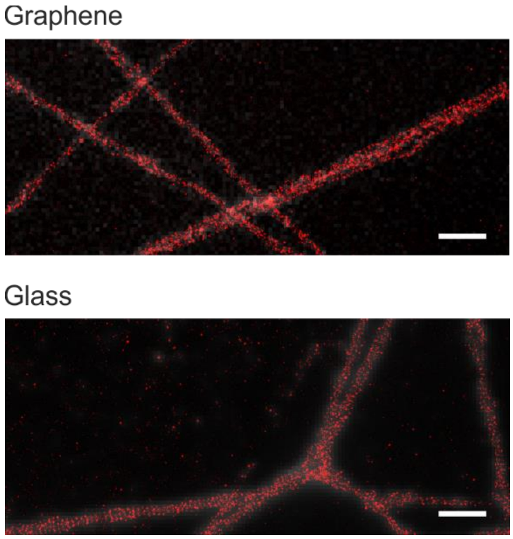

Fig. 4.27. **Periodic MPS observed in axons by using STORM.** Representative STORM images of βII spectrin (red) in DRG neuron cultured on glass and graphene fixed at DIV2 overimposed to conventional fluorescence images (grey). Scale bar: 20 μm.

We found that graphene-cultured neurons maintain the characteristic periodicity of ~ 190 nm of the MPS (graphene, 195.6 ± 20.8 nm vs. glass, 196.7 ± 14.9 nm, Fig. 4.28(b)).

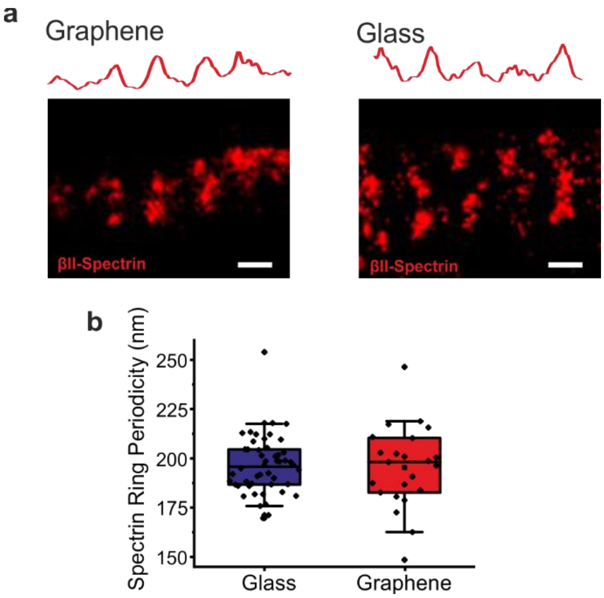

Fig. 4.28. **Spectrin ring periodicity.** (a) Magnification of the STORM images with intensity profiles across the periodic spectrin structure reported with a red line. Scale bar: 200 nm. (b) Box plots showing the periodicity of spectrin ring-like structure, which did not significantly differ according to Mann Whitney Test. The number of analyzed regions is 21 for graphene and 48 for glass from two independent cultures. In the box plot the horizontal line is the median value, boxed area extends from the 25th to 75th percentile, whiskers from the 5th to 95th percentiles.

However, the super-resolution approach also allowed us to distinguish the presence of regions in which the MPS expands radially, following an increased axon diameter (Fig. 4.29).

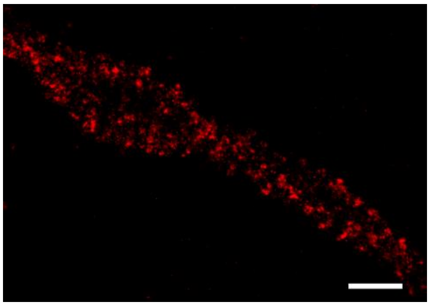

Fig. 4.29. **Fluctuation of spectrin ring diameter.** Scale bar: 500 nm.

This structures resemble the transient radial expansion of the hippocampal axonal diameter controlled by non-muscle myosin-II and induced by the passage of axonal large cargoes previously reported by Wang et coworkers [197]. They demonstrated that the axon diameter expands proportionally to the size of the cargo by stretching the axon membrane without affecting the microtubule structure and preserving the MPS periodicity. This results in fluctuation of MPS diameter that augments the mobility of the long-range retrograde carriers by increasing the number of fast-moving carriers at the expense of the pausing ones.

We quantified the number of these MPS radial expansions over an axonal length of 10 µm and we found that on graphene there were less than half radial expansions than on the control (Fig. 4.30).

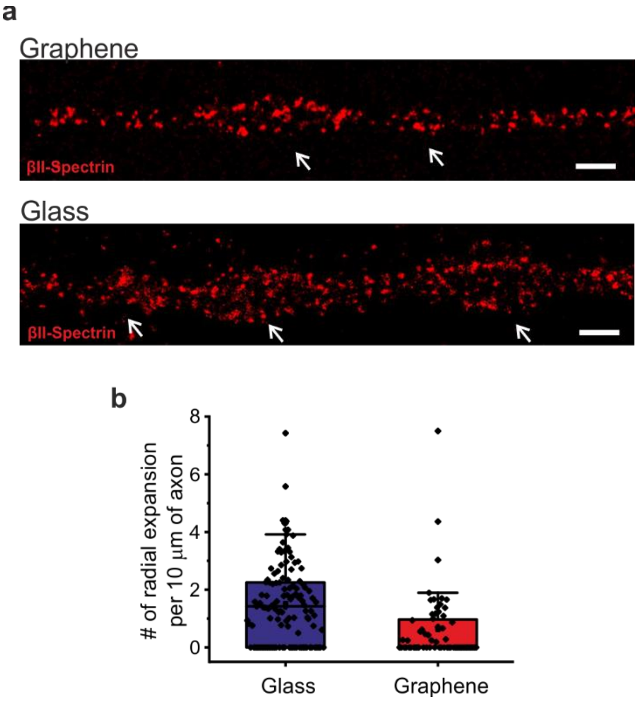

Fig. 4.30. **Radial axon expansions in graphene and glass substrates.** (a) Magnification of the STORM images with white arrows indicating the radial axon expansions (Scale bar: 500 nm) (b) Box plots of the number of axonal twists per 10 µm of axon, showing a significantly higher number of twists on glass than on graphene (***P<0.0001, Mann Whitney Test). The number of analyzed axons is 68 for graphene and 150 for glass from two independent cultures. In the box plots the horizontal line is the median value, boxed area extends from the 25th to 75th percentile, whiskers from the 5th to 95th percentiles.

Since these structures have been associated to an increase in the transport of large carriers, such as the endosomes involved in the NGF retrograde transport, this result suggests that the altered axonal transport in graphene might be also due to the reduced axon relaxation and an increase in the axon radial contractility, which may impact the cargo mobility.

We then exploited TEM to analyze MT organization and density in longitudinal sections of the DRG culture (Fig. 4.31) to identify possible structural causes that justify the alterations in the axonal transport.

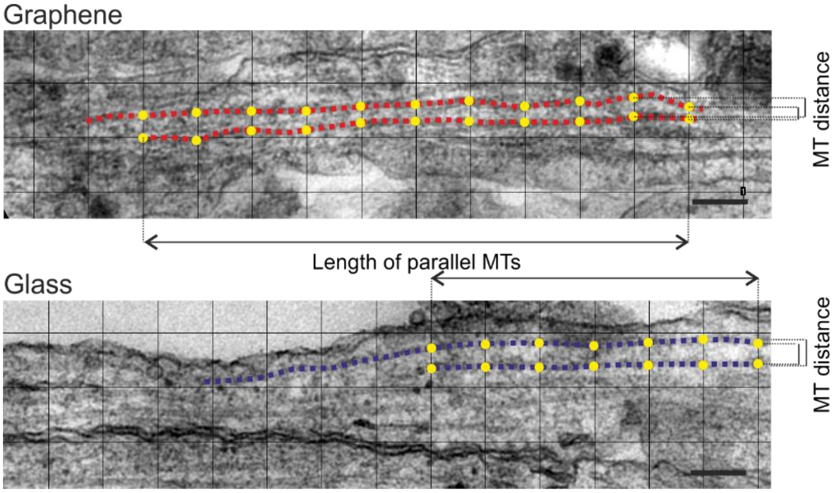

Fig. 4.31. **Representative TEM images for quantifying axon diameter, number, density, and spacing of MTs of DRG cultured on graphene and glass.** Scale bar: 200 nm. The morphological assessment of MTs is reported on the images. A couple of adjacent MTs is highlighted with dotted red lines (graphene) or with dotted blue lines (glass). Grid-pattern lines are superimposed in black and the intersection points of the grid lines with the MT, used to quantify the MT distance, are highlighted in yellow. The length of parallel MTs and the MT distance are also reported.

In detail, we quantified the spacing between adjacent couples of MTs on graphene with respect to the control. We found that on graphene, the intratubular distance was significantly reduced by 19% when compared to the control (Fig. 4.32).

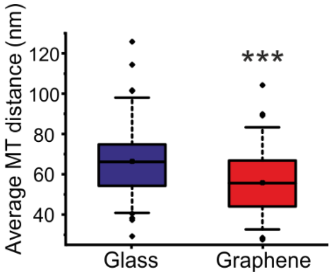

Fig. 4.32. **Average MT distance.** Box plots showing the average distance between a couple of microtubules within axons on glass and graphene (***P<0.0001, Mann Whitney Test). In the box plots the horizontal line is the median value, boxed area extends from the 25th to 75th percentile, whiskers from the 5th to 95th percentiles, the square is the mean and the circles are outliers. The number of analyzed couples was 79 for graphene and 97 for glass from two independent cultures.

In order to exclude an effect of the axon caliber on this measure [198], we also quantified the mean axon diameter (by measuring the mean axon section width) and the number of observed MTs per axon, which were found to be comparable in the two cases (Fig. 4.33).

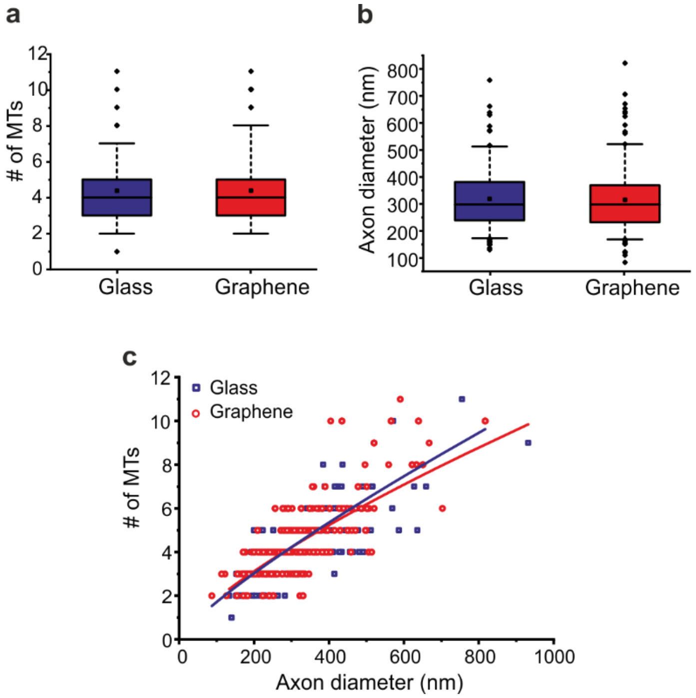

Fig. 4.33. **MT number and axon diameter quantification.** (a,b) Box plots showing the MT number and axon diameter for graphene and glass. The values did not differ significantly. In the box plots, the horizontal line is the median value, boxed area extends from the 25th to 75th percentile, whiskers from the 5th to 95th percentiles, the square is the mean and the circles are outliers. The number of analyzed axons from two independent culture was 79 for graphene and 97 for glass. (c) Dependency of the microtubule number on axon diameter for graphene (red circle) and glass (blue circle). The populations overlapped and are not distinguishable. The MT number (N_{MT}) dependency on axon diameter (D) resembled the power law previously reported [198]

$$N_{MT} = aD^{m}$$

where a and m are the fitting parameters for the power law, where a=0.0595 and m=0.7472 for glass and a=0.0390 and m=0.8215 for graphene.

These data agree with a parallel immunofluorescence quantification of tubulin we performed in the two cases. In order to compare tubulin content in DRG neurons axons on graphene and control, we selected ROI containing all the axons in the field, removing contributions of cell bodies and glial cells (clearly visible thank to a concomitant phalloidin staining) and we calculated the mean tubulin intensity by averaging the mean intensity inside each ROI. We quantified the mean fluorescence intensity of Alexa488-labelled βIII-tubulin, showing a similar result for graphene and control (Fig. 4.34).

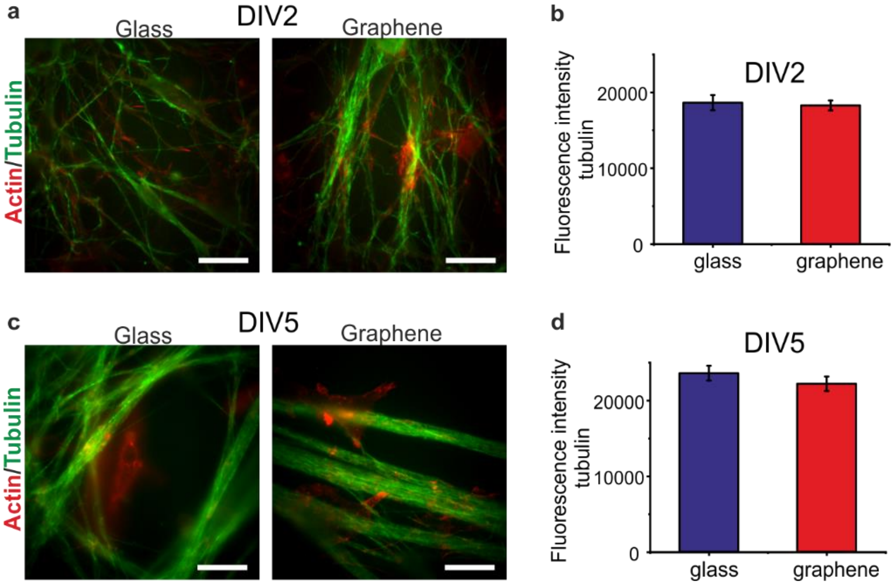

Fig. 4.34. **DRG neurons tubulin quantification.** (a,c) Representative TIRF microscopy images of neural culture stained with phalloidin to identify actin and β-III tubulin to identify axons at DIV2 (a) and DIV5 (c). (b.d) Histograms showing the mean ± s.e.m of the fluorescence intensity of Alexa488-labelled tubulin in DRG neurons in the selected ROI at DIV2 (b) and DIV5 (d). More than 25 fields were analyzed for each condition. The number of acquired ROI containing axons was 31 for glass and 51 for graphene at DIV2 and 31 for glass and 28 for graphene at DIV5.

Interestingly, TIRF microscopy allowed us to appreciate the cellular structures closer to the substrate. We observed that in the case of graphene, but not glass, the axons were on the same focal plane of glial cells which grow in close adhesion to the substrate. This may indicate an increased adhesion of neural extensions to the graphene substrate.

We thus ascribe the different MT spacing to a different three-dimensional architecture of axons grown on graphene when compared to control ones.

Moreover, as reported in Fig. 4.35, we measured the length for which the pairs of MTs arranged into adjacent arrays remains parallel along the same axon and found that this parameter exhibits a remarkable 42% increase in graphene with respect to the control sample.

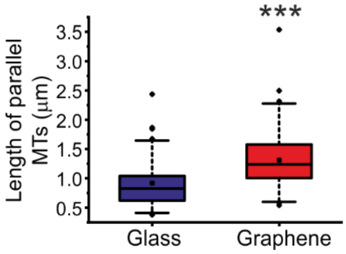

Fig. 4.35. **Length of parallel MTs.** Box plots showing the length of a microtubule couple that remain parallel inside the axon on glass and graphene (***P<0.0001, Mann Whitney Test). In the box plots the horizontal line is the median value, boxed area extends from the 25th to 75th percentile, whiskers from the 5th to 95th percentiles, the square is the mean and the circles are outliers. The number of analyzed couples was 79 for graphene and 97 for glass from two independent cultures.

Thus, our data indicate that MTs are closer and straighter on graphene than on the control substrate. This can be easily explained by the electrostatic interaction experienced by axons on graphene as discussed in the previous section, which may increase their adhesion to the substrate, finally changing their three-dimensional architecture and forcing them to remain straighter than on the control substrate. Despite this, the TEM and STORM results suggest that the interaction between graphene and neurons does not alter the axonal ultrastructure, maintaining a similar total number and integrity of MTs and actin organization, but rather confers to axons an elongated, stretched morphology. This effect may also provide another cause for the observed stall of NGF signaling endosomes (Fig. 4.18). Indeed, transient radial expansions of axonal diameter were recently described to facilitate the processivity of the long-range fast-moving retrograde carriers at the expense of the pausing ones [197]. Accordingly, the inhibition of these expansions prompted by graphene interface (Fig. 4.30), along with the reduced MT interdistance (Fig. 4.32), may create a crowded space that might inhibit cargo mobility and reduce the retrograde transport of NGF-loaded endosomes, ultimately favoring their local action on axon outgrowth.

4.8 Conclusion

The real possibility of using graphene for neuroregeneration applications will depend on our understanding of how the interaction with graphene influences the processes of neurite outgrowth, elongation and regeneration following injury. This can be achieved by exploiting graphene optical transparency to monitor the processes of interest, as we propose to do in this work. We performed single-molecule fluorescence microscopy in living DRG neurons and revealed that, although on graphene neurons are completely viable for weeks [27], deep nanoscale changes characterize the early cell-material interaction. Indeed, in early developing peripheral neurons we observe a 8.5-fold reduction of retrogradely transported vesicles of NGF, the signaling molecule known to mediate sensory axon development (Fig. 4.18). While this is in line with previous observations that local NGF actions account for axon elongation [185,186], our experiments provide a clear, unprecedented indication that such action may be driven by a local accumulation of NGF-loaded vesicles. To investigate possible causes for the observed NGF trafficking alteration, we studied graphene influence on both electrical and structural properties of axons. In the former case, we observe mutual effects: on one side neurons change graphene charge concentration, inducing a doping clearly measurable via Raman spectroscopy (Fig. 4.23); on the other side graphene hyperpolarizes the resting membrane potential, and reduces cell excitability (Fig. 4.19). It is noteworthy that this condition ensures a maximal effect of graphene on axonal length (up to >70% increase with respect to a control substrate, Fig. 4.12Fig. 4.12. **Increased axonal elongation in DRG neurons grown on graphene.** (a) Schematic representation of DRG axonal length quantified on graphene inside a microfluidic chamber. On the left, optical image of an assembled device on graphene. On the right, cartoon showing the microfluidic chamber with the SC and AC connected by microchannels. The bright field image shows axons crossing and filling the microchannels in blue. Scale bar: 50 µm. (b) Quantification of the axonal length at different DIV on glass and graphene in a microfluidic device. A significant difference was found between graphene and control according to Two-way Anova Test. (***P_substrate <0.001, ***P_DIV <0.0001, Two-way Anova). The number of measured axons was: DIV1, glass n=42, graphene n=50; DIV2, glass n=109, graphene n=101; DIV3, glass n=147, graphene n=119; In the box plots the horizontal line is the median value, boxed area extends from the 25th to 75th percentile, whiskers from the 5th to 95th percentiles, the square is the mean and the circles are outliers. and Table 2), and was previously linked to increased axon regeneration in sensory neurons [199]. On the other hand, graphene also alters axon morphology, inducing longer and straighter axonal bundles (Fig. 4.13 and Fig. 4.35) and closer and straighter MTs within each axon (Fig. 4.32).

The sum of these effects is progressively diminished with time, allowing already after 4-5 DIV to reach an excitability and axonal transport comparable to the control (Fig. 4.19 and Fig. 4.18), and stabilizing to a 17% increase in the axonal length (Fig. 4.12 and Table 2). Thus, the molecular players stalling NGF signaling endosomes are selectively switched on upon the early contact with the material. Nevertheless, it will be important in the future to establish the synergy (if any) between the electrophysiological and structural graphene effects, in order to increase our mechanistic detail of axonal growth processes and design optimal biocompatible guides to enhance them.

5 Cell viability on centimeter-scale WS_2 and graphene on a transparent substrate

This chapter focuses on evaluating cell viability on the transition metal dichalcogenide (TMD) tungsten disulphide (WS_2) grown on sapphire via CVD. After a brief introduction on the possible biomedical applications of TMD materials, a detailed comparison of both graphene and WS_2 by using AFM and Raman spectroscopy is presented. The substrates are used as culture platforms for cell adhesion investigations and for the analysis of cell viability and cellular morphometric features.

The experimental data showed in this chapter are reported in a manuscript in preparation with authors D. Convertino, N. Mishra, L. Marchetti, M. Calvello, A. Viegi, F. Fabbri, C. Coletti: ”Cell viability on centimeter-scale WS_2 and graphene on a transparent substrate”. Experiment and data analysis concerning the evaluation of the citotoxicity and differentiation of SH-SY5Y on graphene and WS_2 were performed by D. Convertino.

5.1 Introduction

Two-dimensional materials have shown superior properties as a platform for neural cell culture. In addition to graphene, another class of two-dimensional materials, known as TMD, has gained interest for their possible application in biological and/or biomedical environments [200]. Mechanically exfoliated flakes of TMDs, have been used in bioimaging, biosensing, as antimicrobial agents and to realize nanocomposites for tissue engineering applications to promote cell adhesion and improve mechanical properties of the scaffolds [201,202]. WS_2 is one of the most studied TMDs, thanks to its optical and electrical properties. Due to this increasing interest, biocompatibility and toxicity tests need to be performed. Testing different exfoliated TMDs, Teo *et al.* demonstrated that the chalcogen plays an important role in influencing the material toxicity; in particular, they demonstrated that WS_2 were much less toxic than graphene oxide, while WSe_2 showed similar toxicity [203].

Despite the increased interest, only few studies have investigated the biocompatibility of WS_2 grown via CVD. As for graphene, this approach allows obtaining full covered substrates for cell interaction investigation. WS_2 grown via CVD on SiO_2 was demonstrated to improve cell adhesion and viability [204]. Unfortunately, due to the non-transparency of the substrate, a cell staining was necessary to visualize cell morphology.

The use of a transparent substrate to grow CVD WS_2 without transfer could help cell-substrate interaction studies, thanks to the real-time observation of cell growth with a label-free approach using standard transmitted light microscopy. In the past years, the CVD approach has been used to grow WS_2 on both epitaxial graphene on SiC [63,205] and sapphire [206]. To date, no approach has allowed the growth of continuous WS_2 directly on SiC, neither a successful method for transferring large-scale WS_2 on cover slip was available within our group, thus making unfeasible the integration of WS_2 on systems already investigated in this thesis. Hence, we decided to adopt sapphire (i.e., single-crystal aluminum oxide (Al_2O_3)), a transparent substrate with a broad transmission band from UV to near-infrared. Its chemical, thermal, electrical, mechanical and optical properties make it an attractive material for a variety of applications, including semiconductor and engineering industry [207]. Thanks to its inertness to biological tissues and biocompatibility, in the past years it has been suggested for different medical application [208], including bone, dental and neural implants [209,210]. For these reasons, together with the possibility to grow 2D materials directly on it without the need to transfer it, sapphire represents an ideal substrate material for biocompatibility investigation of other 2D materials.

In this section, we use WS_2 as a platform to investigate human neuroblastoma SH-SY5Y cell interaction and compare the results with those obtained on graphene grown on sapphire.

The SH-SY5Y cell line was chosen because it is a well-established cellular model for experimental neurological studies, including metabolism, neural differentiation and neurodegenerative processes [211]. In fact the sequential treatment of these cells with retinoic acid (RA) and human brain-derived neurotrophic factor (hBDNF), causes differentiation in a neuron like phenotype with neuritic processes.

High quality full-covered WS_2 and graphene samples were grown on sapphire via CVD, and bare sapphire and culture wells were used as control substrates to test the material effect on cell viability and differentiation. We first checked the quality and homogeneity of the synthesized materials by using AFM and Raman spectroscopy. We then used the bare substrates (i.e., without polymeric coating) to culture SH-SY5Y. Cell viability was assessed in the WST-8 cell proliferation assay and cell differentiation was investigated via optical microscopy thus allowing quantification of morphometric parameters that describe the differentiation process.

5.2 Material and methods

5.2.1 Samples preparation and characterization

Few layers (FL) WS_2 was grown directly on sapphire substrate via low-pressure chemical vapor deposition process, using tungsten trioxide WO_3 (Sigma Aldrich, 99.995%) and sulfur S (Sigma Aldrich, 99.998%) as precursors. The reactor comprises a central hot-zone, where a crucible loaded with WO_3 powder and an inlet zone, where the S powder was positioned and heated by a resistive belt. S was heated at 100°C. The sulphur vapor reacts with WO_3 directly on the substrate surface at a temperature of 930 °C and at a pressure of ~5 x 10^{-2} mbar with argon as carrier gas. In order to obtain a material homogeneity over the centimeter scale the growth process is repeated twice. The first growth process allows the nucleation of micrometric WS_2 MLs meanwhile the second process homogenize the WS_2 on centimeter scale, increasing the thickness up to few layers [212].

High-quality monolayer graphene on sapphire was obtained via CVD on the c-plane of Al_2O_3(0001) substrates with a catalyst-free and single-step approach [213] in the HT-BM Aixtron reactor adopted also for the growth of graphene on SiC. Sapphire dice were cut from single c-axis, single crystal HEMCOR, double side polished sapphire (0001) wafers. Prior to growth, sapphire substrates were cleaned with acetone, isopropanol, and DI water for 5 min each, respectively, in ultra-sonicator bath. The substrates were then cleaned in piranha solution (1:3, H_2O_2 : H_2SO_4) for 15 min and then sonicated in DI water and finally dried by N_2 blow. After the cleaning steps, sapphire substrates were H_2 etched in the HT-BM Aixtron reactor at 1180˚C for 5 min in H_2 atmosphere. After the H_2-etching step, substrates were annealed at 1200˚C for 10 min in Ar atmosphere (1000 sccm). After the annealing process, the Ar (1000 sccm), H_2 (100 sccm), and CH_4 (5 sccm) mixture gas was introduced into the CVD system for 30 min at low pressure of 25 mbar to grow graphene films directly on the substrate surface. After the growth, the reactor was cooled in Ar atmosphere (1000 sccm).

The controls adopted in the experiments were sapphire dice (sonicated in acetone and isopropanol and treated with O_2 plasma for 5 min at 100W) and polystyrene 48-well plates (Corning). The dimensions of all the substrates were about 6 × 6 mm^2.

The topography of the samples as well as the graphene and WS_2 number of layers and quality were assessed by both AFM and Raman spectroscopy. Before cell culture, all substrates were sterilized by 30 min immersion in 96% ethanol and then rinsed several times with DI water.

5.2.2 Preparation of hBDNF

The hproBDNF cDNA was subcloned in the prokaryotic expression vector pET11a and the protein was expressed as recombinant protein in E. coli strain BL21(DE3), refolded from inclusion bodies and purified by using protocols adapted from previously published ones [168,169,214,215]. Briefly, BL21(DE3) E. coli were transformed with 30 ng of plasmid pET11a containing the gene of human proBDNF; bacteria were plated on Luria-Bertani (LB) agar plates supplemented with Ampicillin (Amp) and grown overnight at 37°C. Then a single colony was inoculated in 20 ml of LB supplemented with Amp and grown overnight at 37°C with shaking at 250 rpm. The day after, the inoculum was diluted 1:50 in 1L of LB + Amp and grown at 37°C at 250 rpm to reach an OD600 of about 1 before induction with 1 mM of isopropyl-b-thio-galactoside (IPTG). The proBDNF production was continued at 37°C at 250 rpm shaking. After 5 hours, bacteria were collected by centrifugation at 5000 x g for 10 min at 4°C. The bacterial pellet was first resuspended with Lysis Buffer (10 mM TRIS HCl pH 8, 1 mM EDTA and 1 mg/ml lysozyme) at 5 ml/g v/w ratio and incubated at RT for 1 h. After sonication on ice (3 cycles of 45 seconds on and 60 seconds off using a MicrosonTM Ultrasonic Cell Disruptor XL at maximum power), 3 mM $MgCl_2$ and 50 ug/ml DNaseI solutions were added and the sample was incubated at RT for 30 minutes. To isolate inclusion bodies (IB), 0.5 vol. of Triton Buffer (60 mM EDTA, 1.5 M NaCl, 6% Triton X-100) was added and the sample and incubated at RT for 30 minutes on a stirring plate. The IB were then centrifuged at 18,000 x g for 30 minutes at 4°C, resuspended in 20 ml of resuspension buffer (10 mM TRIS HCl pH 8, 1 mM EDTA), 0.5 vol. of Triton Buffer and incubated at RT for 30 minutes on a stirring plate. The IB were then centrifuged at 18000 x g for 30 minutes at 4°C and subsequently washed three times with a total volume of 100 ml of Washing Buffer (50 mM TRIS HCl pH 7.5, 1 mM EDTA). The IB pellet was then resuspended with 5 ml/g of Solubilization Buffer (6M guanidinium, 100 mM TRIS HCl pH 8, 1 mM EDTA and 100 mM DTT), and incubated until complete solubilization at RT on a rocking plate. Then the pH was lowered to 3.5 with HCl 3M and the sample was centrifuged at 18000 x g for 30 minutes at 4°C. The resulting solution was dialyzed three times against 300 ml of Dialysis Buffer (6M guanidinium pH 3.5) each one for twelve hours using Visking dialysis membrane (cut-off 7 kDa, Medicell Membranes Ltd) and the protein concentration was measured with the Bio-Rad Protein Assay. IB solution containing denatured hproBDNF was refolded by a drop by drop addition in 100 ml of Refolding buffer (1 M Arginin, 100 mM TRIS HCl pH 9.3, 5 mM EDTA pH 8, 1mM GSSG and 5 mM GSH). Every hour 50 µg/ml of sample were added to the buffer under vigorous stirring at 4 °C. After 16-48 hours the sample was dialyzed at 4 °C using a Visking dialysis membrane (cut-off 12-14 kDa, Medicell Membranes Ltd) against 2 L of IEX-A (50 mM Na phosphate pH 7, 1 mM EDTA) replacing the buffer after 12 hours. The dialyzed sample containing proBDNF was filtered using a 0.22 µm filter and purified by FPLC. The sample was loaded on a HiLoad 16/10 SP Sepharose High Performance (~20 ml - GE Healthcare) equilibrated with IEX-A buffer using a liquid chromatography system (ÄKTA™ - FPLC). The protein was eluted with linear gradient from 0 to 100% of IEX-B (50 mM Na phosphate pH 7, 1 mM EDTA and 1M NaCl) at 1ml/min flow in 6 column volume (CV) and 2ml fractions collected. The ones corresponding to the UV (280nm) FPLC peak containing hproBDNF were pooled and dialyzed against 100 mM Hepes pH 7.5, 1 mM $CaCl_2$. The mature hBDNF protein was obtained from the purified hproBDNF after digestion with previously prepared His-tagged human furin (1µg enzyme : 20 µg of propeptide), at 30 °C for 2 h. The expression and purification of recombinant His-tagged human furin is reported below.

The hBDNF was purified by ion exchange chromatography with the same protocol used for the prohBDNF already described. The fractions collected were pooled and dialyzed against 1 L of Storage buffer (50 mM Na phosphate pH 7, 1 mM EDTA and 150 mM NaCl) for 16 hours at 4 °C. The dialyzed protein was concentrated up to 1mg/ml using an Amicon ultrafiltration membrane with 10 kDa cut-off (Merck-Millipore) and stored at - 80 °C. The purity and the correct molecular weight of the protein was monitored by SDS-PAGE and MS analyses.

5.2.3 Expression and purification of recombinant His-tagged human furin

The expression plasmid was provided by Sven Dahms and the expression procedure adapted from ref. [216,217]. Briefly, the coding sequence of human pro-furin, covering the amino acids 23-574, was inserted into the plasmid pHLsec. Using the restriction site AgeI, the insert was placed downstream to a secretion signal sequence encoded by the expression vector. The native protein sequence was modified with a Thrombin cleavage site and a His-tag, resulting in the artificial C-terminus SGSLVPRGSHHHHHH that is expressed after Ala574 [216,217]. Transfection and expression were performed in HEK293 cells.

HEK293 cells were maintained in a humidified atmosphere at 37°C, 5% CO_2 in Dulbecco's Modified Eagle's medium (DMEM high glucose, Gibco) supplemented with L-glutamine (Euroclone), non-essential amino-acids (Gibco), 10% FBS (Euroclone) and 1% penicillin/streptomycin (Euroclone). Transfection was performed with Lipofectamine® 2000 at the ratio (w/v) of plasmid-DNA to transfection reagent 1:5 (8.4 mg of plasmid-DNA and 42 ml of transfection reagent in 10-cm tissue culture dish). Transfection was carried out at approx. 80-90% confluence of the culture. The transfection medium was replaced after 4-5 h, lowering the serum concentration to 0.2%. Conditioned medium was harvested 72 h and 120 h post transfection. 12 ml and 8 ml medium were used during the first and second culture period, respectively. The conditioned samples were centrifuged (20 min, 4500 g, 20°C), filtered using a PES membrane (0.22 mm pore size, Sarstedt) and stored at -20°C. Prior to purification the samples were thawed in ice, pooled and dialysed against a 20-fold excess of 25 mM Tris, pH 8,0, 250 mM NaCl, 5 mM $CaCl_2$ with Visking dialysis membrane (cut-off 12-14 kDa, Medicell Membranes Ltd) for 16 h at 4°C. His-tagged human furin was purified by affinity chromatography, using an ÄKTApurifier 100 FPLC system (GE Healthcare) with a 1 ml HisTrap FF Crude (GE-Healthcare) affinity column. Before purification, imidazole was added to the resulting samples, up to a concentration of 10 mM. The column was then washed with 10 column volumes (CV) of buffer A (100 mM Tris, pH 8.0, 500 mM NaCl, 5 mM $CaCl_2$) supplemented with 10 mM imidazole. The protein was eluted with a linear gradient from 2 to 100% of buffer B (buffer A + 500 mM imidazole) at 1ml/min flow in 20 CV and 2ml fractions collected. The ones corresponding to the UV (280nm) FPLC peak were pooled and dialyzed against 10 mM Hepes, pH 7,5, 100 mM NaCl, 2 mM $CaCl_2$ and then concentrated to 1 mg/ml, using an Amicon ultrafiltration membrane with 10 kDa cut-off (Merck-

Millipore). The enrichment and the purity of the protein were monitored by SDS-PAGE analysis.

5.2.4 SH-SY5Y cell culture and differentiation

Human neuroblastoma SH-SY5Y cells (a kind gift of Prof. M. Canossa, University of Trento) were maintained in a humidified atmosphere at 37 °C, 5% CO_2 in high glucose Dulbecco's modified eagle medium with nutrient mixture F12 (DMEM-F12) supplemented with 10% FBS and 1% penicillin/streptomycin (Gibco). Cell were plated at ~40–60% confluency onto the bare substrates. Differentiation was achieved using the following procedure: after 24h from the seeding the cells were treated with 10 µM RA in high glucose DMEM-F12 supplemented with 1% penicillin/streptomycin and 10% of FBS for 5 days and then with hBDNF 100 ng/ml. Every 2-3 days, 2/3 of the medium was renewed.

The cells were observed at different time points using an inverted microscope equipped with a 20× magnification objective (Leica DMI4000B microscope). Typically, 10 fields per sample were acquired to perform morphometric analysis of SH-SY5Y differentiation. Three morphometric parameters were measured as previously reported in Marchetti *et al.* [150] and in section 3.1.4. Differently from [150] we quantified the mean neurite length measuring all the neurites of each differentiated cell in the field. Cell viability was assessed with the Cell counting Kit-8 assay (Dojindo), based on quantification of WST-8 reduction due to the metabolic activity of viable cells. Samples were prepared according to the manufacturer’s instructions and measured at the GloMax Discover multiplate reader (Promega). The results are reported as % over the polystyrene well, considered as control. All the experiments were repeated at least twice independently.

5.2.5 Statistical analysis

For all the experiments, we performed two independent cultures with three to five biological replicates each. For length measurement and neurite number quantification, for each substrate we analyzed at least 80 cells from selected fields of the replicates obtained with a 20× objective. The number of cells analyzed (nc) is the total pool of the experiments. The number of analyzed cells was: DIV7, G n=176, Sapphire n=205, WS_2 n=135, Well n=226; DIV9, G n=,116, Sapphire n=81, WS_2 n=98, Well n=93.At least 50 cells per fields were used for evaluating the percentage of differentiated cells. The number of analyzed cells was: DIV7, G n=1872, Sapphire n=1579, WS_2 n=2368, Well n=1964; DIV9, G n=1743, Sapphire n=1970, WS_2 n=2693, Well n=2484. All data are expressed as mean ± s.e.m. unless stated otherwise. Data were analyzed by using Origin Software. ANOVA with Bonferroni multiple comparison test, with $*p < 0.05$, $**p < 0.01$, and $***p < 0.001$.

5.3 Characterization of the few-layers WS_2

In order to identify the thickness of the CVD-grown WS_2 we adopted Raman spectroscopy. A representative Raman spectrum of WS_2 FL is presented in Fig. 5.1(a). The Raman modes of WS_2 appear at 178 cm^{-1} (LA(M) mode), 354 cm-1 (superimposed 2LA(M) and $E^1_{2g}(\Gamma)$ modes) and 418.6 cm^{-1} ($A_{1g}(\Gamma)$ mode). It is worth noting that when a 532 nm laser is employed, there is the superimposition of the 2LA (second-order Raman resonance involving the longitudinal acoustic mode (LA)) mode with the E_{2g} Raman modes, so it is not possible to assess WS_2 thickness using the separation of the E_{2g} and A_{1g} modes. Another possible benchmarking method to determine WS_2 thickness is that of looking at the Raman shift of the $A_{1g}(\Gamma)$ peak. For WS_2 monolayer the $A_{1g}(\Gamma)$ peak occurs at 417 cm^{-1} while its shift toward higher values is indicative of few-layer WS_2 (i.e., 420 cm^{-1} is the average value for bulk WS_2) [218]. The position of the $A_{1g}(\Gamma)$ in our samples is found at 418.5 cm^{-1}, which suggests WS_2 bilayer [218].

WS_2 photoluminescence (PL) intensity and position can be also used to further confirm the material thickness. In our analysis, reported in Fig. 5.1(b), the PL spectrum shows a broad, faint peak at 630 nm (1.97 eV). The standard PL emission of WS_2 monolayer on insulating substrates is a sharp intense peak at 618 nm (2.00 eV). In few layers WS_2 case, the PL intensity drastically decreases and the peak position red-shifts up to 630 nm (1.97 eV) [219]. Therefore, this additional analysis supports our initial assessment of a bilayer thickness.

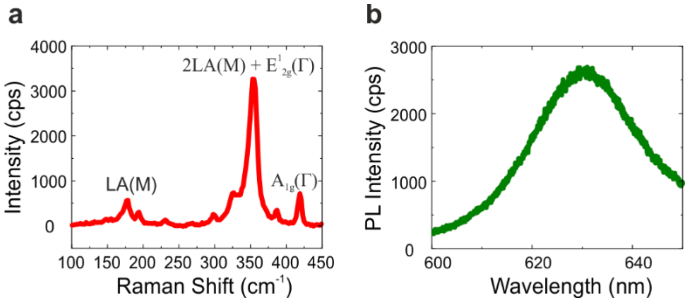

Fig. 5.1**. Representative Raman (a) and PL (b) spectrum of few-layers WS_2.**

To better evaluate material homogeneity, we carried out Raman and PL mapping. Fig. 5.2(a) shows $A_{1g}(\Gamma)$ mode Raman shift, which is consistently found to be at an average position of 418.5 cm^{-1} with a FWHM of 0.3 cm^{-1}. However, in some areas with lateral length of about 1 micrometer, the $A_{1g}(\Gamma)$

mode is locally peaked at 419 cm^{-1}, suggesting the presence of 3-layers patches.

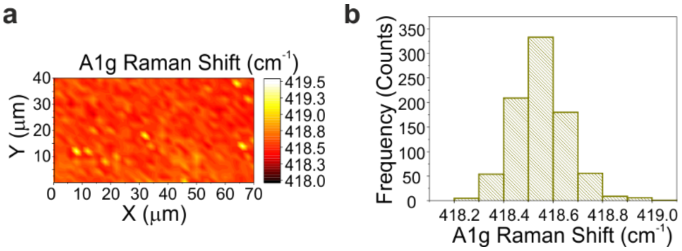

Fig. 5.2. **Raman characterization of the few-layers WS$_2$.** Map of the Raman shift of the A1g mode (a) and its statistical representation (b).

The presence of these trilayer patches is also confirmed by AFM analysis as visible in Fig. 5.3. The line profile insert in panel (b) shows that the height of these features is compatible to that of an additional WS$_2$ layer (i.e., 0.7 nm). The overall RMS of WS$_2$ FL free of the aforementioned patches is 0.2 nm, further confirming the material homogeneity.

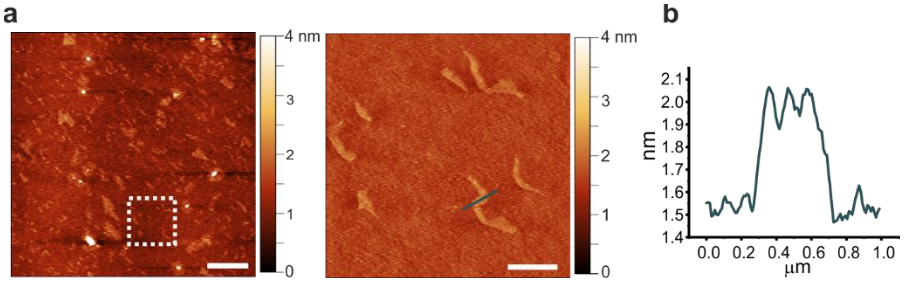

Fig. 5.3. **Morphological characterization of the few-layers WS$_2$.** (a) Large area AFM topological map of few-layers WS$_2$. Scale bar: 5 µm. The dashed white square indicates the zoomed area reported in the right panel. Scale bar: 1 µm. (b) Profile analysis of a trilayer patch.

5.4 Characterization of polycrystalline graphene on sapphire

The morphology of the graphene grown on sapphire is shown in Fig. 5.4. In the AFM micrograph are well visible the atomic terraces of the sapphire substrate as well as the graphene ridges (3-4 nm high) which are due to different thermal expansion coefficient of graphene and sapphire [62].

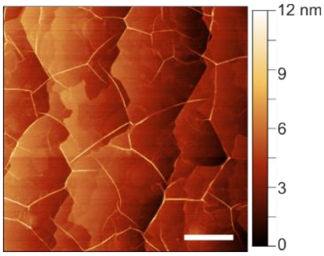

Fig. 5.4. **AFM topological map polycrystalline graphene on sapphire.** Scale bar 500 nm.

A representative Raman spectrum of graphene grown on sapphire is reported in **Error! Reference source not found.**.

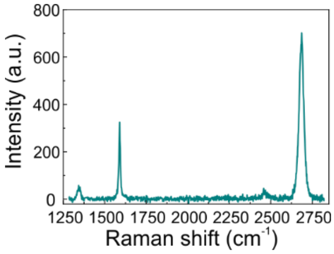

Fig. 5.5. Representative Raman spectrum of polycrystalline graphene grown on sapphire.

The standard graphene Raman G and 2D appears at 1589 cm^{-1}, and at 2684 cm^{-1}. Due to the polycrystalline nature of the graphene obtained on sapphire, also the defects- activated D mode appear at 1345 cm^{-1} [213]. We adopt the

FWHM of the 2D peak for evaluating the quality graphene on sapphire and compare it with that observed for the graphene adopted in the other chapters of this work (i.e., graphene on SiC and polycrystalline graphene on copper). The map regarding this figures of merit is reported in **Error! Reference source not found.**(a), with the relative statistical analysis presented as histogram in panel (b). The 2D FWHM histogram (**Error! Reference source not found.**(b)) shows an average value of 35 cm^{-1}, a value comparable to those found for epitaxial graphene on SiC (section 2.3) and polycrystalline graphene (section 2.4).

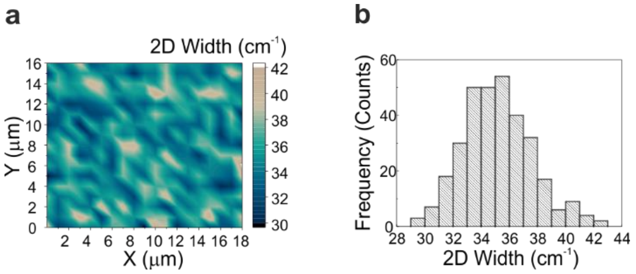

Fig. 5.6. **Raman characterization of polycrystalline graphene on sapphire**. Raman maps of the 2D mode width (a) and its statistical representation (b).

5.5 Cytotoxicity and differentiation of SH-SY5Y on graphene and WS$_2$

We investigated the cytotoxicity of graphene and WS$_2$ on sapphire morphological observation of differentiated SH-SY5Y and WST-8 viability assay. At day 3 of differentiation with hBDNF there were no morphological differences between the different substrates, cells were characterized by neural morphology with significant neurite outgrowth (Fig. 5.7).

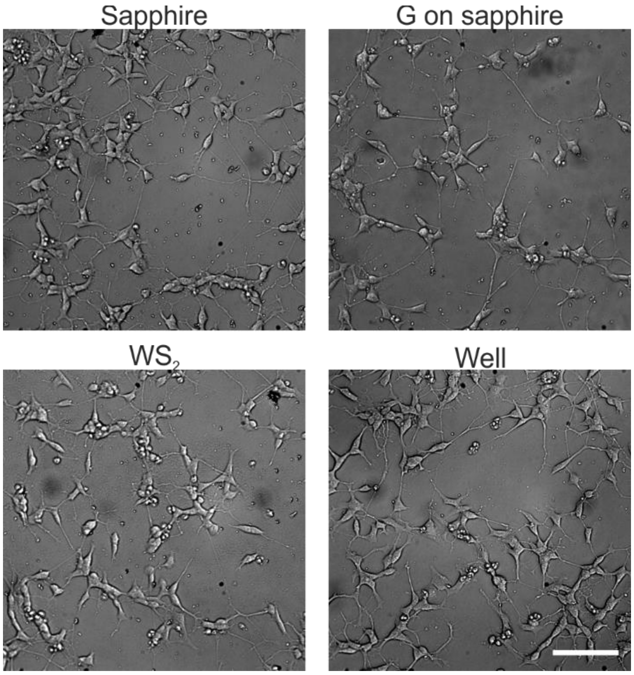

Fig. 5.7. **SH-SY5Y cells cultured on bare WS_2, bare graphene grown on sapphire and control substrates.** Typical optical microimages of SH-SY5Y cells grown on sapphire, graphene on sapphire (G on sapphire), WS_2 and polystyrene (well) at day 9, after 3 days of hBDNF treatment. Scale bar: 100 µm.

The cell viability was assessed at three different time points: at DIV5 (the last day of RA treatment before hBDNF treatment), DIV9 (3 days of hBDNF treatment) and DIV12 (6 days of hBDNF treatment) (Fig. 5.8).

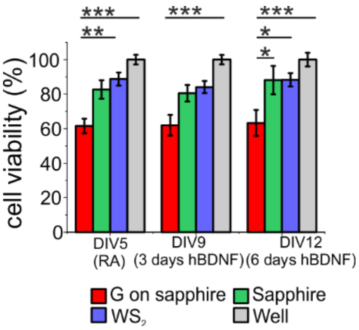

Fig. 5.8. **SH-SY5Y cells viability.** Cell viability after 5, 9, and 12 days tested by WST-8. The results are reported as mean ± s.e.m. of the % over the polystyrene control sample (*p<0.05, **p<0.01, ***p<0.0001, Two-way Anova, with Bonferroni’s Multiple Comparison Test).

As previously reported we had a good adhesion on sapphire, even in the absence of a coating [209]. We did not observe significant differences of cell viability between WS_2, sapphire and the control; on the contrary a significantly reduced viability was observed for graphene with respect to the control well (***$p<0.001$), sapphire (DIV12: *$p<0.05$) and WS_2. (DIV5: **$p<0.01$; DIV12: *$p<0.05$). This is probably due to the high hydrophobicity of the substrate that in the absence of coating reduces cell adhesion and thus the WST-8 signal [45].

Hence, we performed tailored experiments to evaluate the coating effect on cell viability (Fig. 5.9). Cell were plated at ∼40–60% confluency onto the substrates previously coated with 100 µg/ml collagen type I solution in water (C3867 Sigma-Aldrich) for 4 h at 37 °C, and then washed two times in DI water. Bare sapphire substrates and wells (the same used in the morphological quantification) were used for comparison. Cell viability after 5, 9, and 12 days, corresponding at 1 day treatment with RA, 3 days treatment with hBDNF and 6 days treatment with hBDNF was tested by WST-8. No statistically significant differences were observed between bare and coated substrates of each type. Thus, we excluded the lack of coating as the cause for the reduced viability of cells grown on graphene.

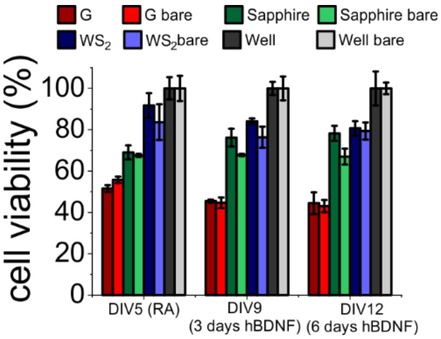

Fig. 5.9. **Cell viability on bare and coated substrates.** Cell viability after 5, 9, and 12 days tested by WST-8. The results are reported as % over the polystyrene control sample. Data reported as mean ±

s.e.m. The cell viability on bare and coated substrates did not significantly differ, according to Two-way Anova, with Bonferroni's Multiple Comparison Test.

The morphometric analysis of the differentiation process was performed at day 1 and day3 of hBDNF treatment. We quantified three morphometric parameters reported in (a-c): the percentage of differentiated cells in each field (Diff), the average neurites number per cell (av. Neurites/cell) and the average length of the neurites per differentiated cell (length). Graphene induced significantly greater differentiation relative to the control well, both after one (***p<0.001) and three (**p<0.01) days of hBDNF treatment (Fig. 5.10(a)). It performed also better than sapphire and WS_2 both after one (*p<0.05) and three days (***p<0.001).

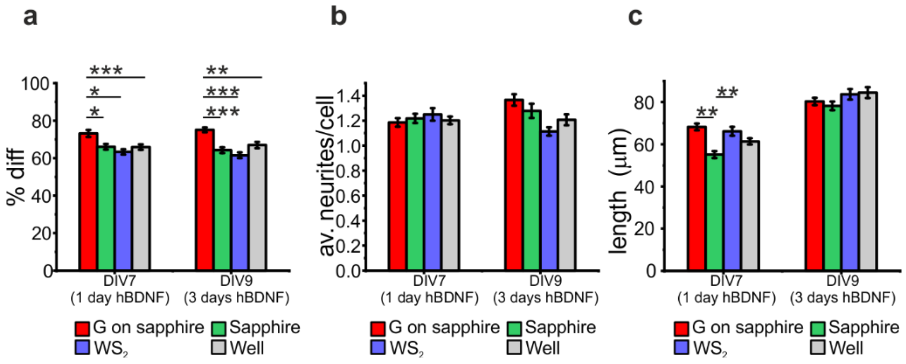

Fig. 5.10. **Morphometric analysis of SH-SY5Y cells.** Histograms shows (a) quantification of the percentage of differentiation, (b) average number of neurites per cell and (c) neurite length at different DIV of two independent experiments per substrate. Data reported as mean ± s.e.m. (*p<0.05, **p<0.01, ***p<0.0001, Two-way Anova, with Bonferroni's Multiple Comparison Test).

Remarkably, after one day the percentage of differentiated cells was higher than on WS_2, sapphire and well by 11, 16 and 11%, respectively, reaching an increase in the percentage of 17, 22, 12% after three days of hBDNF, while the average number of neurites per cell on graphene and WS_2 was comparable to that of the controls (Fig. 5.10(b)). We evaluated the mean neurite length at day 1 and day3 of hBDNF treatment. Following this time, the formation of a highly dense network impeded further quantification. Interestingly, after one day of differentiation the mean neurite length on graphene was significantly higher than on sapphire (***$p<0.001$) and control well (*$p<0.05$) by 24% and 11%, respectively. Also WS_2 showed significantly 20% longer neurite compared to sapphire (***$p<0.001$). After 3 days of hBDNF treatment, the neurite length was comparable to the control (Fig. 5.10(c)).

These results confirm the positive effect of graphene on cell differentiation and neurite outgrowth, previously reported in this thesis for different cell lines, and in other works [11,31,45]. The reduced percentage of length increase observed on graphene in Fig. 5.10(c) with respect to the one showed in Fig. 3.11(a), could be explained by the different type of graphene used in this study. The graphene on sapphire is polycrystalline with a reduced crystal dimension of hundreds of nanometers [213]. Epitaxial graphene on SiC is highly crystalline, while the single-crystal size for CVD graphene on Cu is larger than that of a single cell. The surface topography, characterized by terraces and nanometric wrinkles has an increased roughness compared with graphene on SiC. This could change the cell response to the materials, indeed cells are known to be sensitive to nanoscale roughness actively responding to surface nanotopography, as previously reported for other materials [220–222]. Moreover, it was previously demonstrated that graphene crystallinity influenced its cytocompatibility in terms of neuronal attachment and outgrowth, tuning the neural affinity from adhesive to repellent [86]. This consideration could explain the reduced cell viability obtained on graphene, with respect to the other substrates.

On the contrary, WS_2 showed a very good cell viability, comparable with the one of the control well. Interestingly, it induced a neurite sprouting comparable to graphene, confirming its potential in biomedical application and interactions with neural cells.

5.6 Conclusion

This chapter provides novel data about the use of large-scale graphene and WS_2 grown via CVD on a transparent biocompatible substrate such as sapphire. We used SH-SY5Y cells, as a consolidated model for neurobiology studies to examine the substrate effect on cell morphology and viability. Interestingly, WS_2 was an excellent substrate for culturing SH-SY5Y cells, showing an increased neurite length and a viability comparable to the controls. Graphene confirmed its capacity to induce cell differentiation and neurite sprouting, performing better than controls, even if its performances in terms of viability were strongly influenced by its roughness and crystallinity.

Conclusion and outlook

Due to an enticing set of properties, graphene and other 2D materials are bringing new perspectives in the field of innovative medicine, especially for application in regenerative medicine.

This thesis represents a pioneering work which helps to move towards a better understanding of the impact of graphene on peripheral neurons. We show a positive effect of graphene in terms of axonal outgrowth and study the molecular mechanism driving this axon elongation in a time-dependent fashion. We report for the first time structural and dynamic information on the material effect on neuron physiology in the early developmental stage, key information towards the development of graphene-based devices for peripheral neurons regeneration.

Graphene per se confirms its potential as an active substrate that enhances axonal outgrowth. Knowing the potential of microfluidic platforms in axonal injury studies, the next step will be to perform the structural and transport experiments after a selective axotomy to quantify axonal regeneration in response to graphene. Moreover, graphene conductivity could be further exploited in neuron regeneration by adding an external electrical stimulation, which shall additionally enhance graphene positive effect on axonal elongation. To this end, different parameters (*e.g.* stimulation frequency, intensity, duration and temporal pattern) will need to be systematically tested to ultimately identify those that effectively improve the regeneration process. To further proceed in this direction, a neural stimulation device directly integrated in the compartmentalized chambers shall be developed.

The use of large-scale CVD graphene, flexible and potentially transferable on substrates of choice, may serve as a basis for the design of implants for in vivo applications. The integration of graphene with commercially available polymeric conduits adopted in neural regeneration shall ultimately improve their electrical conductivity (which is functional to implement stimulation), while preserving the biocompatibility and mechanical properties of the polymer that fit well with the nerve tissues.

Another exciting future development which could stem from the work reported in this thesis is the use of graphene/WS_2 heterostructures in regenerative applications. As graphene/WS_2 has proved to be an excellent platform for implementing optically-induced charge transfer [63], this heterostack could be exploited to realize novel advanced nerve conduits for a non-invasive optically-stimulated axon regeneration, where electrical stimulation could be operated thanks to the photoinduced current in graphene.

Bibliography

1. Faroni, A., Mobasseri, S. A., Kingham, P. J. & Reid, A. J. Peripheral nerve regeneration: Experimental strategies and future perspectives. *Adv. Drug Deliv. Rev.* **82**, 160–167 (2015).

2. Daly, W., Yao, L., Zeugolis, D., Windebank, A. & Pandit, A. A biomaterials approach to peripheral nerve regeneration: bridging the peripheral nerve gap and enhancing functional recovery. *J. R. Soc. Interface* **9**, 202–221 (2012).

3. Gu, X., Ding, F. & Williams, D. F. Neural tissue engineering options for peripheral nerve regeneration. *Biomaterials* **35**, 6143–6156 (2014).

4. Tran, P. A., Zhang, L. & Webster, T. J. Carbon nanofibers and carbon nanotubes in regenerative medicine. *Adv. Drug Deliv. Rev.* **61**, 1097–1114 (2009).

5. Fraczek-Szczypta, A. Carbon nanomaterials for nerve tissue stimulation and regeneration. *Mater. Sci. Eng. C* **34**, 35–49 (2014).

6. Pinho, A. C., Fonseca, A. C., Serra, A. C., Santos, J. D. & Coelho, J. F. J. Peripheral Nerve Regeneration : Current Status and New Strategies Using Polymeric Materials. *Adv. Healthc. Mater.* **5**, 2732–2744 (2016).

7. Novoselov, K. S. *et al.* Electric Field Effect in Atomically Thin Carbon Films. *Science* **306**, 666–669 (2004).

8. Lee, C., Wei, X., Kysar, J. W. & Hone, J. Measurement of the Elastic Properties and Intrinsic Strength of Monolayer Graphene. *Science* **321**, 385–388 (2008).

9. Castro Neto, A. H., Guinea, F., Peres, N. M. R., Novoselov, K. S. &

Geim, A. K. The electronic properties of graphene. *Rev. Mod. Phys.* **81**, 109–162 (2009).

10. Bitounis, D., Ali-Boucetta, H., Hong, B. H., Min, D. H. & Kostarelos, K. Prospects and challenges of graphene in biomedical applications. *Adv. Mater.* **25**, 2258–2268 (2013).

11. Li, N. *et al.* The promotion of neurite sprouting and outgrowth of mouse hippocampal cells in culture by graphene substrates. *Biomaterials* **32**, 9374–9382 (2011).

12. Hong, S. W. *et al.* Enhanced neural cell adhesion and neurite outgrowth on graphene-based biomimetic substrates. *Biomed Res. Int.* **2014**, (2014).

13. Meng, S. Nerve cell differentiation using constant and programmed electrical stimulation through conductive non-functional graphene nanosheets film. *Tissue Eng. Regen. Med.* **11**, 274–283 (2014).

14. Park, S. Y. *et al.* Enhanced differentiation of human neural stem cells into neurons on graphene. *Adv. Mater.* **23**, 263–267 (2011).

15. Frahs, S. M. *et al.* Prechondrogenic ATDC5 Cell Attachment and Differentiation on Graphene Foam; Modulation by Surface Functionalization with Fibronectin. *ACS Appl. Mater. Interfaces* **11**, 41906–41924 (2019).

16. Jakus, A. E. *et al.* Three-dimensional printing of high-content graphene scaffolds for electronic and biomedical applications. *ACS Nano* **9**, 4636–4648 (2015).

17. Liu, X. *et al.* Functionalized Carbon Nanotube and Graphene Oxide Embedded Electrically Conductive Hydrogel Synergistically

Stimulates Nerve Cell Differentiation. *ACS Appl. Mater. Interfaces* **9**, 14677–14690 (2017).

18. Qian, Y. *et al.* An integrated multi-layer 3D-fabrication of PDA/RGD coated graphene loaded PCL nanoscaffold for peripheral nerve restoration. *Nat. Commun.* **9**, (2018).

19. Agarwal, S. *et al.* Interfacing live cells with nanocarbon substrates. *Langmuir* **26**, 2244–2247 (2010).

20. Bramini, M. *et al.* Graphene Oxide Nanosheets Disrupt Lipid Composition, Ca 2+ Homeostasis, and Synaptic Transmission in Primary Cortical Neurons. *ACS Nano* **10**, 7154–7171 (2016).

21. Defterali, C. *et al.* In Vitro evaluation of Biocompatibility of Uncoated Thermally reduced graphene and carbon nanotube-loaded PVDF Membranes with adult neural stem cell-Derived neurons and glia. *Front. Bioeng. Biotechnol.* **4**, 1–19 (2016).

22. Fabbro, A. *et al.* Graphene-Based interfaces do not alter target nerve cells. *ACS Nano* **10**, 615–623 (2016).

23. Rauti, R. *et al.* Graphene Oxide Nanosheets Reshape Synaptic Function in Cultured Brain Networks. *ACS Nano* **10**, 4459–4471 (2016).

24. Chiacchiaretta, M. *et al.* Graphene Oxide Upregulates the Homeostatic Functions of Primary Astrocytes and Modulates Astrocyte-to-Neuron Communication. *Nano Lett.* **18**, 5827–5838 (2018).

25. Schmidt, C. E., Shastri, V. R., Vacanti, J. P. & Langer, R. Stimulation of neurite outgrowth using an electrically conducting polymer. *Proc. Natl. Acad. Sci. U. S. A.* **94**, 8948–8953 (1997).

26. Deng, M. *et al.* Electrochemical deposition of polypyrrole/graphene

oxide composite on microelectrodes towards tuning the electrochemical properties of neural probes. *Sensors Actuators, B Chem.* **158**, 176–184 (2011).

27. Pampaloni, N. P. *et al.* Single-layer graphene modulates neuronal communication and augments membrane ion currents. *Nat. Nanotechnol.* **13**, 755–764 (2018).

28. Kuzum, D. *et al.* Transparent and flexible low noise graphene electrodes for simultaneous electrophysiology and neuroimaging. *Nat. Commun.* **5**, 1–10 (2014).

29. Park, D. W. *et al.* Graphene-based carbon-layered electrode array technology for neural imaging and optogenetic applications. *Nat. Commun.* **5**, 1–11 (2014).

30. Hébert, C. *et al.* Flexible Graphene Solution-Gated Field-Effect Transistors: Efficient Transducers for Micro-Electrocorticography. *Adv. Funct. Mater.* **28**, 1–15 (2018).

31. Lee, J. H. *et al.* Enhanced neurite outgrowth of PC-12 cells on graphene-monolayer-coated substrates as biomimetic cues. *J. Korean Phys. Soc.* **61**, 1696–1699 (2012).

32. Sun, Y. *et al.* Surface Coating as a Key Parameter in Engineering Neuronal Network Structures In Vitro. *Biointerphases* **7**, 29 (2012).

33. Ku, S. H., Lee, M. & Park, C. B. Carbon-Based Nanomaterials for Tissue Engineering. *Adv. Healthc. Mater.* **2**, 244–260 (2013).

34. Ding, X., Liu, H. & Fan, Y. Graphene-Based Materials in Regenerative Medicine. *Adv. Healthc. Mater.* **4**, 1451–1468 (2015).

35. Wang, L. *et al.* Silk-Graphene Hybrid Hydrogels with Multiple Cues to

Induce Nerve Cell Behavior. *ACS Biomater. Sci. Eng.* **5**, 613–622 (2019).

36. Uesaka, N., Hirai, S., Maruyama, T., Ruthazer, E. & Nobuhiko, Y. Activity Dependence of Cortical Axon Branch Formation: A Morphological and Electrophysiological Study Using Organotypic Slice Cultures. *J. Neurosci.* **25**, 1–9 (2005).

37. Singh, B. *et al.* Accelerated axon outgrowth, guidance, and target reinnervation across nerve transection gaps following a brief electrical stimulation paradigm: Laboratory investigation. *J. Neurosurg.* **116**, 498–512 (2012).

38. Bourke, J. L., Coleman, H. A., Pham, V., Forsythe, J. S. & Parkington, H. C. Neuronal Electrophysiological Function and Control of Neurite Outgrowth on Electrospun Polymer Nanofibers Are Cell Type Dependent. *Tissue Eng. Part A* **20**, 1089–1095 (2013).

39. Lee, J. Y., Bashur, C. A., Gomez, N., Goldstein, A. S. & Schmidt, C. E. Enhanced polarization of embryonic hippocampal neurons on micron scale electrospun fibers. *J. Biomed. Mater. Res. - Part A* **92**, 1398–1406 (2010).

40. Emtsev, K. V. *et al.* Towards wafer-size graphene layers by atmospheric pressure graphitization of silicon carbide. *Nat. Mater.* **8**, 203–207 (2009).

41. Li, X. *et al.* Large area synthesis of high quality and uniform graphene films on copper foils. *Science* **324**, 1312–1314 (2009).

42. Greene, L. A. & Tischler, A. S. Establishment of a noradrenergic clonal line of rat adrenal pheochromocytoma cells which respond to nerve

growth factor. *Proc. Natl. Acad. Sci. U. S. A.* **73**, 2424–8 (1976).

43. Neumann, S. & Woolf, C. J. Regeneration of Dorsal Column Fibers into and beyond the Lesion Site following Adult Spinal Cord Injury. *Neuron* **23**, 83–91 (1999).

44. Convertino, D., Rossi, A., Miseikis, V., Piazza, V. & Coletti, C. Thermal decomposition and chemical vapor deposition: a comparative study of multi-layer growth of graphene on SiC(000-1). *MRS Adv.* **1**, 3667–3672 (2016).

45. Convertino, D., Luin, S., Marchetti, L. & Coletti, C. Peripheral neuron survival and outgrowth on graphene. *Front. Neurosci.* **12**, 1–8 (2018).

46. Snider, W. D. Dorsal root ganglion neurons require functional neurotrophin receptors for survival during development. *Philos. Trans. R. Soc. B Biol. Sci.* **351**, 395–403 (1996).

47. Lentz, S. I., Knudson, C. M., Korsmeyer, S. J. & Snider, W. D. Neurotrophins support the development of diverse sensory axon morphologies. *J. Neurosci.* **19**, 1038–1048 (1999).

48. Geim, A. K. & Novoselov, K. S. The rise of graphene. *Nat. Mater.* **6**, 183–191 (2007).

49. Riedl, C., Coletti, C. & Starke, U. Structural and electronic properties of epitaxial Graphene on SiC(0001): A review of growth, characterization, transfer doping and hydrogen intercalation. *J. Phys. D. Appl. Phys.* **43**, (2010).

50. NobelPrize.org. The Official Website of the Nobel Prize. On-line. https://www.nobelprize.org/prizes/physics/2010/summary/. (2010).

51. Forti, S. Large-area epitaxial graphene on SiC(0001): from decoupling

to interface engineering. (2014).

52. Balandin, A. A. Thermal properties of graphene and nanostructured carbon materials. *Nat. Mater.* **10**, 569–581 (2011).

53. Bunch, J. S. *et al.* Impermeable Atomic Membranes from Graphene Sheets. *Nano Lett.* **8**, 2458–2462 (2008).

54. Nair, R. R. *et al.* Fine Structure Constant Defines Visual Transparency of Graphene. *Science* **320**, 1308–1308 (2008).

55. Novoselov, K. S. *et al.* A roadmap for graphene. *Nature* **490**, 192–200 (2012).

56. Pinto, A. M., Gonçalves, I. C. & Magalhães, F. D. Graphene-based materials biocompatibility: A review. *Colloids Surfaces B Biointerfaces* **111**, 188–202 (2013).

57. Mashoff, T. *et al.* Increasing the active surface of titanium islands on graphene by nitrogen sputtering. *Appl. Phys. Lett.* **106**, (2015).

58. Takahashi, K. *et al.* Revealing the Multibonding State between Hydrogen and Graphene-Supported Ti Clusters. *J. Phys. Chem. C* **120**, 12974–12979 (2016).

59. Geim, A. K. Graphene: Status and Prospects. *Science* **324**, 1530–1534 (2009).

60. Kostarelos, K. & Novoselov, K. S. Graphene devices for life. *Nat. Nanotechnol.* **9**, 744–745 (2014).

61. Geim, A. K. & Grigorieva, I. V. Van der Waals heterostructures. *Nature* **499**, 419–425 (2013).

62. Mishra, N. *et al.* Rapid and catalyst-free van der Waals epitaxy of

graphene on hexagonal boron nitride. *Carbon N. Y.* **96**, 497–502 (2016).

63. Rossi, A. *et al.* Scalable synthesis of WS 2 on graphene and h-BN : an all-2D platform for light-matter transduction. *2D Mater.* **3**, 031013 (2016).

64. Feng, L. & Liu, Z. Graphene in biomedicine: opportunities and challenges. *Nanomedicine* **6**, 317–324 (2011).

65. Shen, H., Zhang, L., Liu, M. & Zhang, Z. Biomedical applications of graphene. *Theranostics* **2**, 283–294 (2012).

66. Zhang, Y., Nayak, T. R., Hong, H. & Cai, W. Graphene: A versatile nanoplatform for biomedical applications. *Nanoscale* **4**, 3833–3842 (2012).

67. Chung, C. *et al.* Biomedical applications of graphene and graphene oxide. *Acc. Chem. Res.* **46**, 2211–2224 (2013).

68. Rauti, R., Musto, M., Bosi, S., Prato, M. & Ballerini, L. Properties and behavior of carbon nanomaterials when interfacing neuronal cells: How far have we come? *Carbon N. Y.* **143**, 430–446 (2019).

69. Shin, S. R. *et al.* Graphene-based materials for tissue engineering. *Adv. Drug Deliv. Rev.* **105**, 255–274 (2016).

70. Bramini, M. *et al.* Interfacing Graphene-Based Materials With Neural Cells. *Front. Syst. Neurosci.* **12**, 1–22 (2018).

71. Kostarelos, K. & Novoselov, K. S. Exploring the Interface of Graphene and Biology. *Science* **344**, 261–263 (2014).

72. Mao, H. Y. *et al.* Graphene: Promises, Facts, Opportunities, and Challenges in Nanomedicine. *Chem. Rev.* **113**, 3407–3424 (2013).

73. Criado, A., Melchionna, M., Marchesan, S. & Prato, M. The Covalent Functionalization of Graphene on Substrates. *Angew. Chemie - Int. Ed.* **54**, 10734–10750 (2015).

74. Du, W., Jiang, X. & Zhu, L. From graphite to graphene: Direct liquid-phase exfoliation of graphite to produce single- and few-layered pristine graphene. *J. Mater. Chem. A* **1**, 10592–10606 (2013).

75. Keisham, B., Cole, A., Nguyen, P., Mehta, A. & Berry, V. Cancer Cell Hyperactivity and Membrane Dipolarity Monitoring via Raman Mapping of Interfaced Graphene: Toward Non-Invasive Cancer Diagnostics. *ACS Appl. Mater. Interfaces* **8**, 32717–32722 (2016).

76. Singh, V. K. *et al.* Fabrication of sensitive bioelectrode based on atomically thin CVD grown graphene for cancer biomarker detection. *Biosens. Bioelectron.* **105**, 173–181 (2018).

77. Pumera, M. Graphene in biosensing. *Mater. Today* **14**, 308–315 (2011).

78. Zhang, Y. *et al.* Cytotoxicity Effects of Graphene and Single-Wall Carbon Nanotubes in Neural Phaeochromocytoma-Derived PC12 Cells. *ACS Nano* **4**, 3181–3186 (2010).

79. Liao, K. H., Lin, Y. S., MacOsko, C. W. & Haynes, C. L. Cytotoxicity of graphene oxide and graphene in human erythrocytes and skin fibroblasts. *ACS Appl. Mater. Interfaces* **3**, 2607–2615 (2011).

80. Wang, K. *et al.* Biocompatibility of Graphene Oxide. *Nanoscale Res. Lett.* **6**, 1–8 (2011).

81. Yang, K., Li, Y., Tan, X., Peng, R. & Liu, Z. Behavior and toxicity of graphene and its functionalized derivatives in biological systems. *Small* **9**, 1492–1503 (2013).

82. Kuila, T. *et al.* Chemical functionalization of graphene and its applications. *Prog. Mater. Sci.* **57**, 1061–1105 (2012).

83. Sahni, D. *et al.* Biocompatibility of pristine graphene for neuronal interface. *J. Neurosurg. Pediatr.* **11**, 575–583 (2013).

84. Tang, M. *et al.* Enhancement of electrical signaling in neural networks on graphene films. *Biomaterials* **34**, 6402–6411 (2013).

85. Guo, R. *et al.* Accelerating bioelectric functional development of neural stem cells by graphene coupling : Implications for neural interfacing with conductive materials. *Biomaterials* **106**, 193–204 (2016).

86. Veliev, F., Briançon-Marjollet, A., Bouchiat, V. & Delacour, C. Impact of crystalline quality on neuronal affinity of pristine graphene. *Biomaterials* **86**, 33–41 (2016).

87. Bendali, A. *et al.* Purified Neurons can Survive on Peptide-Free Graphene Layers. *Adv. Healthc. Mater.* **2**, 929–933 (2013).

88. Golafshan, N., Kharaziha, M. & Fathi, M. Tough and conductive hybrid graphene-PVA: Alginate fibrous scaffolds for engineering neural construct. *Carbon N. Y.* **111**, 752–763 (2017).

89. Song, Q. *et al.* Anti-inflammatory effects of three-dimensional graphene foams cultured with microglial cells. *Biomaterials* **35**, 6930–6940 (2014).

90. Keefer, E. W., Botterman, B. R., Romero, M. I., Rossi, A. F. & Gross, G. W. Carbon nanotube coating improves neuronal recordings. *Nat. Nanotechnol.* **3**, 1–6 (2008).

91. Rastegar, S. *et al.* Signal-to-noise ratio enhancement using graphene-based passive microelectrode arrays. in *2017 IEEE 60th International*

Midwest Symposium on Circuits and Systems (MWSCAS) 507–510 (IEEE, 2017).

92. Thunemann, M. *et al.* Deep 2-photon imaging and artifact-free optogenetics through transparent graphene microelectrode arrays. *Nat. Commun.* **9**, 1–12 (2018).

93. Bonaccorso, F. *et al.* Production and processing of graphene and 2d crystals. *Mater. Today* **15**, 564–589 (2012).

94. Park, S. & Ruoff, R. S. Chemical methods for the production of graphenes. *Nat. Nanotechnol.* 217–224 (2009). doi:10.1038/nnano.2009.58

95. Starke, U., Forti, S., Emtsev, K. V & Coletti, C. Engineering the electronic structure of epitaxial graphene by transfer doping and atomic intercalation. *MRS Bull.* **37**, 1177–1186 (2012).

96. First, P. N. *et al.* Epitaxial Graphenes on Silicon Carbide. *MRS Bull.* **35**, 296–305 (2010).

97. Qingkai Yu *et al.* Graphene segregated on Ni surfaces and transferred to insulators. *Appl. Phys. Lett.* **93**, 113103 (2008).

98. Miseikis, V. *et al.* Rapid CVD growth of millimetre-sized single crystal graphene using a cold-wall reactor. *2D Mater.* **2**, 014006 (2015).

99. Ramachandran, V., Brady, M. F., Smith, a. R., Feenstra, R. M. & Greve, D. W. Preparation of atomically flat surfaces on silicon carbide using hydrogen etching. *J. Electron. Mater.* **27**, 308–312 (1998).

100. Riedl, C., Coletti, C., Iwasaki, T., Zakharov, A. A. & Starke, U. Quasi-free-standing epitaxial graphene on SiC obtained by hydrogen intercalation. *Phys. Rev. Lett.* **103**, 1–4 (2009).

101. Kellar, J. A., Alaboson, J. M. P., Wang, Q. H. & Hersam, M. C. Identifying and characterizing epitaxial graphene domains on partially graphitized SiC(0001) surfaces using scanning probe microscopy. *Appl. Phys. Lett.* **96**, 1–4 (2010).

102. Tamayo, J. & García, R. Deformation, Contact Time, and Phase Contrast in Tapping Mode Scanning Force Microscopy. *Langmuir* **12**, 4430–4435 (2002).

103. Kruskopf, M. *et al.* Epitaxial graphene on SiC: Modification of structural and electron transport properties by substrate pretreatment. *J. Phys. Condens. Matter* **27**, (2015).

104. Ferrari, A. C. Raman spectroscopy of graphene and graphite: Disorder, electron-phonon coupling, doping and nonadiabatic effects. *Solid State Commun.* **143**, 47–57 (2007).

105. Malard, L. M., Pimenta, M. A., Dresselhaus, G. & Dresselhaus, M. S. Raman spectroscopy in graphene. *Phys. Rep.* **473**, 51–87 (2009).

106. Lee, D. S. *et al.* Raman Spectra of Epitaxial Graphene on SiC and of Epitaxial Graphene Transferred to SiO 2. *Nano Lett.* **8**, 4320–4325 (2008).

107. Das, A., Chakraborty, B. & Sood, A. K. Raman spectroscopy of graphene on different substrates and influence of defects. *Bull. Mater. Sci.* **31**, 579–584 (2008).

108. Hao, Y. *et al.* Probing layer number and stacking order of few-layer graphene by Raman Spectroscopy. *Small* **6**, 195–200 (2010).

109. Das, A. *et al.* Monitoring dopants by Raman scattering in an electrochemically top-gated graphene transistor. *Nat. Nanotechnol.* **3**,

210–215 (2008).

110. Lee, J. E., Ahn, G., Shim, J., Lee, Y. S. & Ryu, S. Optical separation of mechanical strain from charge doping in graphene. *Nat. Commun.* **3**, 1024–1028 (2012).

111. Neumann, C. *et al.* Raman spectroscopy as probe of nanometre-scale strain variations in graphene. *Nat. Commun.* **6**, 1–7 (2015).

112. Casiraghi, C., Pisana, S., Novoselov, K. S., Geim, A. K. & Ferrari, A. C. Raman fingerprint of charged impurities in graphene. *Appl. Phys. Lett.* **91**, 1–4 (2007).

113. Röhrl, J. *et al.* Raman spectra of epitaxial graphene on SiC(0001). *Appl. Phys. Lett.* **92**, 20–23 (2008).

114. ying Wang, Y. *et al.* Raman Studies of Monolayer Graphene: The Substrate Effect. *J. Phys. Chem. C* **112**, 10637–10640 (2008).

115. Starke, U., Bernhardt, J., Schardt, J. & Heinz, K. SiC surface reconstruction: relevancy of atomic structure for growth technology. *Surf. Rev. Lett.* **06**, 1129–1141 (1999).

116. Frewin, C. L., Coletti, C., Riedl, C., Starke, U. & Saddow, S. E. A Comprehensive Study of Hydrogen Etching on the Major SiC Polytypes and Crystal Orientations. *Mater. Sci. Forum* **615**–**617**, 589–592 (2009).

117. Bianco, F. *et al.* Terahertz detection by epitaxial-graphene field-effect-transistors on silicon carbide. *Appl. Phys. Lett.* **107**, 131104 (2015).

118. Hupalo, M., Conrad, E. H. & Tringides, M. C. Growth mechanism for epitaxial graphene on vicinal 6H-SiC (0001) surfaces: A scanning tunneling microscopy study. *Phys. Rev. B - Condens. Matter Mater.*

Phys. **80**, 1–4 (2009).

119. Emtsev, K. V., Speck, F., Seyller, T., Ley, L. & Riley, J. D. Interaction, growth, and ordering of epitaxial graphene on SiC{0001} surfaces: A comparative photoelectron spectroscopy study. *Phys. Rev. B - Condens. Matter Mater. Phys.* **77**, 1–10 (2008).

120. Strupinski, W. *et al.* Graphene Epitaxy by Chemical Vapor Deposition on SiC. *Nano Lett.* **11**, 1786–1791 (2011).

121. Candini, A. *et al.* Electroburning of few-layer graphene flakes, epitaxial graphene, and turbostratic graphene discs in air and under vacuum. *Beilstein J. Nanotechnol.* **6**, 711–719 (2015).

122. Candini, A. *et al.* High Photoresponsivity in Graphene Nanoribbon Field-Effect Transistor Devices Contacted with Graphene Electrodes. *J. Phys. Chem. C* **121**, 10620–10625 (2017).

123. Haghighian, N. *et al.* Rippling of graphitic surfaces: A comparison between few-layer graphene and HOPG. *Phys. Chem. Chem. Phys.* **20**, 13322–13330 (2018).

124. Meng, F. *et al.* Saturable absorption of femtosecond optical pulses in multilayer turbostratic graphene. *Opt. Express* **24**, 15261 (2016).

125. Bianco, F. *et al.* THz saturable absorption in turbostratic multilayer graphene on silicon carbide. *Opt. Express* **23**, 11632 (2015).

126. de Heer, W. A. *et al.* Large area and structured epitaxial graphene produced by confinement controlled sublimation of silicon carbide. *Proc. Natl. Acad. Sci. U. S. A.* **108**, 16900–5 (2011).

127. Prakash, G., Capano, M. A., Bolen, M. L., Zemlyanov, D. & Reifenberger, R. G. AFM study of ridges in few-layer epitaxial

graphene grown on the carbon-face of 4H-SiC (000$\bar{1}$). *Carbon N. Y.* **48**, 2383–2393 (2010).

128. Johansson, L. I. *et al.* Stacking of adjacent graphene layers grown on C-face SiC. *Phys. Rev. B - Condens. Matter Mater. Phys.* **84**, 1–8 (2011).

129. Razado-Colambo, I. *et al.* Probing the electronic properties of graphene on C-face SiC down to single domains by nanoresolved photoelectron spectroscopies. *Phys. Rev. B - Condens. Matter Mater. Phys.* **92**, 1–10 (2015).

130. Shivaraman, S., Chandrashekhar, M. V. S., Boeckl, J. J. & Spencer, M. G. Thickness estimation of epitaxial graphene on sic using attenuation of substrate raman intensity. *J. Electron. Mater.* **38**, 725–730 (2009).

131. Faugeras, C. *et al.* Few-layer graphene on SiC, pyrolitic graphite, and graphene: A Raman scattering study. *Appl. Phys. Lett.* **92**, 2006–2009 (2008).

132. Zanotto, S. *et al.* Coherent absorption of light by graphene and other optically conducting surfaces in realistic on-substrate configurations. *APL Photonics* **2**, 016101 (2017).

133. Hibino, H. *et al.* Microscopic thickness determination of thin graphite films formed on SiC from quantized oscillation in reflectivity of low-energy electrons. *Phys. Rev. B - Condens. Matter Mater. Phys.* **77**, 1–7 (2008).

134. Chen, J. W. *et al.* Efficient n-type doping in epitaxial graphene through strong lateral orbital hybridization of Ti adsorbate. *Carbon N. Y.* **109**, 300–305 (2016).

135. Coletti, C. *et al.* Charge neutrality and band-gap tuning of epitaxial graphene on SiC by molecular doping. *Phys. Rev. B - Condens. Matter Mater. Phys.* **81**, 1–8 (2010).

136. Kang, J., Ronen, Y., Cohen, Y. & Convertino, D. MBE growth of self - assisted InAs nanowires on graphene. *Semicond. Sci. Technol.* **31**, 115005 (2016).

137. Wu, B. *et al.* Self-organized graphene crystal patterns. *NPG Asia Mater.* **5**, e36–e36 (2013).

138. Kim, H. *et al.* Activation energy paths for graphene nucleation and growth on Cu. *ACS Nano* **6**, 3614–3623 (2012).

139. Yu, Q. *et al.* Control and characterization of individual grains and grain boundaries in graphene grown by chemical vapour deposition. *Nat. Mater.* **10**, 443–449 (2011).

140. Hao, Y. *et al.* The Role of Surface Oxygen in the Growth of Large Single-Crystal Graphene on Copper. *Science* **342**, 720–723 (2013).

141. Lee, D., Ahn, G. & Ryu, S. Two-dimensional water diffusion at a graphene-silica interface. *Journal of the American Chemical Society* **136**, 6634–6642 (2014).

142. El Merhie, A. *et al.* Single layer graphene functionalized MEA for enhanced detection of neuronal network development. *Sensors Actuators, B Chem.* **277**, 224–233 (2018).

143. Greene, L. A. & Tischler, A. S. *PC12 Pheochromocytoma Cultures in Neurobiological Research*. **3**, (Accademic Press, 1982).

144. Saddow, S. E. *et al.* Single-Crystal Silicon Carbide: A Biocompatible and Hemocompatible Semiconductor for Advanced Biomedical

Applications. *Mater. Sci. Forum* **679–680**, 824–830 (2011).

145. Frewin, C. L., Locke, C., Mariusso, L., Weeber, E. J. & Saddow, S. E. Silicon carbide neural implants: In vivo neural tissue reaction. *Int. IEEE/EMBS Conf. Neural Eng.* 661–664 (2013). doi:10.1109/NER.2013.6696021

146. Kim, R., Joo, S., Jung, H., Hong, N. & Nam, Y. Recent Trends in Microelectrode Array Technology for In Vitro Neural Interface Platform. *Biomed Eng Lett* **4**, 129–141 (2014).

147. Obien, M. E. J., Deligkaris, K., Bullmann, T., Bakkum, D. J. & Frey, U. Revealing neuronal function through microelectrode array recordings. *Front. Neurosci.* **8**, 1–30 (2015).

148. Aregueta-Robles, U. A., Woolley, A. J., Poole-Warren, L. A., Lovell, N. H. & Green, R. A. Organic electrode coatings for next-generation neural interfaces. *Front. Neuroeng.* **7**, 1–18 (2014).

149. Coletti, C. *et al.* Biocompatibility and wettability of crystalline SiC and Si surfaces. *Annu. Int. Conf. IEEE Eng. Med. Biol. - Proc.* 5849–5852 (2007).

150. Marchetti, L. *et al.* Site-specific labeling of neurotrophins and their receptors via short and versatile peptide tags. *PLoS One* **9**, 1–18 (2014).

151. Oliveros, A. *et al.* Cellular Interactions on Epitaxial Graphene on SiC (0001) Substrates. *Mater. Sci. Forum* **679–680**, 831–834 (2011).

152. Wang, S., Zhang, Y., Abidi, N. & Cabrales, L. Wettability and surface free energy of graphene films. *Langmuir* **25**, 11078–11081 (2009).

153. Lee, J. S. *et al.* Graphene substrate for inducing neurite outgrowth. *Biochem. Biophys. Res. Commun.* **460**, 267–273 (2015).

154. Keshavan, S., Naskar, S., Diaspro, A., Cancedda, L. & Dante, S. Developmental refinement of synaptic transmission on micropatterned single layer graphene. *Acta Biomater.* **65**, 363–375 (2018).

155. Taylor, A. M. *et al.* A microfluidic culture platform for CNS axonal injury, regeneration and transport. *Nat. Methods* **2**, 599–605 (2005).

156. Reina, G. *et al.* Promises, facts and challenges for graphene in biomedical applications. *Chem. Soc. Rev.* 4400–4416 (2017).

157. Levi-Montalcini, R. & Hamburger, V. Selective growth stimulating effects of mouse sarcoma on the sensory and sympathetic nervous system of the chick embryo. *J. Exp. Zool.* **116**, 321–361 (1951).

158. Levi-Montalcini, R. The nerve growth factor 35 years later. *Science* **237**, 1154–1162 (1987).

159. Riccio, A., Pierchala, B. A., Ciarallo, C. L. & Ginty, D. D. An NGF-TrkA-Mediated Retrograde Signal to Transcription Factor CREB in Sympathetic Neurons. *Science.* **277**, 1097–1100 (1997).

160. Reichardt, L. F. Neurotrophin-regulated signalling pathways. *Philos. Trans. R. Soc. B Biol. Sci.* **361**, 1545–1564 (2006).

161. Squire, L. *et al. Fundamental Neuroscience*. (Academic Press, 2012).

162. Roux, P. P. & Barker, P. A. Neurotrophin signaling through the p75 neurotrophin receptor. *Prog. Neurobiol.* **67**, 203–233 (2002).

163. Chowdary, P. D., Che, D. L. & Cui, B. Neurotrophin Signaling via Long-Distance Axonal Transport. *Annu. Rev. Phys. Chem.* **63**, 571–594 (2012).

164. Campenot, R. B. Local control of neurite sprouting in cultured

sympathetic neurons by nerve growth factor. *Dev. Brain Res.* **37**, 293–301 (1987).

165. Campenot, R. B. & MacInnis, B. L. Retrograde Transport of Neurotrophins: Fact and Function. *J. Neurobiol.* **58**, 217–229 (2004).

166. Hendry, I. A., Sto¨ckel, K., Thoenen, H. & Iversen, L. L. The retrograde axonal transport of nerve growth factor. *Brain Res.* **68**, 103–121 (1974).

167. Cui, B. *et al.* One at a time, live tracking of NGF axonal transport using quantum dots. *Proc. Natl. Acad. Sci.* **104**, 13666–13671 (2007).

168. De Nadai, T. *et al.* Precursor and mature NGF live tracking: One versus many at a time in the axons. *Sci. Rep.* **6**, 1–12 (2016).

169. Di Matteo, P., Calvello, M., Luin, S., Marchetti, L. & Cattaneo, A. An Optimized Procedure for the Site-Directed Labeling of NGF and proNGF for Imaging Purposes. *Front. Mol. Biosci.* **4**, 1–9 (2017).

170. Yin, J. *et al.* Genetically encoded short peptide tag for versatile protein labeling by Sfp phosphopantetheinyl transferase. *Proc. Natl. Acad. Sci.* **102**, 15815–15820 (2005).

171. Ferrari, A. C. *et al.* Raman spectrum of graphene and graphene layers. *Phys. Rev. Lett.* **97**, 1–4 (2006).

172. Cançado, L. G. *et al.* Quantifying defects in graphene via Raman spectroscopy at different excitation energies. *Nano Lett.* **11**, 3190–3196 (2011).

173. Parthasarathy, R. Rapid, accurate particle tracking by calculation of radial symmetry centers. *Nat. Methods* **9**, 724–726 (2012).

174. Siano, G. *et al.* Tau Modulates VGluT1 Expression. *J. Mol. Biol.* **431**,

873–884 (2019).

175. Rust, M. J., Bates, M. & Zhuang, X. Sub-diffraction-limit imaging by stochastic optical reconstruction microscopy (STORM). *Nat. Methods* **3**, 793–795 (2006).

176. Xu, K., Zhong, G. & Zhuang, X. Actin, Spectrin, and Associated Proteins Form a Periodic Cytoskeletal Structure in Axons. *Science* **339**, 452–456 (2013).

177. He, J. *et al.* Prevalent presence of periodic actin–spectrin-based membrane skeleton in a broad range of neuronal cell types and animal species. *Proc. Natl. Acad. Sci.* **113**, 6029–6034 (2016).

178. Zhong, G. *et al.* Developmental mechanism of the periodic membrane skeleton in axons. *Elife* **3**, 1–21 (2014).

179. Han, B., Zhou, R., Xia, C. & Zhuang, X. Structural organization of the actin-spectrin–based membrane skeleton in dendrites and soma of neurons. *Proc. Natl. Acad. Sci.* **114**, E6678–E6685 (2017).

180. Linetti, A. *et al.* Cholesterol reduction impairs exocytosis of synaptic vesicles. *J. Cell Sci.* **123**, 595–605 (2010).

181. Cappello, V. *et al.* Contrast solution. (2019).

182. Barde, Y. A. Trophic factors and neuronal survival. *Neuron* **2**, 1525–1534 (1989).

183. Chowdary, P. D., Che, D. L., Zhang, K. & Cui, B. Retrograde NGF axonal transport - Motor coordination in the unidirectional motility regime. *Biophys. J.* **108**, 2691–2703 (2015).

184. Ye, H., Kuruvilla, R., Zweifel, L. S. & Ginty, D. D. Evidence in support

of signaling endosome-based retrograde survival of sympathetic neurons. *Neuron* **39**, 57–68 (2003).

185. Campenot, R. B. NGF and the local control of nerve terminal growth. *J. Neurobiol.* **25**, 599–611 (1994).

186. Atwal, J. K., Massie, B., Miller, F. D. & Kaplan, D. R. The TrkB-Shc site signals neuronal survival and local axon growth via MEK and PI3-Kinase. *Neuron* **27**, 265–277 (2000).

187. Sung, K. *et al.* Swedish Nerve Growth Factor Mutation (NGF R100W) Defines a Role for TrkA and p75 NTR in Nociception . *J. Neurosci.* **38**, 3394–3413 (2018).

188. Wang, T. *et al.* Flux of signalling endosomes undergoing axonal retrograde transport is encoded by presynaptic activity and TrkB. *Nat. Commun.* **7**, (2016).

189. Williams, C. D., Dix, J., Troisi, A. & Carbone, P. Effective Polarization in Pairwise Potentials at the Graphene-Electrolyte Interface. *J. Phys. Chem. Lett.* **8**, 703–708 (2017).

190. Pham, T. A. *et al.* Salt Solutions in Carbon Nanotubes: The Role of Cation-π Interactions. *J. Phys. Chem. C* **120**, 7332–7338 (2016).

191. Stein, V. & Nicoll, R. A. GABA Generates Excitement. *Neuron* **37**, 375–378 (2003).

192. Vaillant, A. R. *et al.* 3-Kinase – Akt Pathway to Synergistically Regulate Neuronal Survival. *Cell* **146**, 955–966 (1999).

193. Nguyen, P. & Berry, V. Graphene interfaced with biological cells: Opportunities and challenges. *J. Phys. Chem. Lett.* **3**, 1024–1029 (2012).

194. Ferrari, A. C. & Basko, D. M. Raman spectroscopy as a versatile tool for studying the properties of graphene. *Nat. Nanotechnol.* **8**, 235–246 (2013).

195. Caponi, S. *et al.* Raman micro-spectroscopy: A powerful tool for the monitoring of dynamic supramolecular changes in living cells. *Biophys. Chem.* **182**, 58–63 (2013).

196. Kevenaar, J. T. & Hoogenraad, C. C. The axonal cytoskeleton: from organization to function. *Front. Mol. Neurosci.* **8**, 1–12 (2015).

197. Wang, T. *et al.* Radial contractility of Actomyosin-II rings facilitates cargo trafficking and maintains axonal structural stability following cargo-induced transient axonal expansion. *bioRxiv* (2019).

198. Fournier, A. J. *et al.* Changes in neurofilament and microtubule distribution following focal axon compression. *PLoS One* **10**, 1–21 (2015).

199. Tedeschi, A. & He, Z. Axon regeneration: Electrical silencing is a condition for regrowth. *Curr. Biol.* **20**, R713–R714 (2010).

200. Wang, Q. H., Kalantar-Zadeh, K., Kis, A., Coleman, J. N. & Strano, M. S. Electronics and optoelectronics of two-dimensional transition metal dichalcogenides. *Nat. Nanotechnol.* **7**, 699–712 (2012).

201. Kalantar-zadeh, K. *et al.* Two-Dimensional Transition Metal Dichalcogenides in Biosystems. *Adv. Funct. Mater.* **25**, 5086–5099 (2015).

202. Agarwal, V. & Chatterjee, K. Recent advances in the field of transition metal dichalcogenides for biomedical applications. *Nanoscale* **10**, 16365–16397 (2018).

203. Teo, W. Z., Chng, E. L. K., Sofer, Z. & Pumera, M. Cytotoxicity of exfoliated transition-metal dichalcogenides (MoS 2, WS2, and WSe2) is lower than that of graphene and its analogues. *Chem. - A Eur. J.* **20**, 9627–9632 (2014).

204. Palumbo, A., Tourlomousis, F., Chang, R. & Yang, E. H. Transition metal dichalcogenides as cell culture platforms. *Adv. Mater. - TechConnect Briefs 2017* **1**, 2–5 (2017).

205. Büch, H. *et al.* Superlubricity of epitaxial monolayer WS2 on graphene. *Nano Res.* **11**, 5946–5956 (2018).

206. Zhang, Y. *et al.* Controlled growth of high-quality monolayer WS2 layers on sapphire and imaging its grain boundary. *ACS Nano* **7**, 8963–8971 (2013).

207. Kurlov, V. N. Sapphire: Properties, Growth, and Applications. in *Encyclopedia of Materials: Science and Technology* **48**, 8259–8264 (Elsevier, 2001).

208. Shikunova, A. & Kurlov, V. N. Sapphire shaped crystals for medicine. *J. Phys. Conf. Ser.* **672**, 1–5 (2016).

209. Khan, S. P., Auner, G. G., Palyvoda, O. & Newaz, G. M. Biocompatibility assessment of next generation materials for brain implantable microelectrodes. *Mater. Lett.* **65**, 876–879 (2011).

210. Sharova, A. S. *et al.* Sapphire implant based neuro-complex for deep-lying brain tumors phototheranostics. *J. Phys. Conf. Ser.* **945**, 012009 (2018).

211. Encinas, M. *et al.* Sequential Treatment of SH-SY5Y Cells with Retinoic Acid and Brain-Derived Neurotrophic Factor Gives Rise to

Fully Differentiated, Neurotrophic Factor-Dependent, Human Neuron-Like Cells. *J. Neurochem.* **75**, 991–1003 (2002).

212. Rossi, A. 2D vertical heterostructures: growth, properties and applications.

213. Mishra, N. *et al.* Going beyond copper: wafer-scale synthesis of graphene on sapphire. **1904906**, 1–8 (2019).

214. Paoletti, F. *et al.* Intrinsic structural disorder of mouse proNGF. *Proteins Struct. Funct. Bioinforma.* **75**, 990–1009 (2009).

215. Rattenholl, A. *et al.* The pro-sequence facilitates folding of human nerve growth factor from Escherichia coli inclusion bodies. *Eur. J. Biochem.* **268**, 3296–3303 (2001).

216. Dahms, S. O. *et al.* X-ray structures of human furin in complex with competitive inhibitors. *ACS Chem. Biol.* **9**, 1113–1118 (2014).

217. Aricescu, A. R., Lu, W. & Jones, E. Y. A time- and cost-efficient system for high-level protein production in mammalian cells. *Acta Crystallogr. Sect. D Biol. Crystallogr.* **62**, 1243–1250 (2006).

218. Berkdemir, A. *et al.* Identification of individual and few layers of WS 2 using Raman Spectroscopy. *Sci. Rep.* **3**, 1–8 (2013).

219. Park, J. *et al.* Layer-modulated synthesis of uniform tungsten disulfide nanosheet using gas-phase precursors. *Nanoscale* **7**, 1308–1313 (2015).

220. Khan, S. P., Auner, G. G. & Newaz, G. M. Influence of nanoscale surface roughness on neural cell attachment on silicon. *Nanomedicine Nanotechnology, Biol. Med.* **1**, 125–129 (2005).

221. Cyster, L. A., Parker, K. G., Parker, T. L. & Grant, D. M. The effect of

surface chemistry and nanotopography of titanium nitride (TiN) films on primary hippocampal neurones. *Biomaterials* **25**, 97–107 (2004).

222. Brunetti, V. *et al.* Neurons sense nanoscale roughness with nanometer sensitivity. *Proc. Natl. Acad. Sci. U. S. A.* **107**, 6264–6269 (2010).

List of publications

2015

Bianco F., Perenzoni D., Convertino D., De Bonis S.L., Spirito D., Perenzoni M., Coletti C., Vitiello M.S., and Tredicucci A., **Terahertz detection by epitaxial-graphene field-effect-transistors on silicon carbide**, APL 107, 131104 (2015).

Bianco F., Miseikis V., Convertino D., Xu J-H., Castellano F., Beere H.E., Ritchie D.A., Vitiello M.S., Tredicucci A., Coletti C., **THz saturable absorption in turbostratic multilayer graphene on silicon carbide**, Optics Express 23 (9), 11632-11640 (2015).

Candini A., Richter N., Convertino D., Coletti C.,Balestro F., Wernsdorfer W., Kläui M. and Affronte M., **Electroburning of few-layer graphene flakes, epitaxial graphene, and turbostratic graphene discs in air and under vacuum**, Beilstein J. Nanotechnol. 6, 711–719 (2015).

Miseikis V., Convertino D., Mishra N., Gemmi M., Mashoff T., Heun S., Haghighian N., Bisio F., Canepa M., Piazza V., Coletti C., **Rapid CVD growth of millimetre-sized single crystal graphene using a cold-wall reactor**, 2D Mater. 2, 014006 (2015).

Mashoff T., Convertino D., Miseikis V., Coletti C., Piazza V., Beltram F. and Heun S., **Increasing the active surface of titanium islands on graphene by nitrogen sputtering**, APL 106, 083901 (2015).

2016

Kang J.H., Ronen Y., Cohen Y., Convertino D., Rossi A., Coletti C., Heun S., Sorba L., Kacman P., Shtrikman H., **MBE growth of self-assisted InAs nanowires on graphene**, Semicond. Sci. Tech. 31 (2016).

Rossi A., Büch H., Di Rienzo C., Miseikis V., Convertino D., Al-Temimy A., Voliani V., Gemmi M., Piazza V. and Coletti C., **Scalable synthesis of WS2 on graphene and h-BN: an all-2D platform for light-matter transduction**, 2D Mater. 3 (2016).

Meng F., Thomson M.D., Bianco F., Rossi A., Convertino D., Tredicucci A., Coletti C. and Roskos H.G., **Saturable absorption of femtosecond optical pulses in multilayer turbostratic graphene**, Opt. Express. 24(14), 15261-15273 (2016).

Takahashi K., Shigehito I., Kengo O., Mashoff T., Convertino D., Miseikis V., Coletti C., Tozzini V., Heun,S., **Revealing the multi-bonding state between hydrogen and graphene-supported Ti clusters**, J. Phys. Chem C 120(24), 12974–12979 (2016).

Convertino D., Rossi A., Miseikis V., Piazza V., Coletti C., **Thermal decomposition and chemical vapor deposition: a comparative study of multi-layer growth of graphene on SiC(000-1)**, MRS Advances, 1(55), 3667–3672 (2016).

Chen J.W., Huang H.C., Convertino D., Coletti C., Chang L.Y., Shiu H.W., Cheng C.M., Lin M.F., Heun S., Chien F.S.S., Chen Y.C., Chen C.H., Wu C.L., **Efficient n-type doping in epitaxial graphene through strong lateral orbital hybridization of Ti adsorbate**, Carbon 109, 300-305 (2016).

Mishra N., Miseikis V., Convertino D., Gemmi M., Piazza V., Camilla Coletti C., **Rapid and catalyst-free van der Waals epitaxy of graphene on hexagonal boron nitride**, Carbon 96, 497–502 (2016).

2017

Zanotto S., Bianco F., Miseikis V., Convertino D., Coletti C., and Tredicucci A., **Coherent perfect absorption and transparency in lossy and loss/gain metasurface-embedding structures**, 19th International Conference on Transparent Optical Networks (ICTON) (2017).

Convertino D., Luin S., Marchetti L. and Coletti C., **Peripheral neuron survival and outgrowth on graphene**, Front Neurosci. 12(1), 2018.

Candini A., Martini L., Chen Z., Mishra N., Convertino D., Coletti C., Narita A., Feng X., Mullen K. and Affronte M., **High photoresponsivity in graphene nanoribbon field-effect transistor devices contacted with graphene electrodes**, J. Phys. Chem C 121(19), 10620–10625 (2017).

2018

Büch, H., Rossi, A., Forti, S. Convertino D., Tozzini V., Coletti C., **Superlubricity of epitaxial monolayer WS_2 on graphene**, Nano Res., 1-11 (2018).

Haghighian N., Convertino D., Miseikis V., Bisio F., Morgante A., Coletti C., Canepa M., Cavalleri O., **Rippling of graphitic surfaces: a comparison between few-layer graphene and HOPG**, Phys. Chem. Chem. Phys.,20, 13322-13330 (2018).

Forthcoming

Convertino D., Fabbri F., Mishra N., Mainardi M., Cappello V., Signore G., Testa G., Capsoni S., Albertazzi L., Luin S., Marchetti L., Coletti C., **Graphene promotes axon elongation through local stall of Nerve Growth Factor signalling endosomes**.

Amodeo R., Convertino D., Bonsignore F., Ravelli C, Calvello M., Luin S., Mitola S., Cattaneo A., Signore G., and Marchetti L., **Comparative study of different membrane receptors and fluorophores in the performance of YBBR-related chemical tag labelling reactions**.

Convertino D., Mishra N., Marchetti L., Calvello M., Viegi A., Fabbri F., C. Coletti C., **Cell viability on centimeter-scale WS_2 and graphene on a transparent substrate**.